AEDC-TR-90-18

C#3

Space Chambers Contamination Diagnostics and Analysis

W. D. Williams, R. J. Bryson, W. T. Bertrand,
and
J. H. Jones
Calspan Corporation/AEDC Operations

December 1990

Final Report for Period October 1, 1987 — August 31, 1990

ARNOLD ENGINEERING DEVELOPMENT CENTER
ARNOLD AIR FORCE BASE, TENNESSEE
AIR FORCE SYSTEMS COMMAND
UNITED STATES AIR FORCE

NOTICES

When U. S. Government drawings, specifications, or other data are used for any purpose other than a definitely related Government procurement operation, the Government thereby incurs no responsibility nor any obligation whatsoever, and the fact that the Government may have formulated, furnished, or in any way supplied the said drawings, specifications, or other data, is not to be regarded by implication or otherwise, or in any manner licensing the holder or any other person or corporation, or conveying any rights or permission to manufacture, use, or sell any patented invention that may in any way be related thereto.

Qualified users may obtain copies of this report from the Defense Technical Information Center.

References to named commercial products in this report are not to be considered in any sense as an endorsement of the product by the United States Air Force or the Government.

This report has been reviewed by the Office of Public Affairs (PA) and is releasable to the National Technical Information Service (NTIS). At NTIS, it will be available to the general public, including foreign nations.

APPROVAL STATEMENT

This report has been reviewed and approved.

SETH SHEPHERD, Capt, USAF
Flight Dynamics Division
Directorate of Technology
Deputy for Operations

Approved for publication:

FOR THE COMMANDER

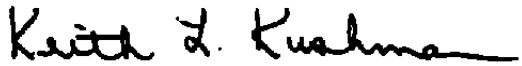

KEITH L. KUSHMAN
Technical Director
Directorate of Technology
Deputy for Operations

REPORT DOCUMENTATION PAGE

Form Approved
OMB No. 0704-0188

1. AGENCY USE ONLY (Leave blank)	2. REPORT DATE	3 REPORT TYPE AND DATES COVERED
	December 1990	Final Report for 10/1/87 - 7/31/90

4 TITLE AND SUBTITLE

Space Chambers Contamination Diagnostics and Analysis

5 FUNDING NUMBERS

PE - 65807F

6 AUTHOR(S)

Williams, W. D., Bryson, R. J., Bertrand, W. T., and Jones, J. H., Calspan Corporation/AEDC Operations

7 PERFORMING ORGANIZATION NAME(S) AND ADDRESS(ES)

Arnold Engineering Development Center/DOT
Air Force Systems Command
Arnold Air Force Base, Tennessee 37389-5000

8. PERFORMING ORGANIZATION REPORT NUMBER

AEDC-TR-90-18

9 SPONSORING/MONITORING AGENCY NAMES(S) AND ADDRESS(ES)

Arnold Engineering Development Center/DO
Air Force Systems Command
Arnold Air Force Base, Tennessee 37389-5000

10 SPONSORING/MONITORING AGENCY REPORT NUMBER

11 SUPPLEMENTARY NOTES

Available in Defense Technical Information Center (DTIC).

12a DISTRIBUTION/AVAILABILITY STATEMENT

Approved for public release; distribution is unlimited.

12b DISTRIBUTION CODE

13. ABSTRACT (Maximum 200 words)

In order for the AEDC to meet its requirement to be the Center of Expertise (COE) for space environmental simulation, a technology effort was structured to provide the required enabling technologies. The proper simulation of the space environment in a ground test chamber requires a complete characterization and control of facility, chamber, and test article generated contaminants. To meet these testing requirements, the objectives of this project included the development of (1) laboratory diagnostics support, (2) online diagnostic instrumentation, and (3) computational analysis capability. A laboratory capability was developed to screen materials for contamination potential and to identify unknown contaminants. New diagnostic techniques for more sensitive contaminant mass measurements and particulate cleanliness level measurements were identified. Contamination analysis development included evaluation of codes to simulate molecular flow in test chambers, establishment of a material property database, and installation of library data and algorithms for identification of unknown contaminants by mass spectra searches.

14 SUBJECT TERMS		15. NUMBER OF PAGES
space chamber test contamination	**diagnostics analysis capability**	**154**
		16 PRICE CODE

17 SECURITY CLASSIFICATION OF REPORT	18 SECURITY CLASSIFICATION OF THIS PAGE	19 SECURITY CLASSIFICATION OF ABSTRACT	20. LIMITATION OF ABSTRACT
UNCLASSIFIED	**UNCLASSIFIED**	**UNCLASSIFIED**	**SAME AS REPORT**

COMPUTER GENERATED

Standard Form 298 (Rev. 2-89)
Prescribed by ANSI Std Z39-18
298-102

PREFACE

The work reported herein was performed by the Arnold Engineering Development Center (AEDC), Air Force Systems Command (AFSC). The results were obtained by Calspan Corporation/AEDC Operations, operating contractor for the aerospace flight dynamics testing facilities at the AEDC, AFSC, Arnold Air Force Base, Tennessee, under Project Number DC05VK. The Air Force Project Manager was Capt. S. D. Shepherd, AEDC/DOT. The data analysis was completed on July 31, 1990, and the manuscript was submitted for publication on November 8, 1990.

The authors acknowledge the efforts of L. L. Price, B. W. Hobbs, B. J. McClure, and W. E. Johnson in the laboratory measurement phase of the project.

CONTENTS

ILLUSTRATIONS

Figure Page

Figure Page

TABLES

Table Page

APPENDIX

1.0 INTRODUCTION

For the Arnold Engineering Development Center (AEDC) to successfully accomplish its mission as the Center of Expertise (COE) for space environmental simulation, a technology effort was structured to provide the required enabling technologies. This project has been formulated to concentrate on the major technical problems in the space environment simulation area, and it focused on contamination and cryovacuum materials.

The contamination effort is of major importance because the proper simulation of the space environment in a ground test chamber requires a complete characterization and control of facility-, chamber-, and test-article-generated contaminants. Future space-based systems will have cooled optical and detection systems that can be degraded or rendered inoperative by contaminant deposition. Contamination of thermal control surfaces and solar cell arrays can also result in a satellite thermal imbalance and a loss of solar cell efficiency. The design on-orbit lifetimes of future systems will impose extremely stringent contamination budgets. To test such systems or components in AEDC test chambers and maintain a reasonable simulation of the test environment will require control and monitoring of contamination that is three orders of magnitude better than present AEDC capability. Routine facility and chamber contamination monitoring devices should be developed to provide online determination of when, where, what, how much, and why contamination occurs. All optical surfaces within the test chamber should be carefully monitored for contamination levels before, during, and after testing. Computational capability is required for prediction of contamination sources, transport mechanisms, and flux levels to sensitive surfaces or volumes. All materials introduced into the chambers should be controlled and/or screened for minimum outgassing, thermal diffusion, and optical effects.

To meet these testing requirements, the objectives of this project included the development of laboratory diagnostics support, online diagnostic instrumentation, and a computational analysis capability and materials database.

2.0 LABORATORY DIAGNOSTICS

Laboratory diagnostics are required to provide a complete characterization of materials to be used in the space chambers, and to identify unknown contaminants detected during testing. Design, fabrication, and operation of a new research chamber and procurement of diagnostic instrumentation was completed to meet these requirements.

2.1 DESCRIPTION OF OUTGASSING CHAMBER

2.1.1 Mechanical Configuration

The present outgassing chamber (OGC) is shown schematically in a side view in Fig. 1 and in a plan view in Fig. 2. The basic test chamber is 17.5-in. (44.45-cm) ID with an inside height of 6.5 in. (16.51 cm). Eight 2-in. (5.08-cm)-diam access ports are equally spaced around the cylinder circumference. The OGC is evacuated using a 400-ℓ/sec turbomolecular pump. The OGC and pump are connected through an isolation valve and an LN_2-cooled trap just above the pump. An LN_2-cooled liner has been placed in front of the inside lateral wall area of the OGC to help pump any condensable species, as well as to provide a cold background for quartz crystal microbalances (QCM). Without any intentionally introduced outgassing, the chamber pressure can be maintained at approximately 1×10^{-6} and 1×10^{-7} torr without and with LN_2 cooling, respectively. The pressure in the OGC is monitored with a Bayard-Alpert-type ion gage.

2.1.2 Effusion Cell

An effusion cell (Fig. 3) is used to introduce contaminating substances into the OGC. The effusion cell maintains a candidate material at a specified temperature and has an orifice that allows the emitted vapor to impinge on a test surface. The effusion cell is fitted with a solenoid-operated shutter that blocks the exit orifice and stops the flow of contaminating species when it is energized. This shutter permits periodic interruption of the contaminant flow without having to shut off the effusion cell heat. It also provides for a smooth startup of data acquisition by permitting the effusion cell to come to operating temperature before exposing surfaces or diagnostic instrumentation to the contaminant flux. The shutter assembly can be removed from the effusion cell if desired. Heat to the effusion cell is provided by two band-type resistance heaters, and the set temperature is maintained by a temperature controller using a type-T thermocouple as the sensing element. The effusion cell orifice plate is replaceable and allows different orifice geometries to be used. The presently installed plate has a 1.5-in.-diam orifice.

2.2 DIAGNOSTICS

2.2.1 Quartz Crystal Microbalance

The primary instrument for measurement of mass deposition and rate deposition is presently the quartz crystal microbalance (QCM). This device (Fig. 4) consists of a quartz crystal, an electronic oscillator, and data processing electronics. The *piezoelectric* effect of the quartz crystal is used to stabilize the resonance frequency of the oscillator. The term

piezoelectric refers to the generation of an electromotive force between the faces of a crystal when pressure is applied. Conversely, application of voltage to the crystal faces produces a corresponding mechanical distortion. An alternating voltage applied to the crystal produces mechanical vibrations of the quartz, and the vibrations are particularly strong at the resonant frequency. From an electronic viewpoint, the crystal assembly appears as a sharply resonant circuit capable of stabilizing the frequency of oscillations. This resonance frequency, depending on the angle of the crystal cut, is a function of the mass deposited on the crystal surface and the crystal temperature. To minimize the influence of temperature, a doublet crystal is cut and arranged (See Fig. 5) so that two independent crystal oscillators are obtained. One of the elements is exposed to the mass flux to be measured, whereas the other (the reference oscillator) is shielded from any flux. Both crystals are constrained to the same temperature environment; therefore, the beat frequency is dependent (in principle) only on mass deposition.

The OGC is equipped with two QCMs, both Mark 9 models manufactured by QCM Research, operating in thickness shear mode. One QCM is designed to operate near room temperature (298 K), and the other is designed to operate near 77 K. The room-temperature QCM has its crystals cut at 35 deg 18 min (relative to the mother crystal Z axis). The low-temperature QCM has its crystals cut at 39 deg 40 min. As shown by Wallace (Ref. 1), these cuts provide minimum frequency dependence near the operating temperature. However, both QCMs can be operated over the full temperature range. The crystal operating frequency is 10 MHz, and the beat frequency is in the kHz range. These QCMs are arranged so that they are adjacent to each other and facing in the same direction (See Fig. 3).

For crystals operating in thickness shear mode, the dependence of frequency shift (Δf) on mass addition per unit area ($\Delta m/a$) is given (Ref. 1) as

$$\frac{\Delta f}{\Delta m/a} = -2.26 \times 10^8 \text{ Hz/gm/cm}^2 \tag{1}$$

Although an actual decrease in frequency with mass addition is shown in Eq. (1), the QCM electronics are adjusted to produce an increasing beat frequency with increasing mass deposition.

In terms of deposit thickness h, and mass density ϱ, the frequency change can be expressed as

$$\Delta f = 2.26 \times 10^8 \, \varrho h, \text{ Hz} \tag{2}$$

where h is thickness in cm, and ϱ is density in gm/cm^3. If the material covering the crystal is known well enough to assume a density, the thickness of the deposit can be determined.

2.2.2 Mass Spectrometer

The primary OGC instrument for species identification is a DYCOR® Model M200 quadrupole mass spectrometer (QMS). The QMS is housed in a separate plumbing system that can be isolated from the chamber by a high-vacuum valve (See Fig. 1). Copper gaskets are used for all the QMS system joints, which permits bakeout of the system to speed system attainment of maximum cleanliness. If so desired, the copper gasket on the QMS side of the isolation valve can be replaced with a copper disc with a pinhole to restrict the amount of outgassing material that can enter the QMS. The QMS housing has an independent 40-ℓ/sec turbomolecular pump that permits continued operation of the QMS when it is isolated from the chamber. The QMS also has its own Bayard-Alpert ion gage to monitor pressure.

The mass range of the QMS is 1 to 200 amu, and all instrument functions may be controlled through a microcomputer via RS-232 interface or from the front panel. Data can be displayed in bar graph, analog, or tabular format on a high-resolution 12-in. screen, and detection is accomplished by electron multiplier or Faraday cup. The maximum sensitivity of the QMS is approximately 10^{-14} torr. The major advantage of the present system is its ability to subtract from the OGC mass spectra the signal associated with the QMS itself. The major disadvantages are the limited mass number range that prevents detection/identification of high mass number hydrocarbons and isomeric species, and the slow scan speed (2.5 min is required to scan 200 amu to distinguish peaks with a signal-to-noise ratio of two). This slow scan speed makes monitoring of transient events difficult.

2.2.3 Gas Chromatography/Mass Spectrometry

Gas chromatography (GC) is an essential part of the Lockheed standardized test method (Ref. 2) for characterizing outgassing materials. GC is used in an *ex-situ* (relative to the OGC) role to obtain information on the number, identity, and relative concentration of species outgassing from a given material. A technique is used called gas chromatography/mass spectrometry (GC/MS).This technique uses a mass spectrometer as a detector, and a capillary column along with a helium carrier gas and split injection is used in the GC. The GC identifies outgassing species by correlation with their elution time through the capillary column. When a species is detected, the mass spectrometer obtains mass fragmentation pattern data for that particular species. The fragmentation pattern data can then be correlated with the mass spectrometer data obtained during sample isothermal outgassing and thermogravimetric analysis in the OGC. GC/MS is also extremely valuable for analyzing wipe or witness plate contaminant samples.

A Tracor® Model 800 GC/MS is available for analysis of externally injected solvent-borne samples. This instrument is also equipped with a pyrolizer attachment to allow solid samples

to be injected and heated for analysis. Included as a convenience with this instrument is a library of fragmentation patterns of many compounds that can be searched for any matches (or near matches) of the sample pattern. This feature can help speed up the sample identification process (See Section 4.2).

2.2.4 Microscope

The ability to characterize an optical detection instrument's response to particulate contamination requires that the amount of particulate matter present on the detection surface be known. The best standard of comparison to use for this characterization is to actually count the number of particles of a particular size on the surface. Accurate counting requires sufficient resolution to detect the smallest particle to be included in the count.

The system used to count particles is a 700X Bausch and Lomb® optical microscope equipped with a zoom lens feature and a color TV camera that permits display of its field of view on a color TV monitor. This system allows particles as small as 1 μm to be routinely counted.

2.2.5 Balance

Researchers must know the amount of mass in a particular material sample when they are attempting to establish the total mass loss (TML) characteristic of that material. TML for materials will be discussed further in Section 2.3.1.4.2. The scale available to measure sample mass is a Fisher Scientific Model XA-200DS with a resolution of 10 μg for samples of 30 gm or less and 100 μg for samples between 30 and 200 gm. On the low range, the change in a gram sample can be determined to within ± 0.001 percent.

2.2.6 Humidity Chamber

Measurement of the outgassing properties of a material uses time as the scale along which changes are recorded; so comparison of the properties of different materials requires that they must have the same starting point. The most variable starting properties of a sample are moisture content and temperature. Preconditioning of these two properties can only be accomplished in an environment where they can be independently controlled.

Pretest conditioning of samples is accomplished using a BLUE M Model VP-100AT-1 humidity chamber. This chamber can furnish environments with temperatures from ambient to 77°C and relative humidities from 20 to 98 percent.

2.3 MATERIALS SCREENING/SPECIES IDENTIFICATION

2.3.1 OGC Measurements

The properties of materials listed in Table 1 were measured in the OGC. Sample percent total mass loss, sample outgassing rate, and mass spectra of the outgassing products were measured.

2.3.1.1 Chamber Preparation

The OGC vacuum chamber, the mass spectrometer sampling system, and the sample heating effusion cell were all conditioned before a test to minimize the amount of background contamination present. All these components were evacuated to a pressure of about 10^{-5} torr for several hours before a test was to begin. The effusion cell was heated to about 130°C (5°C above the test temperature of 125°C) while under vacuum. The mass spectrometer system was also heated while it was evacuated to speed the clean-up process.

The mass spectrometer was used as an indication of the entire system's cleanliness level. The mass spectrometer was monitored periodically, and the pumping and heating were continued until it indicated that the system contaminant background levels would not interfere with sample measurements.

2.3.1.2 Sample Preparation

The sample material was contained in an open aluminum vessel or boat for these tests. The boat was a convenient way to confine the sample material and insert it into the effusion cell for heating. Any sample normally used as a film, such as Epoxy® adhesive, was applied to aluminum strips that were placed in the boat for the test. The boat and any strips that were used were first placed in a vacuum oven and baked at about 130°C for at least 4 hr. After the boat and strips were vacuum baked, they were weighed on the lab balance.

Sample material was in many forms. Solid samples were cut into pieces to expose as much surface area as possible. Soft samples were placed directly in the aluminum boat. As stated before, samples such as paint and adhesives were applied to aluminum strips before being placed in the boat. Any material that required curing was cured for 24 hr.

After a sample boat was prepared, it was placed in the humidity chamber and conditioned there at a relative humidity of 50 percent and a dry bulb temperature of 30°C for a minimum of 24 hr. When the humidity conditioning was completed, the sample was weighed on the lab balance. This was done just before the sample was placed in the effusion cell for testing.

2.3.1.3 Experimental Procedure

The evaluation of a sample material was begun after chamber preparations and sample preparations were completed. Pumping of the chamber was discontinued, and the chamber was returned to atmospheric pressure by admitting dry nitrogen gas. (Dry gas was used to minimize adsorption of water vapor by the chamber walls.) The chamber was opened, and the sample boat was placed in the effusion cell. The chamber was immediately closed and pumping resumed.

When the chamber pressure reached 10^{-4} torr, liquid nitrogen cooling of the cryoliner was started. Liquid nitrogen cooling of the QCM was started after the cryoliner temperature had stabilized at its lowest value. (The actual temperature was determined by the laboratory liquid nitrogen supply conditions and was usually 85 K.)

Power to the effusion cell heater was started after the temperature of the QCM stabilized. The power controller was set at 125°C, and it maintained this temperature after a warmup period of approximately 30 min. The effusion cell temperature was maintained at 125°C ±1°C for a test period of 24 hr.

Chamber pressure had to reach 1^{-5} torr before the mass spectrometer isolation valve could be opened. When this point was reached, the mass spectrometer was opened to the chamber, and samples of the chamber environment were pumped through its ionization source. Mass spectra were obtained at each stage of the operation of the chamber and at intervals throughout the heating of the sample material.

The QCM was kept cold to collect the condensable, incident mass flux as long as the mass rate was greater than 10^{-10} gm/cm^2-sec. When the condensation rate had slowed to below that level, the liquid nitrogen cooling was removed from the QCM, and it was allowed to warm up. As the QCM warmed, the condensed material re-evaporated at the temperatures associated with the vapor pressures of the various species.

At the end of the 24-hr evaluation period, power was removed from the effusion cell. The liquid nitrogen cooling of the cryoliner was discontinued, and dry nitrogen gas was flowed through the liner to help warm it to room temperature. The chamber was then returned to ambient pressure using dry nitrogen gas. The sample material was removed from the effusion cell and weighed on the laboratory balance.

2.3.1.4 Experiment Results

Determination of the various characteristics of the outgassing products described in the following sections was accomplished for each material tested. The material described in these sections was DeSoto® paint and serves as a typical example to illustrate the results.

2.3.1.4.1 QCM Results

A continuous record of the amount of total mass condensed on or evaporated from the cold QCM crystal was furnished by the changing output frequency of the QCM. Figure 6 shows a typical condensation phase obtained from the paint sample. The time scale starts with power-up of the effusion cell heater.

The total deposited mass does not always show rate of change clearly; therefore, the QCM also furnishes the rate at which mass is deposited. The rate at which the mass of Fig. 6 was deposited is shown in Fig. 7. Figures 6 and 7 show that most of the outgassing occurred within the first 200 min, and that after 400 min, very little material was accumulated.

The rate is again the most sensitive indicator of mass change when the QCM cooling is halted. At a constant chamber pressure, the QCM crystal temperature determines the point at which each species is evaporated from the surface, according to its vapor pressure. Figure 8 shows the mass release rate record of the same paint sample shown in the previous figures. The average pressure in the chamber during evaporation was about 1^{-6} torr; but as the release of materials occurred, the pressure increased until the release ended and the pump recovered. This fluctuation in pressure tends to widen the temperature window where the release occurs because a rise in pressure causes the temperature at which evaporation takes place to rise also. The species associated with the evaporation peaks shown in the figure have not been identified; however, the first peak at 172 K is most likely water vapor, even though the temperature appears to be about 10 K too great for the chamber pressure.

The mass deposited on the room-temperature QCM is shown in Fig. 9. The condensation trend was the same here as for the cold QCM, but the amount of mass was about an order-of-magnitude less. When the effusion cell power was turned off, the mass on the room-temperature QCM slowly evaporated until it eventually returned to its pretest condition.

2.3.1.4.2 Determination of Percent Total Mass Loss

The percent total mass loss (TML) of a material is a measure of how detrimental the outgassing from the material could be in a vacuum environment when the material is heated. One technique for determining TML is to weigh the sample before the 24-hr measurement

period is begun, then again after the measurement period is completed, and then calculate the percentage lost during the period. Evaluating a material at the particular conditions to which it would be subjected in a specific application would give better absolute values for TML for that application. However, the relative TML values for different materials can be compared by measurements at a common set of conditions as was done here. The TML for the paint sample used in this example test, determined by weighing, was 2.27 percent.

Another technique for determining TML has been developed by Lockheed (Ref. 2). This technique involves using the QCM mass accumulation rate along with a model that relates the amount of material collected on the QCM to the amount of material given off by the sample. The model includes the effect of the effusion cell orifice on the flow through it and accounts for the spatial distribution of flux at the location of the QCM. When all of the factors for the present test setup are evaluated, the equation

$$m_s = (362.03)\frac{1}{C_c} m_g \tag{3}$$

relates the mass loss rate by the sample, m_s, to the mass gain rate of the QCM, m_g, where C_c is the condensation coefficient. The TML is defined as the percentage loss of the material over a 24-hr period. The pretest sample mass was 1.29475 gm, and the average mass accumulation rate over the evaluation was 8.58×10^{-10} gm/sec; therefore,

$$TML = 2.07/C_c \tag{4}$$

If a condensation coefficient of 1 is assumed, then TML = 2.07 percent, which compares favorably with that obtained by weighing.

2.3.1.4.3 Mass Spectra of Outgassing Products

One way to help identify an unknown contaminant in a vacuum chamber is to obtain a mass spectrum of the chamber environment. This spectrum can then be compared to spectra on file for known materials with the hope that a match can be found.

Mass spectra of the outgassing products were obtained at various times during the 24-hr measurement period for each material so that they could be put on file. Mass spectra scans were repeated two or three times at each sampling time so that they could be averaged to try to improve the signal-to-noise ratio. Also, two or more scans of the chamber background contamination before sample insertion were made and averaged to establish a chamber-only spectrum. The difference of the sample spectrum and the background spectrum was then formed to obtain a spectrum of the sample alone. A typical mass spectrum formed in this

manner is shown in Fig. 10. This spectrum is now available as a comparison for future unknown spectra.

3.0 TEST CHAMBER DIAGNOSTICS

3.1 NEEDS FOR ONLINE DIAGNOSTICS

Contamination can shorten the operational lifetime and reduce the capability of spacecraft. Surveillance satellites such as the Space Surveillance and Tracking System (SSTS) will have large, cooled optical and detector systems that can become degraded or inoperative because of contaminant deposition. The SSTS serves as a good example of the stringent contamination requirements for future spacecraft. The design, on-orbit lifetime of SSTS is 10 yr. In Ref. 3, a worst-case, on-orbit analysis (assuming CO_2 as a contaminant) has shown that if a 10-percent performance degradation can be tolerated for the main sensor optical/detector system, then a maximum molecular contamination of only 3.3×10^{16} molecules/cm^2 (~ 58 monolayers or 2.4 μg/cm^2) can be allowed. Assuming that a 10-percent performance degradation could be tolerated during a fairly typical 8-week ground testing period, the tolerable contamination deposition rate would be 6.8×10^9 molecules/cm^2-sec, ~0.2 Å/hr, ~0.5 pgm/cm^2-sec. Therefore, to monitor the contamination environment of AEDC space simulation chambers, extremely sensitive devices are required. However, detection sensitivity is only part of the need for ground-based testing. If any steps are to be taken during a test to stop or limit contamination and if any analytical measures are to be taken to compensate for contamination, then identification of contaminating species must also be accomplished. At present, AEDC has three principal contamination diagnostic systems: the quartz crystal microbalance (QCM), the quadrupole mass spectrometer (QMS), and the attenuated total reflectance (ATR) plate. Unfortunately, these devices are severely limited in their ability to meet future sensitivity/specificity requirements.

3.2 LIMITATIONS OF QCM, QMS, AND ATR TECHNIQUES

At present, the primary AEDC instrument for detection of contamination is the QCM. Details of operating principles were discussed in Section 2.2.1. The short-term (measurement time $\leq$60 sec) sensitivity is greater than 7×10^{-11} gm/cm^2-sec, and the long-term (measurement time ~24 hr) sensitivity is greater than 5×10^{-13} gm/cm^2-sec. The short-term sensitivity is not sufficient for online contamination detection in AEDC space chambers based on the contamination budget predicted for future space surveillance systems. In addition, the QCM has only a limited capability to identify contaminant species based on operation of a QCM array with each at a different temperature and species differentation based on vapor pressure versus temperature differences. This technique is limited to only low mass number species and environments consisting of just a few species. The QCM may be operated

in thermogravimetric mode in conjunction with a mass spectrometer to provide species identification, but this can be done only after a test is concluded. In an effort to give a QCM additional capability for species identification, AEDC developed the polished QCM (PQCM). The polished crystal surface permits monitoring of diode laser interference patterns. Measurement of the pattern intensity using two lasers and two incidence angles permits determination of the refractive index of a surface contaminant, which permits calculation of the contaminant film thickness. Because the QCM normally measures mass per unit area, the film density can be calculated. If the density value lies close to the value of a particular molecular species, then species identification is possibly obtained. However, this requires the assumption that the contaminant is comprised of a single molecular species, and this is not a reliable assumption.

The second most used instrument for detection and identification of contamination at AEDC is the quadrupole mass spectrometer (QMS) in a direct sampling mode. The QMS can indeed display mass spectral patterns that can be used for species identification, but for high mass number hydrocarbons and isomeric species, the spectra are extremely difficult to interpret. Furthermore, the hot filament of the QMS ionizer system produces infrared radiation that can interfere with sensor testing, which is the type of testing most in need of contamination measurements. Of course, the QMS can be strategically positioned behind cryoliners, but this limits its role to that of a residual gas analyzer. The QMS must sample within the chamber region internal to cryoliners to be effective in identifying species, and multiple QMS systems must be used to help identify sources. The latter is an expensive proposition.

Another traditionally used contamination diagnostic at AEDC is an ATR plate. A thin plate of germanium or KRS-5 is normally used, and infrared radiation (IR) is focused onto the plate edges typically beveled at 45 deg. The IR is transmitted through the plate by undergoing multiple reflections before exiting at the opposite beveled edge. If a contaminant film is on the plate, incident IR energy is absorbed at each reflection point. The absorption occurs at wavelengths corresponding to molecular vibrational bands; therefore, measurement of the absorption spectra provides an identification of contaminating species. Unfortunately, there are a number of shortcomings with the ATR plate technique, and they can be classified as interpretation or operational problems. Interpretation problems center on the complexity of IR absorption spectra for a mixture of species and on the dependence of penetration depth (d_p) on the IR wavelength (λ). Typically, $d_p \approx 0.2\lambda$; therefore, if the contaminant deposit thickness (h) equals or exceeds d_p for lowest λ, the IR absorption spectral signature will be dependent on deposit thickness. Operational problems center on the present inability to obtain a spectral scan when the sample plate is cold. Waiting until a test is over, removing the ATR sample plate, allowing it to warm up, and then analyzing the remaining deposit provides meaningless, untimely data. The development of an ATR apparatus was undertaken to circumvent this operational problem. A cooled ATR plate and internal space chamber optics

were arranged so that radiation from a Fourier transform infrared (FTIR) spectrometer could enter the chamber, be transmitted within the ATR plate, and exit the chamber to a detector. Although this was an excellent plan, IR leakage prevented the device from being useful in sensor testing. As a result of these limitations, a number of new diagnostic techniques have been investigated. Species identification techniques studied included surface-enhanced Raman scattering, online fiber-optic ATR technique, and cryosample transfer to a laboratory chamber for analysis. A surface acoustic wave microsensor was studied for improved mass measurement sensitivity. Laser scattering was studied for particulate measurements.

3.3 SAMPLE TRANSFER MECHANISM (STM)

3.3.1 AEDC Concept

The requirements addressed by the AEDC STM were (1) a high-vacuum, leak-free system; (2) liquid nitrogen cooling of the sample plate at all times; (3) portability in the sense that a technician with the aid of a small cart could remove the sample from a test chamber and bring it to the research laboratory and insert the sample into the OGC; (4) sample plate temperature and STM vacuum level must be monitored at all times; and (5) the STM must provide both linear and rotary motion of the sample plate.

The mechanism is shown in Fig. 11. The aluminum sample collection plate is screwed into a copper heat sink that is cooled by tubes containing liquid nitrogen (LN_2). The heat sink is brazed into a tube that serves as the manual actuator, and also can be evacuated to insulate the tubes carrying the LN_2 coolant. A type-T thermocouple is welded into the copper heat sink to monitor its temperature and exits the actuator tube at the rear through a compressed plastic fitting.

The sample-gathering actuator enters the vacuum chamber through a housing that is equipped on one end with an isolation vacuum valve and on the other with a compressed O-ring vacuum seal. This allows the sample plate to be pulled behind the isolation valve for transport while still cold and under vacuum. The LN_2 coolant is furnished from a portable dewar so that cooling of the sample plate can be maintained during transport. The pressure in the transfer system is monitored while it is in transit by a Pirani gage. A pressure rise alerts the operator to any compromise of the sample by leakage.

Operation of the STM is begun by connecting it to the OGC to evacuate it and to remove contamination products. The decontamination process is monitored with the QMS, which allows a permanent chronological record of the mass scans of the contents of the chamber to be maintained. The monitoring mass spectrometer output furnishes a record of the transfer system's background contamination when the evacuation is complete.

After evacuation is terminated, the sample plate is pulled behind the isolation gate valve and the valve is closed. The transfer system is then detached from the OGC, the proper adaptor section for the chamber of interest is connected, and the system is mounted on the chamber to be examined. The chamber to which the transfer system is attached is then evacuated or, in the case of attachment at a second isolation valve, the connecting space is evacuated, the chamber isolation valve is opened, and the sample plate is pushed into the chamber. Liquid nitrogen is then flowed through the sample plate cooling lines until a proper sample is collected. After the sample has been collected, the valving and attachment procedures are reversed to return the transfer system to the OGC. The sample plate is then warmed by flowing dry gas through the cooling lines to release the sample into the OGC for analysis.

Operation of the STM was modified for this demonstration experiment. Instead of moving the entire assembly from one chamber to another to obtain a sample, the effusion cell in the OGC was used to contaminate the sample plate. After contamination of the plate was accomplished, it was moved behind the isolation valve, and the chamber was warmed up and repressurized to atmospheric pressure so the contaminant material could be removed from the chamber. The chamber was then re-evacuated, cooled, and the actuator was moved into the chamber for analysis. This operation subjected the STM to the same conditions that would be experienced in an actual transfer without having to move all the equipment.

3.3.2 Experimental Results

3.3.2.1 Sample Plate Contamination

The STM sample plate was placed in front of the effusion cell to collect contamination from RTV560 heated to 125°C. The room-temperature and cold QCMs were also exposed to the same contaminant flux so an estimate of the amount of material collected on the sample plate could be made. A typical contamination versus time curve is shown in Fig. 12 for both QCMs. The ordinate for both these curves is the amount of contaminant in micrograms collected on the QCM's crystal surface of 0.316 cm^2. The abscissa is the time from start of cooldown of the cold QCM and the chamber cryoliner. The effusion cell heating was started at 220 min, and the final constant temperature of 124°C was reached at 255 min. The RTV560 material did not start producing appreciable contamination until the effusion cell temperature had reached about 120°C at 240 min.

The room-temperature QCM shows a cutoff at about 12 μg, which should be well within its measurement range. It was speculated that this early cutoff was caused by the contamination material collecting on the QCM in a soft form, which damps the mechanical vibration in the crystal.

The surface area of the sample plate exposed to the contamination flux was about 15 cm^2. Thus, assuming the deposition rate was the same as the cold QCM, the sample plate collected about 60 μg/min.

3.3.2.2 QCM Measurements of Contaminants

A typical mass spectrum of the OGC environment while contamination of the sample plate by RTV560 was underway is shown in Fig. 13. Several distinctive peaks can be seen in the figure. Those at 16, 17, and 18 amu can be attributed to water in the system; that at 28 to nitrogen; and that at 32 to oxygen. These peaks are the result of having residuals of these gases in the chamber or a small air leak into the chamber.

When contamination of the sample plate was ended, it was stowed behind its isolation valve, and the chamber was warmed to room temperature and opened to remove the RTV560 sample material. The chamber was then returned to vacuum conditions and the cryoliner was cooled again to bring the chamber back to its precontamination state. Finally, the sample plate was reinserted into the chamber and warmed to room temperature. A mass spectrum obtained after warmup is shown in Fig. 14. The intensity of this spectrum is less than that shown in Fig. 13, but many of the same peaks can be seen.

The amount of time that the QMS amu sweep remains at a sampled point affects the signal-to-noise ratio with a longer dwell time, resulting in a greater signal-to-noise ratio. There is a penalty to pay for longer dwell times, however, and that is a longer time to sweep the total amu range with the attendant danger that a transient might be missed. The dwell time used for spectra shown in Fig. 13 was 120 msec. This corresponds to a noise equivalent pressure of 2.5×10^{-11} torr. The dwell time used to obtain the spectrum in Fig. 14 was 60 msec. This value yields a noise equivalent pressure of 5.0^{-11} torr. Some of the peak heights in the spectra presented are in this noise range; and if those that are below are ignored, it reduces the number of peaks to consider. A threshold value of 10^{-10} torr was chosen for Figs. 13 and 14.

3.3.3 STM Discussion

The mechanical and thermal operation of the STM was sufficient to allow cryogenically collected samples to be transported to the OGC for analysis. However, for cases where only a small amount of material is condensed on the sample plate, difficulty may be experienced in analyzing the mass spectrometer data because of small signal problems. To improve this situation, the coupling volume between the mass spectrometer and STM sample should be reduced through redesign. Furthermore, a modern, high amu mass spectrometer system should be procured for the OGC. Because the STM successfully demonstrated its sample transfer capability, it can also be used to bring a contaminated ATR plate to the OGC for analysis.

3.4 SURFACE ACOUSTIC WAVE (SAW) DEVICE

3.4.1 Basic SAW Theory, Description, and Advantage in Principle

QCMs (as well as many other piezoelectric transducers) use acoustic wave propagation in the bulk of the piezoelectric material. Only since the early 1960s has there been much interest in the utility of surface acoustic waves even though the existence of this type of wave was established by Lord Rayleigh in the 19th century (Ref. 4). In the case of surface acoustic waves (or Rayleigh waves), the wave motion is bound to a plane surface. This means that the surface wave is accessible as it travels along. It is this accessibility that caught the attention of physicists and electronics engineers working in communication and radar fields. This geometrical freedom for sampling, modifying, or interacting with the surface wave permitted a realization of a wider number of devices than possible with bulk wave devices. In addition, the electromagnetic fields associated with the surface wave propagation on piezoelectric media extend out beyond the surface, and this gives the possibility of electromagnetic interaction of the waves with solids not in mechanical contact with the surface.

In the QCM, the bulk wave is a transverse wave, i.e., particle displacement is transverse to the direction of propagation. The density and elastic constants of quartz limit the bulk wave frequency to 10 to 15 MHz. In the case of a surface acoustic wave, the particle motion at the surface is a retrograde elliptical path. The motion can be decomposed into two orthogonal components: one in the direction of propagation and the other normal to the surface. Because the particles at the surface are less restrained than particles deep in the interior, the SAW frequency can be orders of magnitude larger than the frequency of a bulk device. In addition, the surface wave velocity is lower than the bulk velocity, which means surface wave energy can only propagate a short distance into the bulk medium.

A SAW is normally generated (via the piezoelectric effect) by a radio frequency (RF) voltage applied to an array of metal electrodes on the surface (See Fig. 15). This electrode array is known as an interdigital transducer (IDT), which consists of a number of pairs of metal electrodes and separating spaces that are attached to the surface of a piezoelectric material as shown in Fig. 15. These electrode pairs are subjected to an RF voltage that sets up a surface acoustic wave having the same frequency as the applied voltage. A second IDT is placed in line with the wave generating IDT to detect the surface acoustic wave. Because the SAW exists on the solid surface, the operating frequency is determined by the repeat spacing (d) of the IDT fingers (See Fig. 15) and the Rayleigh wave velocity (V_R) of the piezoelectric material. The SAW wavelength (λ) is equal to d, and the frequency is

$$f = \frac{V_R}{d} \text{ Hz} \tag{5}$$

At present, IDTs are usually made using microphotolithographic techniques that are state-of-the-art limited to IDT finger widths of ~ 0.25 μm. This means SAW wavelengths are limited to ~ 1 μm. Assuming quartz for the piezoelectric material, $V_R = 3.1 \times 10^5$ cm/sec, the maximum operating frequency is nominally 3 GHz. However, most of the SAW devices presently used operate in the 100- to 200-MHz range because of difficulty in obtaining suitable RF amplifiers and electrical connections to permit stable operation.

When a thin film of material is placed on the surface of a SAW device, the material interacts with both the longitudinal and vertical shear components of the Rayleigh wave. If the film material thickness is < 1 percent λ, which would normally be the case for AEDC microbalance applications, then compressional waves will not exist (Ref. 5). Therefore, the primary interaction is through the vertical shear component of the Rayleigh wave, and this interaction results in changes in SAW amplitude, velocity, phase, harmonic constant, etc. SAW devices for microbalance applications are easily configured to monitor changes in either SAW amplitude or velocity, but the measurement of velocity perturbations offers superior precision (Ref. 6). The configuration most commonly used is the delay line oscillator system shown in Fig. 16. The RF power amplifier provides feedback from the output IDT to the input IDT, which stabilizes the system at the IDT resonant frequency. The resonant frequency (or wave velocity) of the device is shifted when the surface of the device is subjected to added mass, and the change in frequency can be measured very accurately with digital frequency counters.

A relationship for the shift in frequency as a function of the mass added to the SAW device surface was first developed by Auld (Ref. 5) and later put into a workable form by Wohltjen (Ref. 6). This relationship is

$$\Delta f = \underbrace{\left(k_1 + k_2\right) f^2 h \varrho}_{\text{term A}} - \underbrace{k_2 f^2 h \left[\frac{4\mu'}{V_R^2}\left(\frac{\lambda' + \mu'}{\lambda' + 2\mu'}\right)\right]}_{\text{term B}} \tag{6}$$

where k_1 and k_2 are constants related to the surface particle velocity components, λ' is the Lame' constant for material added to the surface, and μ' is the shear modulus of the material added to the surface. From Ref. 7 it can be seen that λ'/μ' varies from ~ 0.1 → ∞ for a wide range of materials, and this limits the range of $(\lambda' + \mu')/(\lambda' + 2\mu')$ to ~ 0.5 → 1.0. The shear modulus-dependent term B becomes negligible if $4\mu'/VR^2$ is < 0.1ϱ. Assuming this to be the case, the frequency shift expression becomes

$$\Delta f = \left(k_1 + k_2\right) f^2 h \varrho \tag{7}$$

which is very similar to the relationship for QCMs given by Eq. (1). For YX-cut quartz, $k_1 = -9.33 \times 10^{-8}$ m^2 sec/kg and $k_2 = -4.16 \times 10^{-8}$ m^2 sec/kg (Ref. 6). Equation (7) can now be written as

$$\Delta f = -1.349 \times 10^{-6} f^2 \varrho h \tag{8}$$

for ϱ in gm/cm^3 and h in cm. The QCM relation of Eq. (1) can also be rewritten as

$$\Delta f = -2.26 \times 10^{-6} f^2 \varrho h \tag{9}$$

First inspection of Eqs. (8) and (9) might indicate that SAW and QCM devices have comparable sensitivity. However, a nominal operating frequency for a SAW device is 100 MHz, whereas the AEDC QCMs operate at 10 MHz. This means that the 100-MHz SAW device can be a factor of 59.7 more sensitive than presently used QCMs.

Equation (6) demonstrates a basic difference between a SAW microbalance and a QCM. This difference is manifested by the Term B, which shows that the vertical shear component of the SAW interacting with the material deposit brings the elastic properties of the material into the relation. In contrast, the QCM bulk wave has its oscillations transverse to deposit thickness; that is, the deposit mass oscillates with the QCM crystal (strictly true only for a solid deposit). An equivalent Term B does not appear for the QCM, at least for solid deposits. The QCM measures the deposited mass by detecting the change in frequency induced by the total increase in mass of the oscillator, whereas the SAW device measures deposited mass by detecting the change in SAW frequency caused by deposited mass only.

Both SAW devices and QCMs exhibit sensitivity to temperature change. The use of ST-cut quartz provides a nearly zero first-order temperature coefficient of delay time and wave velocity for temperature from 50 to 0°C (Ref. 8). Selection of optimum cuts for cryogenic temperature operation has yet to be done. The same scheme of using a dual-sensor system, one an active device and the other a reference device, mixing the signals, and reading the difference frequency can be used to circumvent SAW device temperature sensitivity as was done for QCMs. There is another major difference between SAW devices and QCMs in this regard. Both SAW sensors (active and reference) can be easily formed on a single crystal. Furthermore, this crystal can be rigidly mounted by its back side to a heat sink, because the SAW device uses only a surface wave. Therefore, both SAW sensors are more likely to be at the same temperature than the crystals of a QCM.

It is appropriate at this point to review the advantages that a SAW microbalance has, in principle, over a QCM.

1. The SAW device can offer up to ~ 5.4×10^4 more sensitivity if 3-GHz operation can be achieved.

2. The SAW device can offer better temperature stability because both active and reference sensors can be on a single crystal.

3. SAW devices can be made extremely small (10^{-4} cm^2, Ref. 6), which means little interference with the measurement environment.

4. SAW devices need only be polished on the active surface, which reduces costs and provides for rugged mounting of the device via the back (or nonactive) surface.

5. Items 3 and 4 acting together will permit multiple SAW devices to be used in an AEDC space chamber, which will permit adequate mapping of directionally dependent contamination flux.

3.4.2 Review of Naval Research Laboratory (NRL) Work with SAW Devices

Wohltjen and coworkers at the NRL have pioneered the development of SAW devices for vapor sensing applications (Refs. 6, 9, and 10). In Ref. 6 Wohltjen demonstrated that various films of such substances as poly (methyl methacrylate), cis-poly (isoprene), and poly (ethylene maleate) could be deposited on a SAW delay line oscillator surface and that the frequency shift behavior followed the prediction of Eq. (8). In Ref. 9 Wohltjen et al. demonstrated the dual delay line oscillator concept for increased temperature stability. In Ref. 10, Wohltjen and associates showed that the elastomeric polymers of Ref. 6 could be used for detecting organic vapors. As the vapors of interest diffused into the polymer coatings and were either chemisorbed or physisorbed, the mass of the coating increased, and the frequency of the SAW device was observed to change. Organic vapors of low ppm concentration in dry air were successfully detected and ppb detection limits were deemed possible (Ref. 10). Wohltjen (Ref. 10) has also studied the time response of his SAW devices when they are exposed to organic vapors in an air carrier stream. For a 31-MHz SAW device, the response time was ~ 10 sec. A Fickian vapor diffusion into the coating would have a diffusion time related to the square of the thickness, and, as operating frequency increases, the thickness needed to produce the same frequency shift (when mass loaded) decreases with the square of the frequency. Therefore, going from a 31-MHz SAW device to a 112-MHz SAW device, the response time would be expected to be ~ 6 sec, whereas it was measured to be ~ 10 sec. Wohltjen has speculated that his simple diffusion model must be modified to account for other processes responsible for the response time behavior.

3.4.3 Review of Sandia National Laboratory (SNL) Work with SAW Devices

In contrast to the NRL work, Martin and colleagues (Refs. 11, 12, and 13) have pursued development of a SAW vapor sensor by making the SAW sensor itself porous rather than coating a solid SAW device with a porous, elastomer film. In the SNL approach, a SAW sensor was fabricated with ZnO (which is porous and piezoelectric) on a silicon substrate (See Fig. 17). The IDTs and reflector arrays were defined by microphotolithography. Similar to the NRL work, the SAW device was used as the frequency control element of an oscillator circuit and operated at 109 MHz.

ZnO was chosen because it gave the SAW device sorptive properties related to its porous, polycrystalline nature. The surface dipole nature of ZnO gives enhanced adsorption of polar molecules, and the porous nature of the coating allows vapors to penetrate into the interior of the device. Following Auld's work (Ref. 5), the mass sensitivity relation of the device was calculated and was experimentally verified to be

$$\Delta f = -1.62 \times 10^{-6} f^2 \varrho h \tag{10}$$

which is very similar to the sensitivity predicted for a quartz device [See Eq. (8)].

Martin and colleagues (Ref. 13) also examined the transient behavior of their device when it was exposed to dry air seeded with low concentrations of organic vapors, and this behavior is illustrated in Fig. 18. They discovered a short-term and long-term sorption process. The short-term process was typically on the order of 60 sec, and the long-term process was on the order of 400 sec. Using the relationship of Eq. (10), the surface coverage for the short-term process was calculated and plotted versus the vapor pressure of the organic vapor in the air carrier. An excellent fit to a Langmuir isotherm was obtained, which meant that the short-term process corresponded to equilibrium monolayer adsorption on the exposed surface. The long-term process was initially speculated to be a Fickian diffusion process, which is the initial view taken by the NRL workers for their observed transient response. A plot of long-term responses as a function of organic vapor molar volume was constructed and is depicted in Fig. 19. Noting that

$$\text{molar volume} = N_A \delta^3 \tag{11}$$

where N_A is Avogadro's number and δ is a characteristic molecular dimension, the equilibrium time for the long-term process *increases* for *smaller* molecules. This is just the opposite to be expected from a purely Fickian diffusion process. Martin has speculated that the smaller molecules are able to diffuse through smaller pores, which the larger molecules are unable to penetrate; therefore, the smaller molecules can take a much longer time before

reaching a final site in the ZnO film. Obviously, a good explanation for the time response behavior of both the porous SAW and the porous films on SAW devices is lacking, but the implications of Fig. 19 are awesome. Not only can a SAW device determine how much of a deposit is on the device, but it can also determine what kind of molecule has been deposited based on response time and molecular size. Noting that (Ref. 14)

$$\delta = 1.329 \times 10^{-8} \left(\frac{M}{\varrho}\right)^{1/3} \tag{13}$$

where M is molecular weight and ϱ is density, it can be seen that species can be identified from a calibration curve such as Fig. 19.

3.4.4 AEDC Requirements

The success of SAW devices as vapor sensors indicates that they could offer some real measurement advantages over QCMs if they can be tailored to the cryovacuum environment of the AEDC space chambers area. For a contamination monitor to be valuable in measuring the amount of material that condenses on a cryocooled surface, it must be possible to cool the sensing surface to the same temperature. There is no physical problem with operating a SAW crystal at cryogenic temperature, because QCMs, which are similar, regularly operate at temperatures down to 20 K. However, the SAW crystal must either be separated from the RF electronics package as is done for QCMs, or the crystal and electronics must be packaged together on a small circuit board that can function in the cryovacuum environment. The capability to control the surface temperature of the SAW device is required to prevent cooling of the device too rapidly and to heat the surface to purge it of condensation when the device reaches saturation limits.

Using SAW devices for species identification requires either a porous film on the SAW device surface or the SAW device itself to be porous in nature. The latter alternative appears to be the best approach, because the use of elastomeric films at cryogenic temperatures could be unsuitable. Because species identification will depend on the transient response of the device when it is exposed to the contaminating environment, provision will have to be made through some sort of microvalving system to expose the crystal surface for several minutes as the transient response is measured. Following this exposure, the valve must be closed and, if the saturation limits of the device have been reached, the SAW device surface must be warmed as noted earlier.

For SAW devices to detect and identify contamination sources, an AEDC space environment chamber must have multiple monitoring devices throughout the chamber. This requires that the devices have a low procurement and maintenance cost as well as being small

in size. Based on the size of QCMs, the size requirement will be on the order of a few cubic centimeters.

3.4.5 Microsensor Systems, Inc. SAW Device

3.4.5.1 Construction

To become familiar with the foibles of SAW microbalances and to attempt to adapt a SAW device to operation in a vacuum chamber, a prototype first-generation device was purchased from Microsensor Systems, Inc. The device is a dual delay line oscillator (158 MHz) fabricated with quartz. The active and reference crystals are glued to TO-8 printed circuit plug-in bases and mounted at the ends of circuit board extensions, which place them inside the vacuum chamber. The circuit board extensions pass through a mounting flange and are sealed with Epoxy. The electronics package is on the external portion of the device.

A schematic of the dual delay oscillator system is shown in Fig. 20. The system operates with a 5-VDC regulated power supply, and test points are provided on the circuit board for monitoring the resonant frequency of each oscillator as well as the difference frequency (a few hundred kHz). A nonzero frequency difference exists between the two oscillators because of inherent crystal and network differences.

3.4.5.2 Cooling of SAW Crystals

The SAW device crystals were cooled by bringing the plug-in base mounts into contact with liquid nitrogen-cooled copper plates. The cooling system is shown schematically in Fig. 21. The crystals were inserted by compressing the printed circuit board extensions until the crystals were in place, then allowing the boards to spring back to their original positions. A plastic spacer was then placed between the boards to wedge the crystal bases against the copper plates.

Actual cooling of a crystal surface is, of necessity, through the thickness of the crystal and the thickness of the bonding agent. If no heat load is directed at the crystal surface, that surface will approach the base temperature, given enough time. However, if a heat load does exist, the crystal surface will differ from the base temperature because of the conduction path.

3.4.6 Experimental Program

Preliminary operation of the cooled SAW device in a vacuum chamber did indeed indicate a mass increase as it condensed water vapor from the chamber environment. It also showed

that the device was sensitive to temperature changes, that the device's electronics had a stability problem, and at times, the device would cease operation for no apparent reason. Nonetheless, an experiment was devised to further check the operational characteristics of the SAW device.

3.4.6.1 Experimental Configuration

The experimental hardware consisted of (1) a vacuum chamber with a liquid nitrogen-cooled liner; (2) a source to furnish water vapor as the condensing species; (3) a liquid nitrogen-cooled QCM for use as a reference; (4) the liquid nitrogen-cooled SAW device; (5) a liquid nitrogen-cooled support for the source, QCM, and SAW device; and (6) instrumentation for recording test conditions.

3.4.6.1.1 Vacuum Chamber

The vacuum chamber used was the AEDC 2- by 3-ft chamber, which is evacuated by a 400 ℓ/sec turbomolecular vacuum pump. The pump has a liquid nitrogen-cooled trap between it and the chamber, and the chamber is fitted with a full-coverage liquid nitrogen-cooled cryoliner. The pressure in the chamber is monitored with a Bayard-Alpert-type ion gage. In the configuration used for this test, the chamber pressure could be held at about 8×10^{-6} torr.

3.4.6.1.2 Water Vapor Source

Water vapor was used as the test medium because it will condense on liquid nitrogen-cooled surfaces and remain there with little reevaporation. This assured that the vapor that did not impact the sensor surfaces would impact and be held by the other liquid nitrogen-cooled surfaces in the chamber; thus, only that vapor that came directly from the source orifice would condense on the sensor.

The water vapor was produced by a glass bulb filled with distilled water. This bulb was connected by a tube and a leak-type control valve to an aluminum plenum much larger in diameter than the tube and heated to a constant temperature (300 K) by a resistance heater and temperature-controlled power supply. The plenum had a 400-μm-diam by 20-μm-thick orifice for passing the water vapor into the chamber. A bypass line was connected to the vapor supply system through a valve so that initial pumpdown of the system could be done more rapidly than through the orifice. Pressure in the supply plenum was read using a capacitance-type absolute pressure gage.

3.4.6.1.3 SAW Device and QCM Positioning

The sensing crystal surfaces of the SAW device and the QCM were placed in the same relative positions to the water vapor source orifice. This was accomplished by mounting the two crystals on radii of a common 26.24-cm-diam circle and then placing the source orifice on the centerline of this circle at an axial distance of 12.94 cm away. In this way, both sensors were exposed to the same vapor flux from the source orifice. The SAW device was held in place by its flange mount, and the source and QCM were held in place on a liquid nitrogen-cooled support. A schematic of the in-chamber setup is shown in Fig. 22.

3.4.6.2 Source Flux Calculation

The water vapor emitted by the source orifice that impacts a sensor surface located some distance away can be calculated by (Ref. 2)

$$m_i = \frac{B(\theta_1) \cos \theta_1 \cos \theta_2}{\omega \pi R^2} m_o \tag{13}$$

where m_i is the flux incident on the sensor surface; R is the line-of-sight distance between the orifice and the sensor; θ_1 and θ_2 are the angles between the normals and the line of sight for the orifice and the sensor, respectively; B (θ_1) and ω account for orifice effects on the flow; and m_o is the flow leaving the orifice. The flow leaving the orifice can be determined by (Ref. 15)

$$m_o = \omega A \left(\frac{m}{2 \pi KT}\right)^{1/2} \left(P_o - P_c\right) \tag{14}$$

where ω is again an orifice correction term, A is orifice area, m is molecular mass, K is Boltzmann's constant, T is absolute temperature of the flow, P_o is the pressure in the source, and P_c is the test chamber pressure.

The amount of water vapor flux at the sensing surfaces of both the QCM and the SAW device as calculated from Eqs. (13) and (14) was $m_i = 1.73 \times 10^{-10}$ gm/cm^{2}sec. This flux was held constant over the entire test period.

3.4.6.3 Measured Mass Accumulation

The amount of incident flux that condenses on a surface is determined by the condensation coefficient, or $m_c = C_c m_i$ where m_c is the condensed mass flux; m_i is the incident mass flux; and C_c is the condensation coefficient. This coefficient can be different from one case to another, depending on surface and flux conditions, but will normally be between 0.5 and

1.0. For water vapor condensing on a liquid nitrogen-cooled surface in a vacuum, the condensation coefficient would be expected to be about 1.0.

The amount of mass accumulated on the QCM during a test period in which the vapor source temperature and pressure were held constant is shown in Fig. 23. The ordinate in Fig. 23 is the beat frequency from the QCM and only needs to be multiplied by a constant to convert it to mass. The average condensed flux measured for the QCM during this test was $m_c = 1.68 \times 10^{-10}$ gm/cm^{2}sec. This leads to a condensation coefficient of 0.97 for the QCM.

The amount of mass accumulated on the SAW device during the same test period is shown in Fig. 24. (The SAW device frequency decreases with increasing mass deposit.) Again, the ordinate in this figure is the beat frequency and converts to mass by being multiplied by a constant. The large-scale variations before about 1 hr and after about 4 hr were caused by changes in the SAW device temperature. Figure 25 is a small portion of Fig. 24 expanded to show that there was a considerable amount of short-term variation in the output from the SAW device. The long-term average of the amount of condensed flux for the SAW device during the test period was $m_c = 1.08 \times 10^{-10}$ gm/cm^{2}sec. The condensation coefficient calculated for the SAW device is then 0.62. The change in frequency as a function of mass accumulation was approximately 95 times larger for the SAW operating at 158 MHz, compared to the 10 MHz QCM.

3.5 FIBER-OPTIC ATR MEASUREMENTS

ATR methods for identification of contaminant films have demonstrated capability, but the problem of bringing an IR beam into and out of a test chamber without compromising IR sensor testing has not been resolved. Three recent technological developments may yet render ATR methods useful for *in-situ*, online identification of contaminant species. Chalcogenide glass fibers have been developed for transmission in the 2- to 11-μm range, and tunable solid-state IR sources have also been developed for this range of wavelengths. This means that the IR radiation can be generated by a small, inexpensive source rather than an expensive, cumbersome FTIR spectrometer and that the IR radiation can be brought into the test cell with an optical fiber. At the University of Tokyo, unclad optical fibers have been used to detect organic gases surrounding the fibers via molecular absorption of the IR evanescent wave that penetrates the region near the unclad fiber surface. It therefore appears feasible to pass tunable IR radiation through a chalcogenide fiber that has an unclad section exposed to the cryocontaminant environment and analyze the output signature normalized to the noncontaminant signature as a method of identifying the contaminant species on the unclad fiber surface.

Laboratory experiments were devised to determine the feasibility of fiber-optic absorption for contaminant species identification in the space chambers. A 2-m length of chalcogenide fiber was obtained from Infrared Fiber Systems, Inc. An Optronic infrared grating spectrometer with a globar attachment was used as a radiation source to determine the spectral transmittance of the fiber. A photograph of the experimental setup is shown in Fig. 26. Transmitted radiation was detected with a mercury cadmium telluride detector cooled to liquid nitrogen temperature.

An example of the transmitted spectra is shown in Fig. 27. Measurable transmittance was limited to a band in the 6.0- to 7.0-μm spectral region. The magnitude of the transmitted energy was not adequate to provide the necessary signal to noise required for contaminant absorption measurement. Although considerable effort was made to optimize the optical coupling between the fiber and spectrometer and between the fiber and detector, no improvement in throughput was made. Attenuation curves for this fiber indicate that loss varies from 1 to 10 db/m across this spectral range. Even with this loss it would be expected that measurable transmittance could be obtained with a 2-m fiber.

3.6 LASER MICROPROBE

The work described in this section concentrates on a portion of the contamination technology work that was dedicated to development of a laser microprobe device for online identification of cryocontaminant species. The work involved the following parts: learning and modeling the physics of surface-enhanced Raman scattering (SERS), assembling and using laboratory apparatus for SERS evaluation experiments, and developing a concept for use of the laser microprobe in the AEDC space chambers.

3.6.1 Description of Normal Raman Scattering

The needs for online contaminant species identification and the limitations of the best available techniques have made it necessary to search for new techniques. One of the most useful diagnostics for surface and surface-related phenomena that has been developed over the last 10 years is the laser microprobe technique. In general, a laser beam is made to impinge upon a surface of diagnostic interest. Surface molecules interacting with the laser emit radiation as a result of ionization, fluorescence, or scattering processes. For AEDC applications, the use of a high-power laser beam on a contaminant-coated surface to produce a glowing plasma for analysis might not be too practical because of the accompanying infrared radiation as well as thermal impulse. The use of fluorescence is complicated by the fact that different species require different excitation wavelengths and that chemical bonding of molecules to a surface can suppress fluorescence. Scattering techniques avoid all of these difficulties, and the particular technique of Raman scattering can be used to identify all diatomic and polyatomic species.

When a laser beam interacts with gases, liquids, or solids, scattering of the incident radiation occurs. Spectral analysis of the scattered radiation will reveal not only the incident laser wavelength, but components shifted in wavelength with respect to the laser wavelength. In the classical sense, Raman scattering results from a modulation of the incident radiation frequency by the characteristic motions of the scattering species. For most cryodeposit lattices and structures, the charateristic scattering frequencies can be categorized as either lattice modes, which correspond to the intermolecular collective degrees of freedom, or vibrational modes, which correspond to the intramolecular degrees of freedom. Scattered radiation down-shifted relative to the laser frequency is referred to as the Stokes components (increased wavelength), and up-shifted radiation is referred to as the anti-Stokes components (decreased wavelength). Figure 28 depicts a typical, normal Raman Stokes spectrum that could be obtained from a cryodeposit. It can be seen that the lattice mode signature lies within approximately 200 cm^{-1} of the frequency of an exciting laser source. The molecular vibrational mode signatures generally lie from approximately 500 cm^{-1} to 4,000 cm^{-1} of the excitation line. It is these vibrational signatures that provide Raman scattering with such a high degree of molecular specificity, because every diatomic and polyatomic molecule has characteristic vibrational frequencies. The entire Raman spectral region of interest for cryodeposit analysis lies in a 3,500-cm^{-1}-wide spectral region. Assuming excitation radiation at 5,000 Å, the spectral region of interest is only 1,100 Å wide, and such a narrow region can be easily scanned for species identification.

Raman scattering from solid phase species has been studied at AEDC (Ref. 16). Analysis of these experimental results has shown that a cryodeposit thickness of approximately 10 μm is required for obtaining a signal level suitable for accurate measurements. Therefore, to use Raman scattering for analysis of cryodeposits at the monolayer level, advantage must be taken of the surface-enhanced Raman scattering phenomenon.

3.6.2 Description of Surface Enhanced Raman Scattering (SERS)

SERS was discovered 16 years ago by researchers who observed high-quality Raman spectra from pyridine adsorbed on electrochemically roughened silver electrode surfaces. Three years later, other research groups concluded that the Raman scattering cross section must have been enchanced by a factor of 10^5 to 10^6. Since that time, numerous university and government research laboratories have completed experiments that define the characteristics of the SERS phenomenon. These characteristics can be summarized as follows:

1. SERS occurs for all diatomic/polyatomic molecules deposited on the surfaces of a few metals such as silver, copper, indium, aluminum, lithium, potassium, and sodium.

2. A submicroscopic surface roughness of at least 10 to 100 nm is required.

3. Enhanced scattering can be observed for molecules in layers separated from the metal surface by tens of nanometers.

4. The dependence of the Raman-scattered intensity on excitation frequency deviates significantly from the fourth-power frequency dependence observed for normal Raman scattering.

5. The intensities of the Raman bands generally decrease with increasing vibrational frequency.

6. The Raman scattering is completely depolarized.

7. Varying surface roughness requires different excitation frequencies to achieve maximum enhancement for a given vibrational frequency.

8. Normal Raman scattering selection rules are modified, which results in spectral features not observed in the gas phase.

9. Even in the absence of an adsorbed species, SERS surfaces display a weak continuum spectrum.

To date, no completely satisfactory, all-encompassing theory is available to explain the SERS phenomenon. However, the theoretical mechanisms for the enhancement can be divided into two classes: electromagnetic and chemical. The chemical mechanism involves the adsorbate-substrate system. Chemisorption is an example of the chemical mechanism. The magnitude of the chemical mechanism is a subject of considerable controversy, but it is fairly clear that the electromagnetic mechanism is dominant. Because of this and the physical nature of cryosorption, the chemical mechanism was ignored in the development of analytical models for AEDC applications.

The electromagnetic mechanism involves the excitation of conduction electron resonances. An initial phenomenological approach is helpful in understanding the enhancement mechanism. A plasma is normally viewed as a dilute, completely ionized, turbulent state of matter. However, a metal can also be viewed as a plasma. This condensed matter plasma has a fixed background of positive ions with a host of electrons free to move about throughout the plasma. The high density of the plasma allows quantum mechanical influences to occur that bind the ions and electrons into a stable ensemble. The energy quanta associated with the oscillations of electrical charge within the condensed matter plasma are called plasmons. It is the interaction

of electromagnetic radiation with the surface plasmons of a metal that causes the enhanced scattered radiation.

Assume an isolated, spherical, metal particle of radius "a" and a complex dielectric function, ϵ, interacting with laser radiation of frequency ω_o in a surrounding medium of dielectric constant ϵ_o. The size of the particle is assumed to be small compared to the wavelength of incident radiation, which avoids consideration of electrodynamics. The induced dipole moment is (Ref. 17)

$$\bar{p}(\omega) = \left[\frac{\epsilon(\omega_o) - \epsilon_o}{\epsilon(\omega_o) + 2\epsilon_o}\right] a^3 \bar{E}(\omega_o) \tag{15}$$

As the real part of ϵ (ω_O) approaches a value of $-2\,\epsilon_O$, a resonance condition will occur. It is this type of resonance that is responsible for the SERS phenomenon, and it serves as the basis for two of the most prominent electromagnetic models for SERS.

3.6.3 Spheroidal Electromagnetic Model of SERS

To build on the case of the isolated, spherical, metal particle, it was necessary to model the surface in some manner. The spheroidal representation from Refs. 18, 19, and 20 was one of the simplest models. The SERS surface was assumed to consist of a random array of metal spheroids. On average, these metal spheroids (See Fig. 29) have a semi-major axis of length "a" and a semi-minor axis of length "b." The aspect ratio was defined to be a/b. If $a/b < 1$, the protrusion was an oblate spheroid; if $a/b > 1$, a prolate spheroid. As shown in Fig. 29, a molecule was assumed to exist at a distance "d" above the apex of the spheroid. It was assumed that $a,b < \lambda_O$, the wavelength of the laser excitation. To simplify the problem, the spheroid was replaced by a point dipole given by

$$\bar{p} = a_s \bar{E}_O \tag{16}$$

where

$$\alpha_s = \left[\frac{ab^2\epsilon_O}{3}\right]\left\{\frac{\epsilon(\omega_O) - \epsilon_O}{\epsilon_O + [(\epsilon(\omega_O) - \epsilon_O)A]}\right\} \tag{17}$$

where A is a geometric depolarization factor given by

$$A = \frac{ab^2}{2}\int \frac{ds}{(s + a^2)^{3/2}(s + b^2)} \tag{18}$$

The interaction of the incident laser field with the spheroidal particle excites a plasmon resonance that enhances the electric field at the location of the molecule. This electric field induces the Raman molecular polarization, and the resulting dipole moment (Ref. 17) oscillating at the Raman frequency, ω_r, is

$$\bar{p}_m(\omega_r) = \frac{2\alpha_r\alpha_s(\omega_O)\bar{E}_O}{\epsilon_O r^3} \tag{19}$$

where r is the axial distance (a + d) from the center of the spheroid to the molecule. In turn, the field of the molecular dipole polarizes the spheroid at the Raman frequency,

$$\bar{p}_s(\omega_r) = \frac{2\alpha_s(\omega_r)\,\bar{p}_m(\omega_r)}{\epsilon_O r^3} \tag{20}$$

The normal Raman scattering dipole moment is

$$p_m(\omega_r) = \alpha_r E_O \tag{21}$$

Therefore, the spheroidal particle scattering is actually an enhancement of the normal Raman scattering by a factor

$$(EF)^{1/2} = \frac{4\alpha_s(\omega_r)\alpha_s(\omega_O)}{(\epsilon_O r^3)^2} \tag{22}$$

Then,

$$(EF)^{1/2} = (4/9)\left(ab^2/r^3\right)^2 \left|\frac{\epsilon(\omega_r) - \epsilon_O}{\epsilon_O + [(\epsilon(\omega_r) - \epsilon_O)A]}\right| \left|\frac{\epsilon(\omega_O) - \epsilon_O}{\epsilon_O + [(\epsilon(\omega_O) - \epsilon_O)A]}\right| \tag{23}$$

Because scattered intensity varies with the square of the induced dipole moment, the total enhancement factor is

$$(EF) = (16/81)\left(ab^2/r^3\right)^4 \left|\frac{\epsilon(\omega_r) - \epsilon_O}{\epsilon_O + [(\epsilon(\omega_r) - \epsilon_O)A]}\right|^2 \left|\frac{\epsilon(\omega_O) - \epsilon_O}{\epsilon_O + [(\epsilon(\omega_O) - \epsilon_O)A]}\right|^2 \tag{24}$$

This expression does not account for the field concentration at the spheroidal tip — the so-called lightning rod effect. However, in Ref. 19 it has been shown that for the spheroidal model, this effect can be included by a multiplicative factor

$$\gamma^4 = \left[3/2(a/b)^2\,(1 - A)\right]^4 \tag{25}$$

For the vacuum conditions of SERS sample plates to be used in the space chambers area, $\epsilon_0 = 1$. The complex dielectric function for the sample plate surface can be written as a sum of real and imaginary parts

$$\epsilon = \epsilon_1 + i\epsilon_2 \tag{26}$$

Using this formulation, changing from an optical frequency domain to wavelength, and completing the operations for the squares of the absolute values, Eq. (24) takes the form

$$EF = (a/a+d)^{12} \left\{ \frac{[\epsilon_1(\lambda_r) - 1]^2 + \epsilon_2^2(\lambda_r)}{[(1-A) + A\epsilon_1(\lambda_r)]^2 + \epsilon_2^2(\lambda_r)} \right\} \left\{ \frac{[\epsilon_1(\lambda_O) - 1]^2 + \epsilon_2^2(\lambda_O)}{[(1-A) + A\epsilon_1(\lambda_O)]^2 + \epsilon_2^2(\lambda_O)} \right\} (1 - A)^4 \tag{27}$$

Defining

$$ASP = a/b \tag{28}$$

and

$$ESPH = \left[1 - \left(1/ASP^2\right)\right]^{1/2} \tag{29}$$

then the solution of Eq. (18) for the case of a prolate spheroid (ASP > 1) is

$$A = \frac{\left[\ln\left(\frac{1 + ESPH}{1 - ESPH}\right) / 2\,(ESPH)\right] - 1}{(ASP)^2\,(ESPH)^2} \tag{30}$$

A similar expression can be derived for the oblate case.

Equation (27) can be used to model the expected Raman scattering enhancement factor for the case in which the sample plates are made by oblique angle deposition of a metal on a substrate of SiO_2 posts produced by either plasma etching (Ref. 21) or by microlithography (Ref. 18). For these types of sample plates, electron microscope photography has shown that the deposited metal particles approximate prolate spheroids.

3.6.4 Hemi-Spheroidal Electromagnetic Model of SERS

The hemi-spheroidal model was first proposed in Ref. 22. In this model, the surface of the SERS sample plate is characterized by hemi-spheroidal protrusions sticking out of an underlying planar substrate (See Fig. 30). The full derivation of the enhancement factor relations can be found in Ref. 22; therefore, only the pertinent assumptions and results will be presented in this technical report.

The hemi-spheroids were characterized by a semi-major axis of length "a" and semi-minor axis of length "b" with aspect ratio of a/b as before. Mutual interaction between hemi-spheroids was neglected. A cryodeposited molecule was assumed to reside at a distance "d" from the tip of the hemispheroid. The substrate was assumed to be inert and to have a dielectric constant roughly equal to the surrounding medium. The physical dimensions of the hemi-spheroids were assumed to be small in comparison to the wavelength of the excitation laser beam.

As shown in Ref. 23, the enhancement factor for Raman scattering could be expressed as

$$EF = \left| AMP(\omega_O) \right|^2 \left| AMP(\omega_r) \right|^2 \tag{31}$$

where AMP(ω) was an amplification factor and the frequency designations were the same as for the spheroidal model. For prolate hemi-spheroids, the amplification factor was given as

$$AMP(\omega) = 1 + L \left[\frac{\epsilon_o - E(\omega)}{\epsilon(\omega) - \epsilon_o P} \right] \tag{32}$$

where, as before, ϵ_o was the dielectric function of the hemi-spheroids. The factors L and P were defined in terms of the associated Legendre functions of the second kind, Q_1, and the hemi-spheroidal coordinates ξ_o and ξ_l that defined the position of the spheroid and molecule, respectively.

$$L = \xi_o \, Q_1'(\xi_l)/Q_1(\xi_o) \tag{33}$$

and

$$P = \xi_o Q_1'(\xi_o) \, / \, Q_1(\xi_o) \tag{34}$$

$$\xi_o = a/(a^2 - b^2)^{1/2} \tag{35}$$

and

$$\xi_l = (a + d)(a^2 - b^2)^{1/2} \tag{36}$$

$$Q_1(\xi) = (\xi/2) \left[\ln \left(\frac{\xi + 1}{\xi - 1} \right) \right] - 1 \tag{37}$$

and

$$Q_1'(\xi) = (1/2) \left[\ln \left(\frac{\xi + 1}{\xi - 1} \right) \right] - (\xi/\xi^2 - 1) \tag{38}$$

Using Eq. (26), changing from an optical frequency domain to wavelength, and completing the operations for the squares of the absolute values, Eq. (31) takes the form

$$EF = \left\{ \frac{[(L - P) + (1 - L)\,\epsilon_1(\lambda_r)]^2 + [(1 - L)\,\epsilon_2(\lambda_r)]^2}{[\epsilon_1(\lambda_r) - P]^2 + \epsilon_2^2(\lambda_r)} \right\} \times \left\{ \frac{[(L - P) + (1 - L)\,\epsilon_1(\lambda_O)]^2 + [(1 - L)\,\epsilon_2(\lambda_O)]^2}{[\epsilon_1(\lambda_O) - P]^2 + \epsilon_2^2(\lambda_O)} \right\}$$

In addition to the definitions of Eqs. (28) and (29),

$$ESPHD = \left[(a^2 - b^2) / (a + d)^2\right]^{1/2} = \left[\frac{1 - [1/(ASP)^2]}{(a + d)^2}\right]^{1/2} (a) \tag{40}$$

Therefore,

$$\xi_O = (ESPH)^{-1} \tag{41}$$

and

$$\xi_1 = (ESPHD)^{-1} \tag{42}$$

A set of similar expressions can be derived for the oblate case.

Equation (39) can be used to model the expected Raman scattering enhancement factor for the case in which the sample plates are made by vacuum evaporation of metals onto glass or fused silica substrates or cellulosic substrates (Ref. 24). For these types of sample plates, electron microscopy has shown that the deposited metal particles approximate prolate hemi-spheroids.

3.6.5 Computational Work

3.6.5.1 Computer Model Results

The analytical relations for both the spheroidal and hemi-spheroidal models were coded as part of Program ERASP (Enhanced Raman Spectral Program) and made resident on the Space Systems Branch MicroVAX computer system. Input to the code included selection of laser wavelength, Raman shifts for molecules of interest, optical property constants for selected metals, resolution of wavelength, wavenumber, and aspect ratio steps, and selection of various coding parameters. These parameters permitted selection of analytical model, metal, and the type of calculation to be performed. Three types of calculations were possible: (1)

a calculation of enhancement factor as a function of aspect ratio with Raman shift as a parameter for a given laser wavelength and metal; (2) calculation of enhancement factor as a function of laser wavelength with aspect ratio as a parameter for a given Raman shift and metal; and (3) calculation of enhancement factor for a variety of molecular Raman shifts for a given laser wavelength, aspect ratio, and metal.

Two metals were selected for the calculations. Silver was chosen because it had been the overwhelming choice for preparation of SERS sample surfaces in most research laboratories. This was because of the excellent optical properties of silver in the ultraviolet through visible spectral region, the ready availability of silver, and the ease of vacuum deposition of silver on surfaces of all types. Indium was also chosen because of its ready availability, low cost, and excellent record of use in the cryovacuum environment.

The optical properties of silver were taken from Ref. 25. As usual, the optical constants reported were the components of the complex refractive index, m, which could be related to the components of the complex dielectric function, ϵ, using relations from Ref. 25.

$$m = n + inK = n + ik \tag{43}$$

where n is the refractive index, K is the extinction coefficient, and k is the absorption index. Assuming a nonmagnetic conductor,

$$m^2 = \epsilon \tag{44}$$

Threfore,

$$\epsilon_1 = n^2 + k^2 \tag{45}$$

and

$$\epsilon_2 = 2nk \tag{46}$$

Using the n,k values from Ref. 25 and Eqs. (45) and (46), the ϵ_1, ϵ_2 values for silver were calculated and plotted. A curve was fit to the plots, and the fitting coefficients were entered into the Code ERASP input file. The optical constants from indium were taken from Ref. 26, calculated and plotted, and the curve fitting coefficients were entered into the Code ERASP input file. The indium ϵ_2 values were an order of magnitude larger than the silver values, and the indium ϵ_1 values were approximately a factor of four larger than the silver values.

Shown in Fig. 31 is an ERASP result for silver spheroids with laser excitation at 5,145 Å. The semi-major axis dimension was 600 Å, which was a value that could be obtained by oblique angle vacuum deposition on SiO_2 posts. The molecules were assumed to be in a monolayer deposition with a nominal attachment distance of 3 Å. Each curve in Fig. 31 corresponds to a different Raman shift as noted in the figure. Maximum enhancement of approximately 10^6 was achieved with aspect ratios from 2 to 4. For minimum variation of enhancement with Raman shift, an aspect ratio of 3.5 should be selected. Figure 31 also shows that the enhancement has a double peak, and this was because of the double resonance caused by the difference in excitation and Raman wavelengths. Figure 32 shows enhancement predictions for silver spheroids with laser excitation at 4,880 Å. The peak enhancement values were found to be lower than those for 5,145 Å excitation, and the double peaks were almost merged. However, optimum enhancement was still obtained for aspect ratios between 2 and 4. Figure 33 shows enhancement predictions for silver spheroids as a function of laser excitation wavelength. Aspect ratios were varied from 4 to 6 at a constant Raman shift of 2,000 cm^{-1}. Figure 33 reveals that the largest enhancement factors could be obtained by increasing aspect ratio and laser wavelength. The practicality of achieving aspect ratios greater than 6 is questionable, and using wavelengths in the red spectral region reduces the basic Raman scattering cross section as well as increases the probability of laser radiation interfering with sensor testing in the simulated test environment.

Figure 34 displays enhancement predictions for silver hemi-spheroids with laser excitation at 5,145 Å. Again, the semi-major axis was 600 Å, and the molecule attachment distance was 3 Å. The hemi-spheroidal predictions are notably different from the spheroidal model. The enhancement factor curves are more sharply peaked, and the peak enhancement factors ranged from 10^8 to 10^9, which are 2 to 3 orders of magnitude greater than predicted for the spheroidal particles. Furthermore, the optimum range of aspect ratios is from 3 to 5, and the optimum aspect ratio for minimum variation of enhancement with Raman shift is approximately 4. The double resonance phenomenon is readily observed, and the peaks merge for Raman shifts less than 1,000 cm^{-1}. Figure 35 shows enhancement predictions with a laser wavelength of 4,880 Å, and a decrease in enhancement relative to the 5,145 Å values is found. Figure 36 shows enhancement predictions for silver hemi-spheroids as a function of laser wavelength with aspect ratios varied from 1 to 6 and a Raman shift of 2,000 cm^{-1}. Again, there is the obvious trend of obtaining high enhancement factors by using very high aspect ratios and laser excitation in the red spectral region, but, as before, this was not considered practical for AEDC applications.

Figure 37 displays the enhancement predictions for indium spheroids with 5,145 Å laser excitation, semi-major axis of 600 Å, and molecule attachment distance of 3 Å. Obviously, indium would not be a good choice for oblique deposition on SiO_2 posts, because the enhancement factors were found to be approximately 4 orders of magnitude below the

predictions for silver spheroids. However, for indium hemi-spheroids, the enhancement levels were up to the 10^7 range as shown in Fig. 38. Indeed, Fig. 38 has indicated that indium would be an excellent choice for island film type of SERS plates if aspect ratios of 6 to 8 could be obtained. Figure 39 shows that for indium, there is little to be gained by going to very large aspect ratios and long wavelengths.

3.6.5.2 Signal Strength Predictions

To use the ERASP-predicted enhancement factors to calculate SERS signal strengths, consideration was given to the experimental configuration envisioned for using SERS to monitor contamination in the AEDC space chambers. Figure 40 shows a typical excitation/collection optics geometry that would be used for SERS measurements. A laser beam at, for example, 5,145 Å wavelength and power level of approximately 50 mW would be incident on the SERS sample plate. A collection lens would be positioned between the incident and reflected laser beams to collect Raman-scattered radiation from a contaminant cryodeposit on the SERS sample plate. Another lens would be used to image the Raman scattered radiation onto the entrance slit of a triple spectrometer, which would spectrally analyze the signal using a photomultiplier tube as the radiation detector. This type of configuration would be capable of contaminant measurement at only one sample plate location.

For the AEDC space chambers, it would be necessary to make measurements on multiple sample plates simultaneously, and for this reason fiber optics would have to be used to deliver laser radiation to and scattered radiation from the multiple SERS sample plates. It was envisioned that the laser beam would be transmitted with approximately 800-μm-diam fused silica fiber with approximately 200-μm core diameter. Assuming a practical operating length of 30 m for the fibers, a transmission of 88.3 percent was achievable for commercially available fibers. To acquire a Raman spectrum for each SERS sample plate, an intensified, two-dimensional detector array would have to be used instead of a photomultiplier as shown in Fig. 41. At the spectrometer entrance, each sample plate fiber cord would be positioned into a column that would be parallel to and aligned with the entrance slit. The spectral radiation from each fiber cord would be dispersed along rows of the two-dimensional array. As many as ten sample plates could be monitored simultaneously with commercially available detector arrays.

The SERS signal level for the configurations of Figs. 40 and 41 was calculated from the relation

$$S_s = \sigma\, n_s t_s \Omega_c I_O \eta_t\, (EF) \qquad (47)$$

where S_s was the enhanced Raman scattering signal in photoelectrons/sec, σ was the normal Raman scattering cross section in cm^2/sr, n_s was the number density of cryodeposit species in molecules/cm^3, t_s was the cryodeposit thickness in cm, Ω_c was the collection optics solid angle in sr, I_O was the intensity of the laser beam in photons/sec, η_t was the total optical measurement efficiency that included detector quantum efficiency and fiber-optic transmission, and EF was the enhancement factor. It was assumed that the cryodeposit species was CO_2 at 77 K, and the following values were used for the parameters in the signal level equation:

$$\begin{aligned}
\sigma &= 5.68 \times 10^{-31}\ cm^2/sr, \\
n_s &= 2.28 \times 10^{22}\ molecules/cm^3, \\
t_s &= 1\ monolayer,\ = 3.95 \times 10^{-8}\ cm, \\
\Omega_c &= 0.016\ sr, \\
I_O &= 1.29 \times 10^{17}\ photons/sec,\ and \\
\eta_t &= 0.0133.
\end{aligned}$$

The η_t value was estimated by assuming a 90-percent efficiency for all lenses and mirrors, a 50-percent efficiency for all spectrometer gratings, a 20-percent detector quantum efficiency, and an 83.3-percent fiber-optic efficiency. With these assumptions, Eq. (47) was rewritten as

$$S_s = [(1.4 \times 10^{-2})\ (EF)] \tag{48}$$

Based on the ERASP predictions of EF, SERS signal levels ranging from 10^4 to 10^6 photoelectrons/sec could be achieved. These were considered to be very strong signal levels.

3.6.6 Experimental Work

3.6.6.1 Previous Applications of SERS

A review of previous SERS experimental work was performed prior to embarking on AEDC experiments. Most experimental work with SERS has involved studies at electrode-electrolyte interfaces (Refs. 27, 28, and 29, for example). Generally, gold or silver surfaces were prepared in an electrochemical cell. Electrode roughening was achieved using a succession of oxidation-reduction cycles, and immediately following the roughening procedure, the electrode was transferred to another electrochemical cell containing supporting electrolyte and a very small amount of the chemical to be studied. The next most popular technique (Refs. 30, 31, and 32, for example) has been to prepare SERS surfaces by vacuum evaporation of silver or indium onto glass substrates to form island films with thickness of approximately 5 to 50 nm. These films were subsequently coated with monolayers of various chemical species of interest and produced easily detected and processed signals. Other less popular methods for observing SERS have been to use colloidal silver (Refs. 33 and 34, for example) in solvents

containing trace species of interest or to use metal powders (Ref. 35) as the SERS surface.

Some of the work most relevant to AEDC laser microprobe development has been that of Refs. 32, 18, and 24, and Refs. 36, 37, and 38. In Ref. 32 submonolayer sensitivity was achieved with tuned indium and silver island surfaces. To achieve highly reproducible SERS surfaces, photomicrolithography was used to produce an array of SiO_2 posts on a silicon wafer (Ref. 18). Spacing between the posts was 3,200 Å, and each post was 5,000 Å tall with a conical top radius of curvature of 500 Å. By evaporating silver onto this substrate at various grazing angles of incidence, isolated silver particles were obtained at the tops of each post. Microscopic evaluation revealed the silver particles as ellipsoids with a diameter of approximately 100 nm and an aspect ratio as high as 3. Experiments with CN vapor adsorbed on the surface revealed an EF = 10^7. In Refs. 36 and 37, researchers at Oak Ridge National Laboratory (ORNL) developed a method of preparing SERS substrates by coating a filter paper surface with submicron Teflon® or polystyrene latex spheres and then coating the sphere-covered surface with silver. These surfaces were capable of providing SERS signals for detection and identification of monolayers of various organic substances. The same ORNL group also developed SERS plates using substrates consisting of silver particles deposited on stochastically arranged SiO_2 posts produced by plasma etching of a quartz surface using a silver island film as an etch mask (Ref. 21). These surfaces produced excellent SERS spectra with monolayer organic substances. More recently, the same ORNL group has discovered that SERS spectra can be obtained by using cellulosic surfaces covered with silver (Ref. 24). The cellulosic surface consisted of fibers and tendrils intertwined together that provided tips, surface protrusions, and interstices of submicron sizes. When coated with silver, these surfaces had sufficient roughness to produce SERS spectra comparable to those obtained with the stochastic posts. Very recently, the same ORNL group (Ref. 38) developed a SERS fiber-optic sensor based on the concept that was envisioned early in this AEDC project. Indeed, the fiber-optic beam delivery and collection system with 10-m fibers permitted excellent SERS spectra to be obtained from monolayer samples.

3.6.6.2 AEDC Experimental Work

Based on the computational results and the work of others, an experimental system was configured as shown in Fig. 42. Except for the pumping system, all components were mounted on an optical breadboard. The light source was a Coherent Innova 90 argon-ion laser. The laser radiation was directed and focused onto the sample surface by means of mirrors and lenses. The laser off-band plasma light was eliminated by a tunable optical filter. The laser beam was incident on the surface at a nominal angle of 75 deg with respect to the surface normal.

The sample surface was mounted upon the cold finger of a model K2205 MWR Technologies, Inc., cryogenic Joule-Thomson refrigerator. This refrigerator operated by means of a high-pressure (1,200 to 1,800 psi) high-purity (99.999 percent) nitrogen gas expanding through an orifice. A gas filter and flow meter were installed inline. A built-in heater helped stabilize the temperature to as low as 76 K, and cooldown time was about 15 min. A mirror was installed internal to the refrigerator body to reflect the surface-reflected beam back out the input window. The vacuum inside the refrigerator cell could be maintained at approximately 10^{-6} torr with a turbomolecular pump.

Light scattered from the laser beam/sample surface intersection spot was collected by a lens one focal length from the surface. The collected radiation was turned by mirrors and focused onto the entrance slit of a spectrometer. Apertures were in place along the light path to eliminate stray light, and the focusing lens was apertured to match the f-number of the spectrometer.

A Spex Industries, Inc., Model 1877B TRIPLEMATE, 0.6-m triple spectrograph/spectrometer was used for dispersion of the collected scattered radiation. This instrument was designed for extremely high stray-light rejection that was needed for detection of Raman spectra. It also had a wide, flat, unvignetted focal plane for multichannel detectors. The spectrometer had two stages. The first, or filter stage, was a 0.22-m double spectrometer whose gratings were locked in subtractive dispersion, and this stage acted as a bandpass selector and stray light filter. The second stage was a 0.6-m spectrometer that provided spectral dispersion with a selection of any of three turret-mounted gratings.

The detection system consisted of a cooled RCA C31034A photomultiplier tube, an ORTEC photon counting system, and a Clevite Corporation, Brush Mark 250 strip chart recorder.The photomultiplier was cooled to $-70°C$ in a Products for Research dry ice housing, and a frost-free glass envelope was used to prevent condensation on the photomultiplier input surface.

Several types of SERS sample plates were used in the experiments. One type was indium island films prepared at AEDC on thin glass slides. Microscopic examination of these sample plates revealed the metal islands to resemble prolate hemi-spheroids with an aspect ratio of only 1.4. Another set of sample plates was prepared by the Submicron Structures Laboratory of the Massachusetts Institute of Technology. These surfaces were prepared using a microlithography process involving reactive ion etching. This process produced a regular pattern of SiO_2 posts coated with silver on a 3-in.-diam silicon wafer. The spacing between the posts was approximately 2,000 Å, and the post heights were approximately 3,000 Å. The radius of curvature of the post tops was approximately 500 Å, and a 300 Å thickness of Ag was deposited on the sides of the posts. Unfortunately, the aspect ratio of the silver spheroids was not known. Another set of sample plates was provided by ORNL, and these

were 364-nm-diam polystyrene latex spheres coated with silver that had been spin-coated to a monolayer thickness on microscope slides. The aspect ratio of the oblate hemi-spheriods was approximately 0.3.

A pulsed valve was used to deposit small amounts of CO_2 on the various sample plate surfaces that were held at cryogenic temperatures. No SERS spectra of CO_2 were ever obtained. If the CO_2 deposits were thick (i. e., a visible frost on the sample plate surface), then a normal Raman CO_2 spectrum could be obtained. It was first thought that the experimental configuration might be faulty in some manner. Therefore, a sample plate was obtained from ORNL that had been coated with a monolayer of benzoic acid. ORNL also furnished a copy of the SERS spectrum that had been obtained there on the same sample surface. The ORNL sample plate was installed in the scattering cell, and a SERS spectrum was readily obtained with the sample at atmospheric conditions. The AEDC spectrum is compared to the ORNL spectrum in Fig. 43. Although the AEDC spectrum shows a much weaker signal, the spectral features are an excellent match. Consideration was then given to the possibility that the physical nature of the cryodeposit process might hinder the SERS phenomena in some manner. This was removed from consideration with the results of Ref. 39, which showed SERS spectra obtained with deposits at 35 to 40 K temperature.

Resource restrictions unfortunately prevented continued experimentation to understand why no SERS spectra had been obtained. Therefore, the following explanation will be somewhat speculative. A review of the experimental practices of other researchers, including consulting with ORNL, has revealed that most all SERS experiments have been performed within one day after preparation of the sample plate surface. In many cases, the sample plate was prepared in the same vacuum chamber in which the subsequent SERS experiments were performed. At AEDC, a span of several weeks generally existed between sample plate preparation and experiment. Even though the sample plates were contained in protective bags, they were still exposed to air. Furthermore, they were exposed to the laboratory environment for approximately a day during the installation process. The laboratory environment was also at the worst possible cleanliness conditions during the experimental periods because of heavy construction work within the building containing the laboratory. An additional clue is given by the work reported in Ref. 40. In these experiments the sample surface was prepared in vacuum and transferred at atmospheric conditions to another vacuum chamber that was pumped to 10^{-8} torr. Then the surface was cleaned with a UV laser beam for 1 hr to remove nonvolatile residue before successful measurements could be made. It is tentatively concluded that the AEDC experiments did not yield SERS spectra because the sample plates were so badly contaminated that the SERS mechanism could not work. For the sample plates prepared by MIT, there is the additional possibility that an adequately high aspect ratio was not achieved.

The overwhelming positive results of other researchers, the computational results of AEDC, and the development of the fiber-optic SERS sensor by ORNL still indicate that SERS can be used for contamination detection and identification.

3.7 BRDF FOR OPTICAL SURFACE CONTAMINATION DETECTION

The work described in this section was dedicated to the development of an optical contamination monitor based on the measurement of the bidirectional reflectance distribution function (BRDF). A review of the standards and requirements for particulate contamination of future spacecraft and of the AEDC space chambers area particulate measurement/control practices has shown that improvements are required for particulate contamination monitoring. The use of BRDF as a particulate monitor was reviewed, a concept for a prototype instrument was developed, a computer code to aid in instrument design and data reduction was developed, and laboratory particulate contamination data were taken with a laboratory BRDF system.

3.7.1 Review of Particulate Contamination of Optical Components

3.7.1.1 Cleanliness Standards and Their Interrelationships

To build an optical surface particulate contamination monitor, it was necessary to understand the various cleanliness standards that are followed. Federal Standard 209B (Ref. 41) defines air cleanliness classes (ACC) in terms of the maximum number of particles per cubic foot with diameters of 0.5 μm or larger. Only three ACC are specifically defined as follows:

Class 100 (i.e., ACC = 100) in which a cubic foot of air must have no more than 100 particles measuring 0.5-μm diam or larger;

Class 1,000 (i.e., ACC = 1,000) in which a cubic foot of air must have no more than 1,000 particles measuring 0.5-μm diam or larger; and

Class 100,000 (i. e., ACC-100,000) in which a cubic foot of air must have no more than 100,000 particles measuring 0.5-μm diam or larger.

The ACC are shown in Fig. 44. Other classes may be defined by a line intercepting the particle size = 0.5-μm line at a value equal to the ACC and parallel to the three established curves (e.g., class 10,000 in Fig. 44). It should be noted that the three ACC lines are not themselves parallel, because close examination will show that the Class 1,000 line passes through 63 at 5.0 μm, whereas the Class 100,000 line passes through 700 at 5.0 μm. However, the small resulting error is usually neglected, and the lines are considered parallel.

There are several techniques currently available for determining the ACC of a given air space. Generally, there are those techniques that use light scattering detection and those that draw an air sample through a filter and weigh or count the particles collected. The light scattering techniques are useful for continuously monitoring particles with diameters greater than 0.5 μm in still air, but if there is significant air flow (for example, as in a laminar flow cleanroom), it is difficult to obtain an accurate sample. The techniques that draw air samples through a filter are usually restricted to particle sizes greater than 5.0-μm diam. If microscopic techniques are used to count the particles, then the method is not an online technique, and it is restricted to ACC > 10,000 to collect statistically valid samples. If the particle-filled filter is directly weighed by, for example, the patented Tapered Element Oscillating Microbalance (TEOM), an online technique is possible under both atmospheric and high-vacuum conditions (Ref. 42). In addition, the TEOM can provide particle mass measurement down to approximately ACC = 10, but the system will overload with an ACC = 10,000 or greater. The major disadvantages of the TEOM are the 5.0-μm particle diameter lower limit and the requirement of converting a particle mass measurement into the number of particles per cubic foot with diameters greater than 5.0 μm.

Military Standard 1246A (Ref. 43) defines surface cleanliness levels (CL) in terms of particulates per unit area (n) with diameters greater than a given size, and Fig. 45 is a plot of n as a function of particle diameter with CL as a parameter. MIL-STD-1246A assumes a log-normal distribution of particle sizes, i.e.,

$$N\,(r_d)^a = 1 \tag{49}$$

where N is defined as the number of particles per unit volume with diameter "r_d" and with "a" as a constant. Equation (49) can be rewritten as

$$\log N = -a\,(\log r_d) \tag{50}$$

The value of n can be found by the integration

$$\log n = \int_{r_d = r_O}^{r_d} \log N\,(\log r_d) = -(a/2)\,(\log r_d)^2 + C_1 \tag{51}$$

where r_0 is defined as the particle diameter for which there are n with diameters greater than r_0 and C_1 is a constant of integration. With the value of a = 1.8520 (Ref. 43),

$$\log n = 0.9260\,[\log r_O]^2 - 0.9260\,[\log r_d]^2 \tag{52}$$

For MIL-STD-1246A, there is no more than one particle per square foot with diameter greater than r_0, and the CL value is used to represent this diameter, i.e., CL = r_0. Therefore, the size distribution function for MIL-STD-1246A that is shown in Fig. 45 is given by

$$\log n = 0.9260 [\log CL]^2 - 0.9260 [\log r_d]^2 \quad (53)$$

The data or reasoning for using this particle size distribution function are not known, but it is known that in normal cleanrooms (horizontal sampling), there is a disproportionately high level of large particles (Ref. 44). This means that the slope factor (0.9260) in Eq. (53) is too large. However, the size distribution of Eq. (53) is similar to those found on vertical sample plates in cleanrooms (Ref. 45).

The usual methods for measuring the CL of surfaces include the direct microscopic examination of witness plates, flushing a witness plate surface with a solvent, and using either laser scattering techniques to measure the particulate content or filter out the solvent and microscopically count the particles, or collection of particles on sample plates with imprinted grids with subsequent microscopic examination. None of these methods are very satisfactory because of their inability to provide online measurements and their labor intensiveness. There is one other method that involves a combination of air cleanliness monitoring and analysis based on empirical results of particle fallout experiments.

An extensive study of cleanroom particles fallout was performed in Refs. 45 and 46, and an empirical model was developed that expresses fallout as a function of air cleanliness class. This model is shown graphically in Fig. 46, and the relation that represents the mean curve of Fig. 46 is

$$n_d = (2.851 \times 10^3) (NC^{0.773}) \quad (54)$$

where NC is defined as the number of particles per cubic foot with diameters greater than 5.0 μm, and n_d is defined as the number of settled particles per square foot accumlated in a 24-hr period. The relation to ACC is established by

$$NC = (0.0063) ACC \quad (55)$$

which is obtained using the ACC = 10,000 curve.

The orders-of-magnitude variation of particle fallout data with parameters such as cleanroom air change rate and laminar flow velocities as represented by the confidence limit curves in Fig. 46 means that subjective variations in the use of Eq. (54) are required.

This empirical model has been improved (Ref. 47) to give a surface cleanliness level (SCL) as an analytical function of time,

$$SCL(t) = 10^{z(t)} \tag{56}$$

where SCL is defined as the number of particles per square foot of surface with diameters greater than 5.0 μm and t is time in days.

The relation for z(t) is obtained from the CL definition of MIL-STD-1246A and is

$$z(t) = \log SCl(t) = [1.08 \log n_d t + (\log 5.0)^2]^{1/2} \tag{57}$$

Using Eq. 54,

$$z(t) = \{1.08(\log 2.851 \times 10^3 + 0.773 \log NC + \log t) + (\log 5.0)^2]^{1/2} \tag{58}$$

Therefore, with a measurement of ACC and using Eqs. (55), (56), and (58), the cleanliness level of a surface can be obtained. Unfortunately, the difficulty in obtaining timely and accurate ACC measurements and the wide range of curves for particle fallout predictions (previously discussed) makes this a less than satisfactory method.

3.7.1.2 Future Particulate Contamination Requirements for Surveillance Satellites and Ground Test Facilities

A good approximation for future particulate contamination requirements for spacecraft can be obtained by reviewing the published requirements for SSTS (Space Surveillance and Tracking System, Ref. 48), NASA's Hubble Space Telescope (Refs. 49 through 53), Space Station (Ref. 54), UARS (Upper Atmospheric Research Satellite, Ref. 55), and NOAA's EOS (Earth Observing System, Ref. 56). In general, CL values of 100 to 500 must be maintained on orbit, and these requirements are driven by onboard exotic optical and infrared instrumentation and their mission. Obviously, if flight hardware is to undergo test and evaluation in one of the AEDC space chambers, then a maximum CL value of 100 to 500 must be maintained. Using the relations previously noted in Section 3.5, this can be translated to a required ACC of less than 100, and this is for a 1-day test article preparation/installation time. If flight hardware is not being tested or perhaps just prototype components are involved, then the particle contamination requirements can possibly be relaxed, but it is not clear at this time just how much relaxation would be possible. Whatever the ground test contamination requirements, AEDC will be obligated to provide instrumentation that will verify that those requirements are met, and AEDC analysis will be required to translate the test results to expected performance based on on-orbit contamination levels. If it is assumed that analysis techniques are available that will permit an extrapolation of test data over an order-of-magnitude increase in cleanliness level, then a ground test cleanliness level of 1,000 can be tolerated. Assuming a nominal 14-day test article preparation/installation time, then an ACC

of approximately 20,000 can be tolerated. A 28-day preparation/installation time would mean an ACC of 10,000 would have to be maintained. If the particulate fallout rates are following the maximum curves in Fig. 46, then these calculations of tolerable ACC will be much too high.

Based on future spacecraft requirements and the previous assumptions and calculations, an operating range for CL and ACC can be estimated. The AEDC space chambers will have to be able to maintain and monitor surfaces with cleanliness levels of 10 to 500 and air cleanliness with ACC values from 10 to 20,000.

3.7.2 Review of Particulate Contamination Measurement/Control Practices in the Space Chambers Area

3.7.2.1 Control Measures

The former space chamber 7V was the only AEDC space chamber with extensive particulate contamination control measures. The west end of the 7V Chamber was enclosed by an ACC = 10,000 cleanroom, and the east end of the chamber, including the antechamber, was enclosed by an ACC = 100 cleanroom with horizontal air flow. Operating instructions were provided to establish requirements regarding entry of personnel or material into the cleanroom areas. Because the test article was installed into the antechamber while within the ACC = 100 cleanroom and the antechamber remained isolated from the main portion of the chamber during pumpdown, the test chamber itself could be considered to be a class 100 cleanroom. At present, the 7V Chamber is being restructured into the LETS (LWIR Environment and Threat Simulator) Facility in support of sensor development for the USASDC. A similar arrangement of cleanroom facilities is planned for the LETS Facility as for the 7V Chamber.

The Mark I Chamber has a cleanroom area that consists of three rooms: an anteroom, an airlock, and an ACC = 1,000 cleanroom with vertical laminar air flow. This permits preparation of the test article in a relatively clean environment, but installation of the test article requires exposure to the cleanliness conditions of the Mark I Chamber itself. Extreme cleaning measures on the Mark I have shown that it can be reduced to the ACC = 10,000 level. None of the other AEDC space chambers have any sort of particulate control measures.

3.7.2.2 Measurement Systems

There is one airborne particulate counting instrument that can be used in either of the LETS or Mark I cleanrooms. This is a Climet Model CI-226M instrument, which uses a forward light scattering technique for continuous determination of the number of particulates per cubic foot with diameters greater than a selectable value from 0.3 to 20 μm. The upper sampling limit is 2×10^6 particles per cubic foot, and the lower range is limited by the

integration time needed to accumulate a statistically valid sample. Air to be sampled is drawn into the sensor at a rate of 1.0 ft^3/min. For an ACC = 100 air sample, it would take approximately 100 min to obtain a particulate count with a 1-percent precision. The sensor itself is normally located outside of the test area, and the air to be sampled is drawn through a long tube to the sensor. This type of sampling is not conducive to high accuracy, especially if the sampled air is flowing.

3.7.3 Developments Required in Particulate Contamination Monitoring

AEDC measurement systems for both surface and air cleanliness are inadequate for the following reasons:

1. Not enough air cleanliness monitors are available.

2. The air sampling method is susceptible to errors caused by air flow.

3. Surface cleanliness can only be determined by empirical relations using air cleanliness values or by microscopic examination of witness plates.

The deficiencies noted in 1 and 2 can be eliminated with material dollar expenditures and the proper application of isokinetic sampling probes, repectively. Development of real-time surface cleanliness monitoring capability requires significant technological work.

As early as 1979, researchers at Westinghouse (Ref. 57) realized that BRDF measurement could be used to monitor contamination levels in cleanrooms and vacuum chambers. They noted that BRDF measurement had the advantage over other contamination measuring techniques such as QCM and particle counters, because BRDF data could be used to calculate how much the contamination would affect optical system performance. Hughes Aircraft Co. (HAC) has worked on methods to monitor the cleanliness level of optical surfaces on spacecraft (Ref. 58). The Hughes analysis concluded that photographic/microscopic methods could give good, consistent results but not in real time, that surface flushing and liquid particle counting methods were not sensitive enough to particles with diameters less than 25 μm, that the use of particle counting and fallout relations was inaccurate, and that the monitoring of the surface particle light scattering was the only effective method. Aerojet ElectroSystems also realized the effectiveness of using surface particle light scattering as a method of monitoring particulate contamination levels, and developed computational (Ref. 59) and experimental (Ref. 60) capability in that area. NASA Goddard Space Flight Center (GSFC) has shown the correlation of surface cleanliness levels with measurements of surface BRDF (Ref. 61), and the University of Arizona Optical Sciences Center (OSC) developed a concept for a small, portable scatterometer (called the MICROSCAT), which is based on measurement of surface BRDF

(Ref. 62). Recently, researchers at Lockheed Missiles and Space Company (LMSC) developed an improved computational approach for BRDF predictions for use in particulate contamination monitoring (Ref. 63). All of this work has been a strong indication that for AEDC to improve its surface cleanliness monitoring capability, a technique based on measurement of BRDF should be considered.

The basic requirements for a BRDF-based surface cleanliness level monitor for use in the AEDC space chambers area have been developed and are as follows:

1. small size (i.e., 1 to 2 ft^3);
2. portable (i.e. weigh less than 50 lb);
3. capable of operation in cleanrooms and cryovacuum chambers;
4. remotely controllable;
5. computer compatible;
6. capable of operation to at least CL = 25;
7. continuous output;
8. provide information on particle size distribution function as well as CL values based on MIL-STD-1246A; and
9. operate in a wavelength range and in such a manner that it cannot interfere with the handling, installation, and testing of the surface that is being monitored.

The approach to development of a BRDF-based particulate monitoring instrument for AEDC applications was based on concurrent experimental and computational work. The experimental work was to consist of developing and validating a prototype instrument, and the computational work was to consist of developing a code to permit reduction of BRDF data to useful particulate contamination information.

3.7.4 The Use of BRDF for Particulate Contamination Monitoring

3.7.4.1 Description of BRDF

The BRDF of a surface is defined in Ref. 64 as the spatial distribution of the ratio of the reflected radiance to incident irradiance as follows:

$$\text{BRDF}\ (\Theta_i, \phi_i; \Theta_s, \phi_s) = dL\ (\Theta_s, \phi_i; \Theta_s, \phi_s; E_i)/dE\ (\Theta_i, \phi_i) \tag{59}$$

in units of sr^{-1} and where L is the reflected radiance in $W/m^2/sr$, and E is the incident irradiance in W/m^2. The subscripts i and s represent incident and scattered, respectively. The coordinate geometry is shown in Fig. 47. Equation (59) can be rewritten as

$$\text{BRDF}\ (\Theta_i, \phi_i; \Theta_s, \phi_s) = dL\ (\Theta_i, \phi_i; \Theta_s, \phi_s; E_i)/L_i\ (\Theta_i, \phi_i)d\Omega \tag{60}$$

where Ω is the solid angle subtended by the detector apparatus. A number of simplifying assumptions and approximations can be made that are relevant to the development of a practical BRDF instrument for monitoring particulate contamination.

1. The illuminated scattering area, A_s, is small compared to the distance to the detector.

2. The detector dimensions are small compared to the distance to the scattering plane.

3. The incident and scattered radiations are in the same plane.

4. The incident radiation is uniform over the scattering area.

5. The incident radiation is normal to the scattering surface.

6. The scattering surface is isotropic and plane.

Based on these assumptions and approximations, Eq. (60) can be rewritten as

$$\text{BRDF}\ (\Theta_s) = P_s/P_i\ \Omega\cos\Theta_s \tag{61}$$

where P_s and P_i are scattered and incident power, respectively. It can be seen from Eq. (61) that BRDF is measured as a function of solid angle and is independent of the distance between the sample surface and the detector. Because of this independence, the BRDF measurement

can be a standard for cleaniness level monitoring. If a photodetector is used to detect the scattered radiation, the detector output can be described by

$$i_s = \text{BRDF}\ (\Theta_s)\ R\ P_i\ A_{di}\ \cos\Theta_s/R_{ds}^2 \tag{62}$$

in units of amperes (A) where R is the responsivity of the detector in amps/W (A/W), A_{di} is the area of the detector illuminated in cm^2, and R_{ds} is the detector-to-scattering surface distance in cm. To determine BRDF (Θ_s) from the detector output, it is a common practice to use a reference scattering surface of known BRDF. Assuming that the reference surface can be placed into the identical position of the sample surface, the reference signal is

$$i_r = \text{BRDF}_r\ (\Theta_s)\ R\ P_{ir} A_{dl}\ \cos\Theta_s/R_{ds}^2 \tag{63}$$

Therefore, the BRDF of the surface of interest is given by

$$\text{BRDF}\ (\Theta_s) = \text{BRDF}_r\ (\Theta_s)\ \left(i_s/i_r\right)\ \left(P_{ir}/P_i\right) \tag{64}$$

The concept of the noise equivalent BRDF (or NEBRDF) is of importance in designing a BRDF-based instrument. The NEBRDF is defined as that value of BRDF that can be measured with a signal-to-noise ratio (SNR) equal to unity. For a photodetector the noise equivalent power (NEP) is defined as the incident radiant signal power that will yield an electrical current with SNR = 1. The mathematical relation is

$$\text{NEP} = i_n/R, \tag{65}$$

where i_n is the noise current with units of $A/(Hz)^{1/2}$, and R is the responsivity with units of A/W. Using Eq. (65), the NEBRDF relation can be written as

$$\text{NEBRDF}\ (\Theta) = (\text{NEP})\ (B)^{1/2}/\left(P_i(A_{di}/R_{ds}^2)\ \cos\Theta\right) \tag{66}$$

where B is the noise bandwidth in units of Hz, A_{di} is the area of the detector illuminated, and R_{ds} is the distance from the sample surface to the detector. Equation (65) can be rewritten using the relationship between NEP and the normalized detectivity, D^*,

$$D^* = (A_d)^{1/2}/\text{NEP} \tag{67}$$

where A_d is the total detector area in units of cm^2. Therefore,

$$\text{NEBRDF}\ (\Theta) = (R_{ds})^2\ \left(A_d B\right)^{1/2}/D^* P_i A_{di}\ \cos\ \Theta \tag{68}$$

If the following easily achievable values are assumed,

$A_d = A_{di} = 0.05\ cm^2$,
$\Theta = 60$ deg,
$B = 100$ Hz,
$P_i = 30$ mW,
$D^* = 10^{13}$ cm-Hz/W,

then an NEBRDF = 1.2×10^{-7}/sr can be achieved.

3.7.4.2 Review of Young's BRDF Work at AEDC

The pioneering work of Young (Ref. 65) at AEDC demonstrated dramatically the effect of particulate contamination on mirror BRDF. A low-scatter mirror was contaminated with spherical, silver particles with nominal diameters between 9 and 18 μm or between 18 and 36 μm, and the BRDF was measured at wavelengths of 632.8 and 10,600 nm and angles of 1 to 70 deg. The low-scatter test mirrors were fabricated from an aluminum substrate with an electrodeless nickel surface that was "super" polished to obtain an extremely low BRDF that could be neglected in comparison to the BRDF of the particulate contamination. Reasonable agreement between the experimental measurements and the predictions of a computer model developed by Young based on Mie scattering theory (Refs. 66 and 67) was obtained. This model assumed that the only effect of the mirror was to reflect forward scattering from a particle. The particle size distribution function (PSDF) used in the silver particle experiments and calculations was determined by microscopic analysis of glass slides contaminated in the same manner as the test mirror surface.

Low-scatter mirrors were also allowed to become contaminated with particulate fallout from the laboratory air. The mirrors were positioned horizontally, and personnel access was not permitted during 95 hr of exposure. The particle size distribution was determined through microscopic inspection, and the distribution was similar to the MIL-STD-1246A distribution except for a high number of large particles. The particles were assumed to have indices of refraction of $1.5 + i1.0 \times 10^{-6}$ and $0.8 + i5.0 \times 10^{-3}$ for wavelengths of 632.8 and 10,600 nm, resectively. Young's model gave fairly good agreement with the measured BRDF. Subsequently, the MIL-STD-1246A particle size distribution function was used in the model to demonstrate the correlation of BRDF with CL values.

3.7.4.3 Review of Westinghouse Electric BRDF Work

Williams and Lockie (Ref. 57) extended Young's work to a variety of low-scatter surfaces contaminated with dust, hydrocarbon oil, acrylic, and peelable coating residue. BRDF

measurements were shown to be a very practical and accurate method of measuring the scatter degradation of optical surfaces that had become contaminated. This work was the first to note that BRDF measurement could possibly be used for particulate contamination monitoring. Unfortunately, an extension of the computational developments of Young was not pursued.

3.7.4.4 Review of NASA Goddard BRDF Work

In more recent work (Ref. 61), NASA GSFC personnel again demonstrated the strong correlation between BRDF and surface CL values. A 35-mW He-Ne laser was used as a light source, and BRDF was measured from 5 to 40 deg. A schematic of the optical system is shown in Fig. 48. The sample surfaces were exposed to a normal laboratory environment for varying lengths of time, and the cleanliness level of the surfaces was determined by microscopic particle counting techniques using the ASTM F24 method (Ref. 68). The sample surfaces were not extremely low-scatter mirrors as were used by Young and the Westinghouse researchers. Instead, thoroughly clean, commercially available glass microscope slides were used, and it was claimed that the CL value of a cleaned microscope slide surface was 25. It was also noted that improved cleaning procedures could reduce the baseline surface CL value, and this would be important in developing an instrument with a low NEBRDF. The NASA GSFC detection system had a dynamic range of 10^7, and this permitted BRDF measurement down to 10^{-5}/sr. Again, no attempt was made to extend the modeling work of Young.

3.7.4.5 Review of the University of Arizona BRDF Work

The University of Arizona OSC has developed a surface cleanliness level instrument for cleanroom applications (Ref. 62). This microscatterometer was named the MICROSCAT, and a sketch is shown in Fig. 49. The system uses a laser diode operating with 50-mW output at 790 to 840 nm as the radiation source, and photodiodes are used to measure reflected radiation at four angles. The size of the system was conceived as a "little bigger than a breadbox" with a nominal sample surface-to-detector distance of 15 cm. The estimated NEBRDF for this system was approximately 5×10^{-7}/sr, which is nearly two orders of magnitude better than the NASA GSFC system. The OSC has done extensive work in the area of BRDF modeling, and this will be reviewed later in this report.

3.7.4.6 Initial Concept for AEDC BRDF Particulate Contamination Instrument

Based on the experimental work reviewed and the requirements for an AEDC instrument, an initial concept for the AEDC BRDF particulate contamination instrument was developed. A schematic of this concept is shown in Fig. 50. This system would be designed to operate in either a cleanroom environment or a cryovacuum environment; therefore, the optical system

would have to be placed in an environmentally controlled enclosure. This enclosure was conceived to be approximately the size of a "breadbox" similar to the OSC device. The radiation source was to be a laser of 20 to 100 mW output in the visible to near-IR spectral region, and laser power would be continuously monitored. The reference plate would be identical to the sample plate. The reference plate would remain in the enclosure, and the sample plate would remain outside the enclosure until time to monitor its particulate contamination. When a measurement was desired, the enclosure valve would be opened and the sample plate would be translated into the proper position within the enclosure. Reflected radiation would be detected at two different scattering angles. Collection optics would be used to increase the collection solid angle for the photodetectors, and narrow band filters would likely have to be used to limit detected radiation to the laser wavelength. The detector outputs would be processed with a lock-in amplifier, which would require that the laser beam be mechanically chopped. Laser beam expansion would be provided to ensure that the spot size on the plates would be of sufficient size to provide a statistically valid measurement. A specially coated beam splitter plate similar to those used in laser Doppler velocimeter optical systems would be used to split the laser beam into two components that have a normal incidence on the scattering plates. Judicious use of baffle systems would be required to minimize the level of stray light reaching the detectors. Operation of the sample plate translation and valve would be via remote microcomputer operation. All data processing would be done remotely.

It will be seen in later sections of this report that the initial concept for this instrument evolved considerably during the laboratory experimentation process.

3.7.5 Computational Work Required for Development of a BRDF Particulate Monitor

3.7.5.1 Computational Needs and Objectives

It was imperative to be able to physically and quantitatively explain the measured correlations between BRDF and cleanliness level standards. Furthermore, through development of a physically realistic model, a BRDF system can be performance-optimized for the many parameters of influence such as laser wavelength, scattering angles, CL range, PSDF, particulate shape, and particulate refractive index. In addition, the model must be used to reduce measured BRDF to an appropriate surface cleanliness level and for calculation of a realistic PSDF that will be useful for analysis of the effects of particulate contamination on sensitive optical components undergoing test and evaluation in AEDC space chambers. There is also an inverse application of the model, and this involves calculating the BRDF of various contaminated optical surfaces when cleanliness levels have been determined by standard microscopic inspection methods.

The objectives of the AEDC work to develop a computer model of the particulate contamination contribution to the BRDF of an optical surface were to

1. carefully review prior analytical work and build upon it;

2. develop a computer code that was as simple as possible yet realistically models the phenomena of interest;

3. make the code operational on the Space Systems Branch Analysis Work Center network;

4. use the code to make comparisons to the work of Young, Westinghouse, and NASA GSFC;

5. refine the code as required based on the previous comparisons; and

6. use the code to aid in the design and validation of a prototype particulate contamination monitoring instrument.

3.7.5.2 Review of Prior Analytical Work

The prior work of Young (Ref. 65) at AEDC has been discussed in Section 3.7.4.2, but the analytical aspects need to be reviewed briefly. Young's model was based on Mie scattering theory, and a computer code developed by Mundy (Ref. 65) was used. Young's model can be referred to as an unobstructed reflection model because it assumes that the scattering from the particles is unaffected by the surface, that the surface only serves to reflect forward particle scattering, that the reflected scattering is not affected by the presence of the particle, and that there is no interaction of the scattered electromagnetic fields.This model is rather simplistic, but it has had great success in its agreement with BRDF measurements of known particulate loading of optical surfaces.

The work of Scheer (Ref. 59) addressed the effects of condensible molecular contamination on space-borne optics. Scattering by the molecular contamination was modeled by assuming that the molecules had coalesced into an equivalent mass of spherical particles. Mie scattering was used to model the particle scattering, and Scherr's computer code was based on Program A in Ref. 69. Scherr's model, like Young's, assumes that the light scattered from the particles is reflected from the optical surface and is unaffected by the existence of the particles.

The work of Nahm (Ref. 70) addressed light scattering from a sphere in contact with a mirror surface. Again, the light scattering from the spherical particle was calculated by

Mie theory and used Program A from Ref. 69, and no further interaction of the scattered fields was assumed. However, interaction of the scattered fields was permitted, and several models of this interaction were studied. It was concluded that the sphere on a mirror could best be modeled by replacing the surface plane with an imaginary sphere as in classical electrodynamics. That is, the surface plane is replaced with an image sphere at the same distance from the plane as the actual particle. The two spheres are treated as two coherent scatterers, and light scattered from the image sphere is given a phase shift of π to account for the actual reflection from the surface. The resultant scattered field is the linear sum of the two fields. There is an additional phase shift between the two fields corresponding to the difference in optical paths. This model was termed the phase difference model, and it was shown to give marginally better agreement with experimental data than Young's model.

The work of Ma and Associates (Ref. 63) at LSMC has extended the work of Young by including surface obscuration effects, nonspherical particulate effects, and diffraction and reflection contributions to BRDF. The basic assumption of Young with regard to the lack of interaction between particle and surface was used, and the phase lag or reflection interaction phenomena considered by Nahm was ignored.

3.7.5.3 New AEDC BRDF Model

3.7.5.3.1 Assumptions and Approximations

Based on the computational objectives noted in Section 3.7.5.1, it was desirable to use the same computer code as Young with improvements based on Ma's model. Unfortunately, Young's computer code could not be found; therefore, the easiest path to follow was to make an adaptation from the code of Scherr. Scheer's code was modified to enable the calculation of the BRDF for a distribution of particles at user-specified angles. The PSDF to be used in the calculation can be the MIL-STD-1246A distribution, a single or bimodal function composed of log-normal distributions, or an empirical distribution based on experimental measurements. In addition to the assumptions already discussed for Young's model, it was also assumed that a single refractive index applied to all scattering particles, that the particle size distribution function was known, that the particles were spherical, and that the uncontaminated surface BRDF was known or negligible.

The output from the first modification to Scheer's code was compared to the original calculations of Young, and the agreement was excellent. The code was then modified to account for particulate diffraction, reflection, and obscuration effects. It was assumed that all contributions to BRDF could be summed to yield the total BRDF.

3.7.5.3.2 Mathematical Relations

Total BRDF was calculated as

$$\begin{aligned} BRDF(\Theta_s) = {} & BRDF_{bl}(\Theta_s) + BRDF^{f}_{mie}(\Theta_s) + BRDF^{b}_{mie}(\Theta_s) \\ & + BRDF_{d}(\theta_s) + BRDF_{r}(\Theta_s) \end{aligned} \tag{69}$$

$BRDF_{bl}(\Theta_s)$ is defined as the baseline BRDF of the clean sample surface and is approximated by

$$BRDF_{bl}(\Theta_s) = C1\left(\Theta_s^{-C2}\right) \tag{70}$$

where C1 and C2 are constants. The Mie scattering theory is used to calculate the radiation scattered by the particulate contaminants, and the forward and backward Mie scattering terms are given by $BRDF^{f}_{mie}(\Theta_s)$ and $BRDF^{b}_{mie}(\Theta_s)$, respectively. With reference to Fig. 51, the radiation incident on the sample plate propagates along the Z axis with its electric vector polarized along the X axis. The scattered radiation is observed in the Θ,ϕ direction. This direction and that of the incident radiation constitutes the scattering plane. The intensity of scattered radiation, as presented in Ref. 66, is

$$I_{\phi} = (\lambda^2/4\pi^2r^2)i_1 \sin^2\phi \tag{71}$$

and

$$I_{\theta} = (\lambda^2/4\pi^2r^2)\, i_2\cos^2\phi \tag{72}$$

where i_1 and i_2 are intensity functions. If $\phi = 90$ deg is chosen, then the incident polarization is perpendicular to the scattering plane, and the scattered intensity is

$$I_{\phi} = (\lambda^2/4\pi^2r^2)i_1 \tag{73}$$

If $\phi = 0$ deg is chosen, then the incident polarization is parallel to the scattering plane, and the scattered intensity is

$$I_{\Theta} = (\lambda^2/4\pi^2r^2)i_2 \tag{74}$$

If the incident radiation is nonpolarized, then the scattered intensity is

$$I_{\phi,\Theta} = 0.5\,(\lambda^2/4\pi^2r^2)\,(i_1 + i_2) \tag{75}$$

Because the contaminant particles are assumed to be in free space (i.e., not interacting with the sample plate surface), Eqs. (73), (74), or (75) can be used to obtain the particle scattering in terms of BRDF as defined in Eq. (61).

$$BRDF(\Theta_s) = \lambda^2 D_p i_{mie}/4\pi^2 \cos\Theta_s \tag{76}$$

where D_p is the particle surface density in units of number of particles per cm^2 and i_{mie} is the appropriate Mie scattering intensity function based on the polarization properties of the incident radiation.

The diffraction component of the total BRDF is calculated for particle sizes much larger than the wavelength, i.e.,

$$X_p = \pi r_d/\lambda > 20 \tag{77}$$

For spherical particles,

$$BRDF_d(\Theta_s) = (X_p^2/4\pi)\,(2J_1(X_p \sin\Theta_s)/X_p \sin\Theta_s)^2\, D_p/\cos\Theta_s \tag{78}$$

where J_1 is a first-order Bessel function. Similarly, the reflection component is

$$BRDF_r(\Theta_s) = (8/12\pi)\,(\sin\Theta_s - \Theta_s \cos\Theta_s)\, D_p/\cos\Theta_s \tag{79}$$

Surface obscuration for the MIL-STD-1246A distribution is calculated by an empirical relation for spherical particles from Ref. 63

$$\log(\text{percent obscuration}) = -7.245 + 0.9260\,[\log CL]^2 \tag{80}$$

Therefore, the modification to surface reflectivity caused by obscuration can be calculated by

$$R_{real} = R_{ideal}\left\{1.0 - \left(10^{-9.245 + 0.9260\,[\log CL]^2}\right)\right\} \tag{81}$$

where R_{real} and R_{ideal} are the real and ideal surface reflectivity factors. Both the forward-scatter Mie and diffraction BRDF components are modified by the above relation.

All of the previous relations, as well as previously discussed options for particulate size distribution functions, are part of the AEDC Code PBRDF, which is used to predict the BRDF of a sample surface contaminated with particulates.

3.7.5.3.3 Comparisons to Measurements of Others

Young's BRDF measurements for a mirror contaminated with 9- to 18-μm-diam silver particles are shown in Fig. 52 in comparison to predictions from Code PBRDF. The agreement is excellent. The silver refractive index used was 0.177 + i1.0, and the particle size distribution function was accurately known. Figure 53 compares predictions from Code PBRDF with measurements at NASA GSFC (Ref. 61). A dust particulate refractive index of 1.5 + i1.0 $\times$ 10^{-6} was assumed. These measurements do not agree with the predictions as well as for the case of Young's silver particles. This is believed to be caused by the uncertainty in the basic BRDF measurement as well as in the determination of the cleanliness level of the microscope slides that were used as sample plates. Furthermore, the present Code PBRDF cannot calculate contributions from the bulk scattering within the microscope slides. Figure 54 shows the comparison between the Code PBRDF predictions and the measurements obtained by Westinghouse researchers (Ref. 57). Again, a dust refractive index of 1.5 + i1.0 $\times$ 10^{-6} was assumed. Although the cleanliness levels were not known, the CL = 300 and CL = 500 predictions give good agreement with the two sets of measurements.

3.7.6 AEDC Prototype BRDF Particulate Monitor

3.7.6.1 Apparatus

The prototype BRDF particle monitor experimental setup is shown in Fig. 55. Laser radiation at 6,328 Å was chopped at 100 Hz and passed to the sample surface at normal incidence. Scattered radiation was collected at 5- and 10-deg angles from normal and focused on two photomultipliers. The electrical signals generated by the detectors were fed through preamps to lock-in amplifiers for demodulation. The actual prototype instrument was much simpler than the original concept shown in Fig. 50. A microscope with video camera attachment was used to count particles on the sample surface. All equipment was located in a Class 1,000 cleanroom.

3.7.6.2 AEDC BRDF Measurements

Shown in Fig. 56 is a comparison of the Code PBRDF predictions to measurements of the BRDF of a Pyrex mirror exposed to the environment of the Mark I Chamber cleanroom. The Pyrex mirror is obviously not a low baseline BRDF sample plate, but the particulate contamination data fit well to a CL = 400 prediction. Shown in Fig. 57 is a comparison of Code PBRDF predictions to measurements of the BRDF of a low-scatter mirror used as a sample plate. The sample plate was exposed for different time periods to a normal laboratory environment. Microscopic examination of the surface cleanliness gave 300 < CL < 350. As shown in Fig. 57, Code PBRDF would indicate a CL $\cong$ 200. Considering the great variability in the microscope results for cleanliness level, this should be interpreted as good agreement.

4.0 CONTAMINATION ANALYSIS SUPPORT

In addition to measurement of contamination, the capability to compute outgassing behavior of materials and the subsequent transfer of the contaminant flux to other surfaces and the effect of the contaminant is required. This capability can be used both for pretest analysis of the space chamber contamination environment and posttest analysis of the effects of contamination on data quality.

4.1 MOLECULAR FLOW CODES

Two codes were obtained from the Computer Software Management and Information Center (COSMIC) sponsored by NASA. The Molecular Flow Analyzer (MFA) was developed to simulate molecular flow in the NASA Johnson Space Center thermal vacuum chambers A and B (Ref. 71). The Multispecies Transient Simulator (MTS) was developed to simulate the pressure variation in a vacuum system based on pumping speeds, gas loads, and conductances (Ref. 72). Both codes were made operational on the chamber area analysis computer system.

The MFA code uses variations of the Monte Carlo statistical method to simulate the transfer of flux from chamber leak and other outgas sources to the test article or molecular sensors. Both point and area sources can be simulated. The test article and cryosurfaces are simulated with combinations of subshapes. The basic idea of the Monte Carlo is to follow a group of sample molecules and count the number of molecules that intersect a unit area of surface. When the molecule hits a surface, a test is made to determine if the molecule is captured or continues to bounce. A count is made if the molecule condenses on an area. When all molecules are exhausted, the total counts give the results. A hybrid technique is used in the MFA code. It is assumed that for molecules traveling directly from a source to a point, the flux can be calculated from a simple view factor relationship without need for counting sample molecules. The concept is extended to include scattering from other molecules and from walls by using Monte Carlo principles.

Although the MFA code was developed to simulate NASA-JSC chambers, the geometry inputs are such that the model can be modified to simulate other chambers of similar shape. Work was begun under this project to modify the geometry for AEDC chambers.

The MTS code includes a set of simultaneous differential equations that govern the dynamic response of a system of interconnected compartments containing a number of gas molecule species. When the conditions of the vacuum system are known, the values of compartment

volumes, pumping speed, gas load, and conductance are fed to the model. These values vary with pressure and time in general. The solution of the math model is the response of each species of gas molecule in each compartment at each moment.

The applications of the MTS include

1. simulating pumpdown curves with given vacuum chamber configurations, including various types of pumping capabilities and gas loads;

2. simulating repressurization curves;

3. simulating sudden changes of pressure;

4. simulating contaminant propogation in compartments, and finding leaks and computing conductance between compartments; and

5. finding chamber outgassing times required to reach a specified ultimate pressure.

This analysis can be very important to determine the cooldown sequence during a test to prevent contamination of cryogenic optical components.

The code has been modified to generate plots of partial pressure, gas load, and pumping speed for each species and total pressure as a function of time.

4.2 TRACOR® GC/MS ANALYSIS CAPABILITY

Signal processing programs with the Tracor system provide the following capabilities:

1. monitor or print chromatograms that may represent total ion count, or detected signal for selected masses or mass ranges only;

2. monitor or print spectrum data at selected points in the chromatogram, or averaged over selected time intervals;

3. find a number of compounds in a library best matching a given spectrum; monitor the two best along with the spectrum of interest; print out data including quality of match; and

4. determine quantity of "unknown" based on external or internal standard based on either peak height or area.

Standard libraries included with the system are an environmental library, drug library, and the NIST library. All data obtained from measurements of materials used in the space chambers will be included in an AEDC library.

4.3 CHAMBER MATERIALS DATABASE

The chamber materials database (CMDB) is a database designed for maintaining information about materials commonly used in the aerospace chambers at AEDC. This information primarily covers the contamination-related properties of these materials. The CMDB and its associated software package can be used to store and retrieve such data as may be of interest to chambers-area work. The CMDB is to be used in helping to determine contaminating species that could be expected from a material proposed for use in the aerospace chambers and in helping to determine the identities of the sources of contaminating species found in the chambers. These capabilities will help engineering personnel to minimize contamination in the chambers to better simulate the space environment.

The database was written in VAX Rdb/VMS programming language and is maintained in files that are stored in the AEDC Mark I VAX 8650 computer. A user must run this program and specify the access procedures needed by selecting processing options at each of a series of menus. This tree structure query method sets up the information packet required by the software for performing the storage or retrieval of the needed data. This technique is very flexible and should allow the user to do the large majority of information processing procedures that might be required.

As noted previously, the CMDB should maintain contamination-related information. With this in mind, it was designed to store only certain material properties such as density, melting temperature, vapor pressure, collected volatile condensable materials (CVCM), total mass loss (TML), refractive index, and various types of spectra. A complete description of data structure and query procedure is given in Appendix A.

5.0 CONCLUSIONS

5.1 MATERIAL SCREENING

1. The Outgassing Chamber (OGC) can be used to determine the amount of outgassing that a sample will produce.

2. Mass spectra of the outgassing products from a sample can be obtained and compared to cataloged spectra to aid in species identification. However, fast transients in composition cannot be followed because of noise, which must be integrated out.

3. Thermogravimetric analysis of outgassing products from a sample can be accomplished to help in species identification. However, vapor pressure data for the evolved species must be available. Also, only liquid nitrogen-cooled and ambient temperature QCMs are available.

4. Several samples of materials were processed in the OGC so that records from these materials are available for comparison.

5.2 SAMPLE TRANSFER MECHANISM (STM)

1. The STM can collect a sample that will condense at liquid nitrogen temperature and transport it to the OGC for analysis.

2. Use of the OGC as a material screening chamber in the same timeframe as its use for analyzing samples brought by the STM is not compatible because of cross-contamination problems. Therefore, the OGC must be thoroughly decontaminated prior to use with the STM.

5.3 SURFACE ACOUSTIC WAVE (SAW) MICROBALANCE

1. The SAW microbalance has a potential sensitivity much greater than a QCM.

2. The SAW microbalance has the potential to identify contaminants as well as measuring the amount of contaminant on the surface.

3. The prototype SAW microbalance did operate in a vacuum environment while cooled by liquid nitrogen. However, its sensitivity to temperature change was large, and the lack of stability of its electronics precluded realizing its potential for measuring a small accumulation of mass.

4. The 0.8 condensation coefficient determined from measured mass accumulation on the QCM and calculated flow from the water vapor source is a reasonable, if somewhat low, value. The SAW device was positioned so that it received the same flux as the QCM; therefore, the 0.5 condensation coefficient obtained for the SAW device seems rather low. This difference could be caused by one or more of the following:

   a. an error in geometry determination;

   b. source flux not uniform;

c. the surface temperature may not be uniform at the assumed value;

d. the surface of the SAW crystal is almost 100 percent covered by the metal film interdigital transducer so that the condensation coefficient may actually be somewhat different than the QCM.

5.4 SURFACE-ENHANCED RAMAN SCATTERING (SERS)

1. AEDC computations and the experimental work of others still indicate that SERS can be developed into a technique for contamination detection and identification.

2. Because it is believed that laboratory contamination of the SERS sample plates prevented detection of SERS spectra, it is necessary to modify the initial concept for a SERS-based laser microprobe. Possibilities for a new concept are

   a. SERS sample plates coated within the microprobe system and with provision to be maintained at high vacuum until needed to sample a possibly contaminating environment;

   b. SERS sample plates coated within modules that are sealed at high vacuum and attached to the basic microprobe unit, which is also maintained at high vacuum.

5.5 BRDF PARTICULATE MONITOR

1. It has been demonstrated that measurements of sample plate BRDF combined with code PBRDF predictions can yield a measurement of the cleanliness level value for optical components exposed to the sampled environment.

REFERENCES

1. Wallace, D. A. "Miniature Quartz Crystal Microbalance for Contamination Measurement." *AIAA Journal of Spacecraft*, Vol. 17, No. 2, March-April 1980.

2. Glassford, A. P. M. and Garrett, J. W. "Characterization of Contamination Generation Characteristics of Satellite Materials, Phase II — Test Method Development." AFWAL-TR-85-4118, December 1985.

3. Montgomery, J. W. "Technical Operating Report: SSTS Optics Assessment and Requirements Report, Vol. III — Contamination Predictions and Requirements, Section II — Contamination Requirements." Rockwell International SSD-86-0067-sB, April 1986.

4. Rayleigh, Lord. "On Waves Propagated Along the Plane Surface of an Elastic Solid." *Proceedings of the London Mathematical Society*, 17 (1885), pp. 4-11.

5. Auld, B.A. *Acoustic Fields and Waves in Solids. Vol. II*, John Wiley & Sons, Inc., New York, 1973.

6. Wohltjen, H. "Mechanism of Operation and Design Considerations for Surface Acoustic Wave Device Vapor Sensors." *Sensors and Actuators*, Vol. 5, 1984, pp. 307-325.

7. Condon, E. A. and Odishaw, H. *Handbook of Physics*, McGraw-Hill Book Company, New York, 1967 (2nd Edition).

8. Schulz, M. B., Matsinger, B. J., and Holland, M. G. "Temperature Dependence of Surface Acoustic Wave Velocity on a Quartz." Vol. 41, No. 7, June 1970, pp. 2755-2765.

9. Wohltjen, H., Snow, A. W., and Jarvis, N. L. "Surface Acoustic Wave Devices as Chemical Vapor Microsensors." NRL Memorandum Report No. 5530, April 18, 1985.

10. Wohltjen, H., Snow, A. W., and Ballantine, D. "The Selective Detection of Vapors Using Surface Acoustic Wave Devices." *Proceedings of the International Conference on Solid-State Sensors and Actuators-Transducers '85*, Boston, Massachusetts, June 11-14, 1985.

11. Martin, S. J. et al. *Journal of Applied Physics*, Vol. 54, 1983.

12. Martin, S. J. et al. *1980 Ultrasonics Symposium Proceedings* (IEEE, New York, 1980).

13. Martin, S.J. et al. "Vapor Sensing by Means of a ZnO-on-Si Surface Acoustic Wave Resonator." 1984 Ultrasonic Symposium Proceedings (IEEE, New York, 1984).

14. Dushman, Saul and Lafferty, J. M. *Scientific Foundations of Vacuum Technique*, John Wiley & Sons, Inc., New York, 1962 (2nd Edition).

15. O'Hanlon, J. F. *A User's Guide to Vacuum Technology*, John Wiley & Sons, Inc., New York, 1980.

16. Weaver, D. P. and Lewis, J. W. L. "Raman Scattering Studies of Solid-Phase Species." AEDC-TR-80-4 (AD-A083926), April 1980.

17. Jackson, J. D. *Classical Electrodynamics*, John Wiley & Sons, Inc., New York, 1967.

18. Liao, P. F. "Silver Structures Produced by Microlithography." *Surface Enhanced Raman Scattering*. Edited by R. K. Chang and T. E. Furtak, Plenum Press, New York, 1982.

19. Liao, P. F. and Wokaun, A. "Lightning Rod Effect in Surface Enhanced Raman Scattering." *Journal of Chemical Physics*, Vol. 76, No. 1, Jan. 1, 1982, pp. 751-752.

20. Wokaun, A., Gordon, J. P., and Liao, P. F. "Radiation Damping in Surface Enhanced Raman Scattering." *Physical Review Letters*, Vol. 48, No. 14, April 5, 1982, pp. 957-960.

21. Vo-Dinh, T. "Surface Enhanced Raman Spectrometry with Silver Particles on Stochastic-Post Substrates." *Analytica Chimica Acta*, 181, 1986, pp. 139-148.

22. Gersten, J. I. and Nitzan, A. "Electromagnetic Theory of Enhanced Raman Scattering by Molecules Absorbed at Rough Surfaces." *Journal of Chemical Physics*, Vol. 73, 1980.

23. Aroca, R. and Martin, F. "Tuning Metal Island Films for Maximum Surface Enhanced Raman Scattering." *Journal of Raman Spectroscopy*, Vol. 16, No. 3, 1985, pp. 156-162.

24. Vo-Dinh, T. Uziel, M., and Morrison, A. L. "Surface Enhanced Raman Analysis of Benzo[A]Pyrene-DNA Adducts on Silver-Coated Cellulose Substrates." *Applied Spectroscopy*, Vol. 41, No. 4, 1987, pp. 605-610.

25. Johnson, P. B. and Christy, R. W. "Optical Constants of the Nobel Metals." *Physical Review B*, Vol. 6, No. 12, December 15, 1972, pp. 4370-4379.

26. Theye, M. L. and Devant, G. "Optical Properties of Indium from Thin Film Measurements." *Thin Solid Films*, Vol. 4, 1969, pp. 205-210.

27. Gao, P. and Weaver, M. J. "Surface-Enhanced Raman Spectroscopy as a Probe of Adsorbate-Surface Bonding: Benzene and Monosubstituted Benzenes Adsorbed at Gold Electrodes." *Journal of Physical Chemistry*, Vol. 89, 1985, pp. 5040-5046.

28. Weaver, M. J. et al. "Surface Enhancement Factors for Raman Scattering at Silver Electrodes: Role of Adsorbate-Surface Interactions and Electronic Structure." *Journal of Chemical Physics*, Vol. 82, June 1985, pp. 4867-4874.

29. Otto, C. et al. "Surface-Enhanced Raman Spectroscopy of DNA Bases." *Journal of Raman Spectroscopy*, 1986, pp. 289-298.

30. Aroca, R. and Martin, F. "Trace Analysis of Tetrasulphonated Copper Phthalocyanine by Surface Enhanced Raman Spectroscopy." *Journal of Raman Spectroscopy*, 1986, pp. 243-247.

31. Kobayashi, Y. and Itoh, K. "Surface-Enhanced Resonance Raman Scattering Spectra of Meso-Substituted Prophines in Layered Structures Having CaF2/Porphine/Ag and CaF2/Ag/Porphine Configurations." *Journal of Physical Chemistry*, Vol. 89, 1985, pp. 5174-5178.

32. Aroca, R. et al. "Surface-Enhanced Raman Scattering of Langmuir- Blodgett Monolayers of Phthalocyanine by Indium and Silver Island Films." *Journal of Physical Chemistry*, Vol. 89, 1985, pp 4051-4054.

33. Hildebrandt, P. and Stockburger, M. "Surface-Enhanced Resonance Raman Spectroscopy of Rhodamine 6G Adsorbed on Colloidal Silver." *Journal of Physical Chemistry*, Vol. 88, 1984, pp. 5935-5944.

34. Lepp, A. and Siiman, O. "Surface Resonance Raman and Surface-Enhanced Raman Scattering Excitation Profiles for Dabsyl Aspartate on Colliodal Silver in Ethanol." *Journal of Physical Chemistry*, Vol. 89, 1985, pp. 3444-3502.

35. Dorain, P. B. and Boggio, J. E. "The Reactions of NO2/N2O4 with Ag: A Surface Enhanced Raman Scattering and Ellipsometric Measurement." *Journal of Physical Chemistry*, Vol. 84, January 1986, pp. 135-141.

36. Vo-Dinh, T. et al. "Surface-Enhanced Raman Spectrometry for Trace Organic Analysis." *Analytical Chemistry*, 56, 1984, pp. 1667-1770.

37. Moody, R. L., Vo-Dinh, T., and Fletcher, W. H. "Investigation of Experimental Parameters for Surface-Enhanced Raman Scattering (SERS) Using Silver-Coated Microsphere Substrates." *Applied Spectroscopy*, Vol. 41, No. 6, 1987, pp. 966-970.

38. Bello, J. M. and Vo-Dinh, T. "Surface-Enhanced Raman Scattering Fiber-Optic Sensor." *Applied Spectroscopy*, Vol. 44, No. 1, 1990, pp. 63-69.

39. Blue, D. et al. "Interference Effects in Surface Enhanced Raman Scattering by Thin Adsorbed Layers." *Journal of Chemical Physics*, Vol. 92, No. 7, April 1990, pp.4600-4608.

40. Tsang, T. et al. "Surface-Plasmon-Enhanced Multiphoton Photoelectric Emission from Thin Silver Films." *Optics Letters*, Vol. 15, No. 15, August 1990, pp. 866-868.

41. "Federal Standard Clean Room and Work Station Requirements, Controlled Environment." Fed. Std. No. 209B, General Services Administration, April 24, 1973.

42. Patashnick, H. and Rupprecht, G. "Microweighing Goes On Line in Real Time." *Research and Development*, June 1986, pp. 74-78.

43. "Military Standard Product Cleanliness Levels and Contamination Control Program." MIL-STD-1246A, August 18, 1967.

44. Bareiss, L. E., Payton, R. M., and Papazian, H. A. "Shuttle/Spacelab Contamination Environment and Effects Handbook." NASA Contractor Report 4053, March 1987.

45. Hamberg, O. and Shon, E. M. "Particle Size Distribution on Surfaces in Clean Rooms." Aerospace Corporation, Institute of Environmental Science, 30th Annual Technical Meeting, Orlando, Florida, May 1-3, 1984.

46. Hamberg, O. "Particulate Fallout Predictions for Clean Rooms." *Journal of Environmental Sciences*, Vol. 25, No. 3, May/June 1982.

47. Buch, J. D. "Analysis of Particulate Contamination Buildup on Surfaces." SPIE Conference 777, Optical System Contamination: Effects, Measurement, Control, Orlando, Florida, May 19-22, 1987.

48. Montgomery, J. W. "Technical Operating Report: SSTS Optics Assessment and Requirements Report, Vol. III—Contamination Predictions and Requirements, Section II—Contamination Requirements." Rockwell International SSD-86-0067-3B, April 30, 1986.

49. Tenerelli, D. J. et al. "Hubble Space Telescope Contamination Control Program Plan." SPIE Conference 777, Optical System Contamination: Effects, Measurement, Control, Orlando, Florida, May 19-22, 1987.

50. Facey, T. A. "Particulate Contamination Control in the Optical Telescope Assembly for the Hubble Space Telescope." SPIE Conference 777, Optical System Contamination: Effects, Measurement, Control, Orlando, Florida, May 19-22, 1987.

51. Burdick, L. A., Jr., Hultquist, A.E., and Mason, K. "Clean Room for Hubble Space Telescope." SPIE Conference 777, Optical System Contamination: Effects, Measurement, Control, Orlando, Florida, May 19-22, 1987.

52. Fong, M. C., Peterson, M. A., and Lee, A. L. "Hubble Space Telescope Contamination Analysis." SPIE Conference 777, Optical System Contamination: Effects, Measurement, Control, Orlando, Florida, May 19-22, 1987.

53. Steakley, J. M. et. al. "Definition and Implementation of a Thermal Vacuum Bakeout Program for the Hubble Space Telescope." SPIE Conference 777, Optical System Contamination: Effects, Measurement, Control, Orlando, Florida, May 19-22, 1987.

54. Carosso, N. J. P. "Space Station Users Contamination Requirements." SPIE Conference 777, Optical System Contamination: Effects, Measurement, Control, Orlando, Florida, May 19-22, 1987.

55. Carosso, P. A. "Upper Atmosphere Research Satellite (UARS) Contamination Control." SPIE Conference 777, Optical System Contamination: Effects, Measurement, Control, Orlando, Florida, May 19-22, 1987.

56. Millard J. M. and Hansen, P. A. "Earth Observing System (EOS)/NOAA Candidate Propulsion System Assessment and Instrument Contamination Requirements." SPIE Conference 777, Optical System Contamination: Effects, Measurement, Control, Orlando, Florida, May 19-22, 1987.

57. Williams, V. L. and Lockie, R. T. "Optical Contamination Assessment by Bidirectional Reflectance Distribution Function (BRDF) Measurement." *Optical Engineering*, Vol. 18, No. 2, March-April 1979, pp. 152-156.

58. Beck, D. G. "CONIN Contamination Investigation Contract Review." RADC Contamination Contracts Review Conference, Griffiss AFB, New York, April 15, 1987.

59. Scheer, L. M. and Lee, W. W. "Assessment of Condensible Molecular and Particulate Contamination on Optical Elements in Space Systems." SPIE Conference 777, Optical System Contamination: Effects, Measurement, Control, Orlando, Florida, May 19-22, 1987.

60. Mossman, D. and George, P. "Optics Survivability." RADC Contamination Contracts Review Conference, Griffiss AFB, New York, April 16, 1987.

61. Carosso, P. A. and Carosso, N. J. P. "Role of Scattering Distribution Functions in Spacecraft Contamination Control Practices." *Applied Optics*, Vol. 25, No. 7, April 1, 1987, pp. 1230-1234.

62. Wolfe, W. "Particulate Contamination Assessment — Practical Formula Cleanroom Monitor." RADC Contamination Contracts Review Conference, Griffiss AFB, New York, April 17, 1987.

63. Ma, P., Fong, M., and Lee, A. "Surface Particle Obscuration and BRDF Predictions." SPIE 33rd International Symposium on Optical and Optoelectronic Applied Science and Engineering, August 10, 1989, San Diego, California.

64. Nicodemus, F. E. "Directional Reflectance and Emissivity of an Opaque Surface." *Applied Optics*, Vol. 4, 1965.

65. Young, R. P. "Low-Scatter Mirror Degradation by Particle Contamination." *Optical Engineering*, Vol. 15, No. 6, Nov./Dec., pp. 516-520.

66. Kerker, M. *The Scattering of Light and Other Electromagnetic Radiation*. Academic Press, New York, 1969.

67. Mundy, W. C., Roux, J. A. and Smith, A. M. "Mie Scattering by Spheres in an Absorbing Medium." *Journal of the Optical Society of America*, Vol. 64, No. 12, December 1974.

68. "Standard Method for Measuring and Counting Particulate Contamination on Surfaces." ASTM-F24-65, Reapproved 1983.

69. Bohren, C. F. and Huffman, D. R. *Absorption and Scattering of Light by Small Particles*. Wiley-Interscience, 1983.

70. Nahm, K. B. and Wolfe, W. L. "Light-Scattering Models for Spheres on a Conducting Plane: Comparison with Experiment." *Applied Optics*, Vol. 26, No. 15, Aug. 1, 1987, pp. 2995-2999.

71. Lee, A. L. and Robertson, S. I. "The Molecular Flow Analyzer and Its Application to Thermal-Vacuum Simulation Chambers." LMSC-HREC, TR D390712, March 1975.

72. Lee, A. L. "Multi-Species Transient Simulator and Its Application to Thermal-Vacuum Chambers." LMSC-HREC, TR D390714, March 1975.

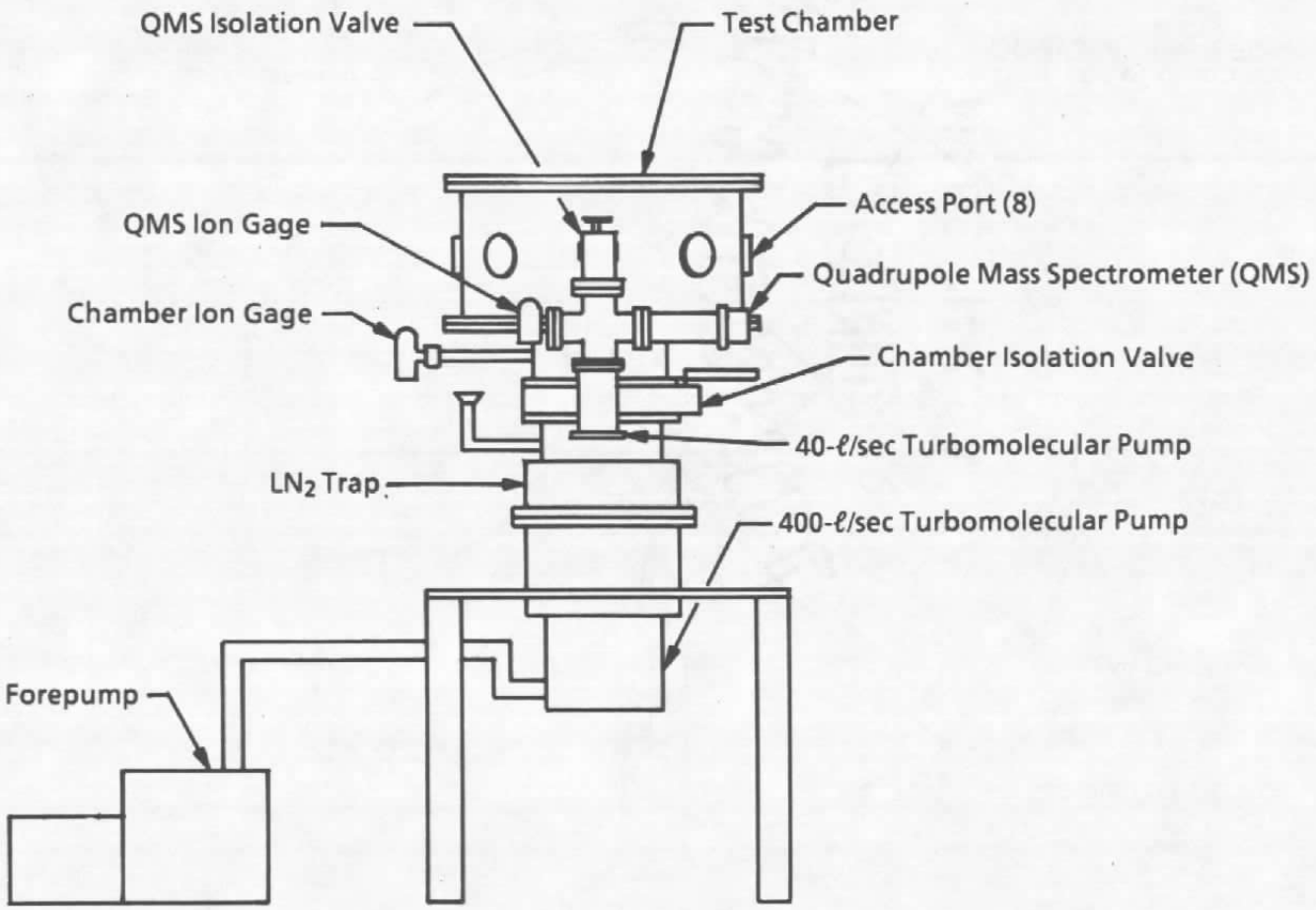

Figure 1. Outgassing chamber (OGC) configuration, side view.

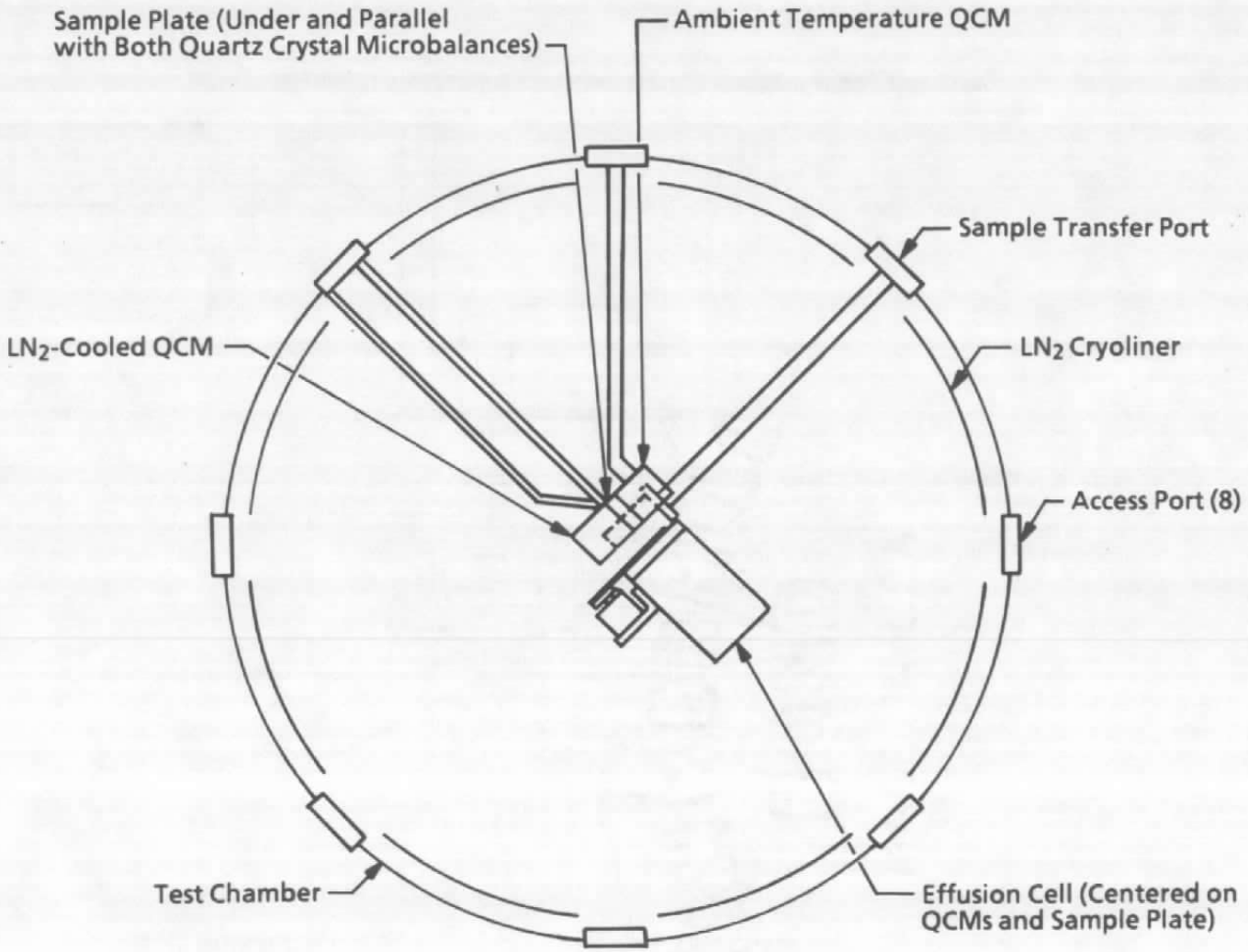

Figure 2. OGC configuration, plan view.

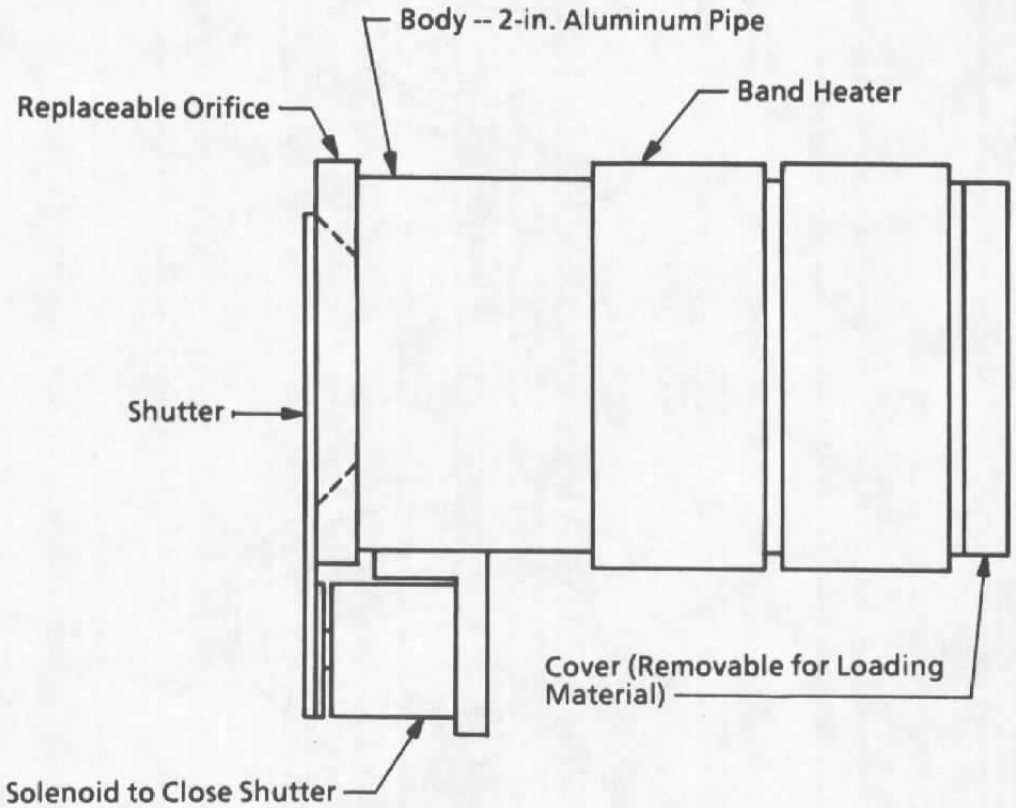

Figure 3. Effusion cell.

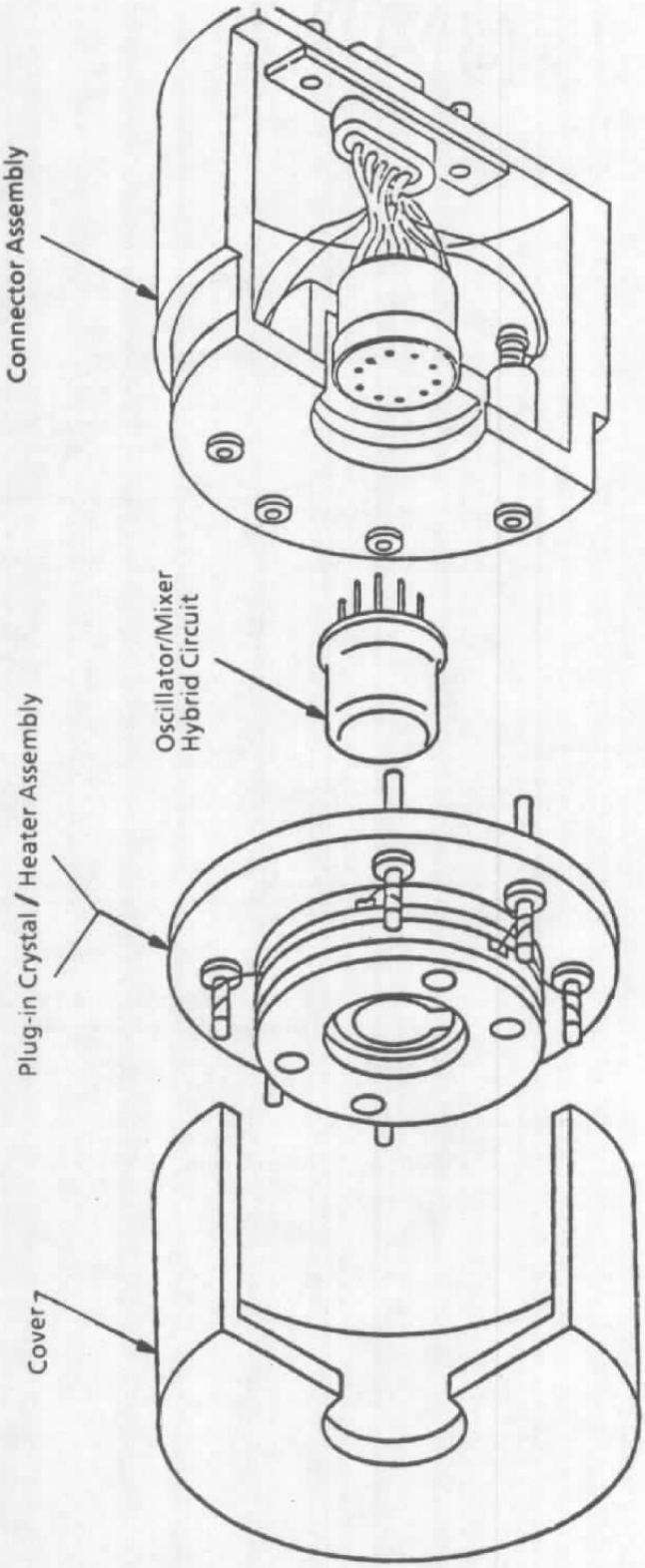

Figure 4. Quartz crystal microbalance (QCM), exploded view.

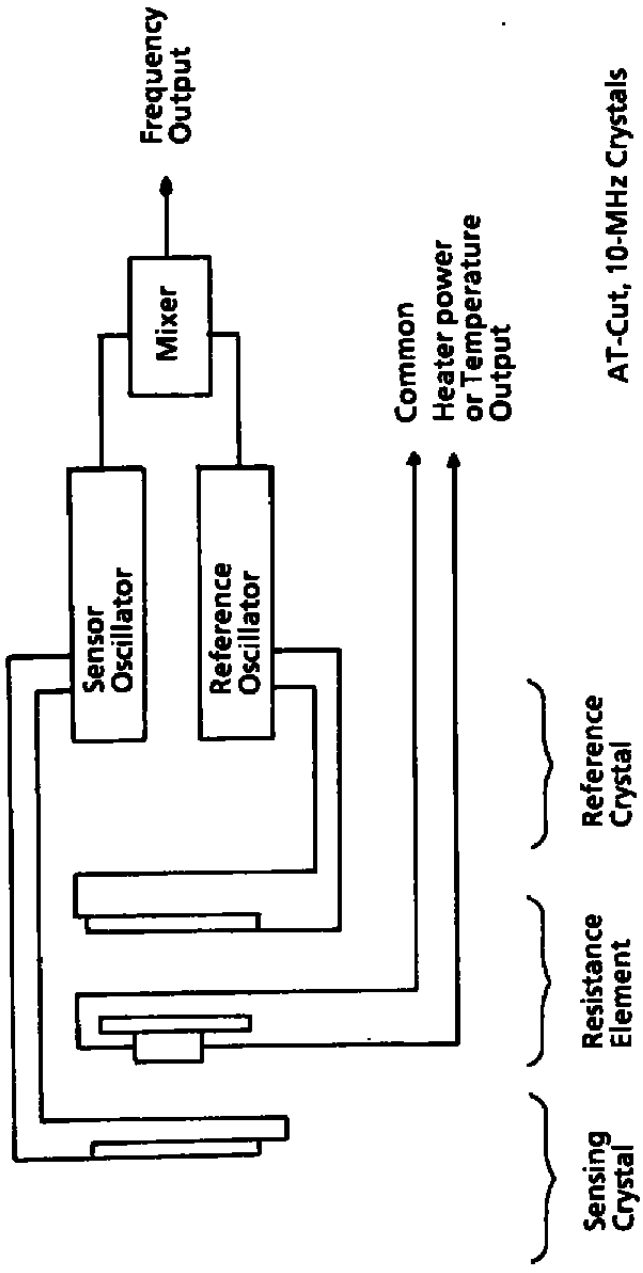

Figure 5. QCM schematic.

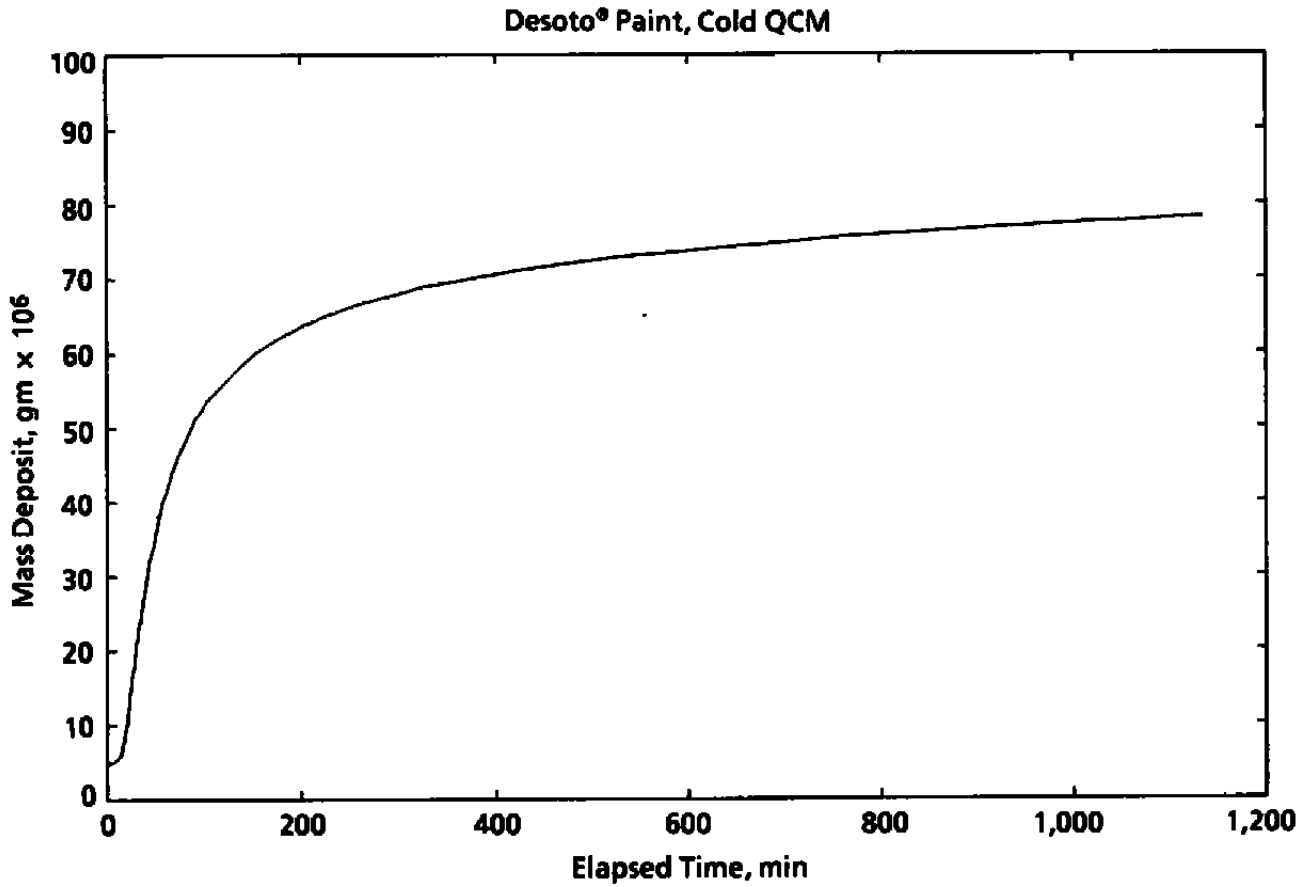

Figure 6. Deposited mass as function of time (cold QCM).

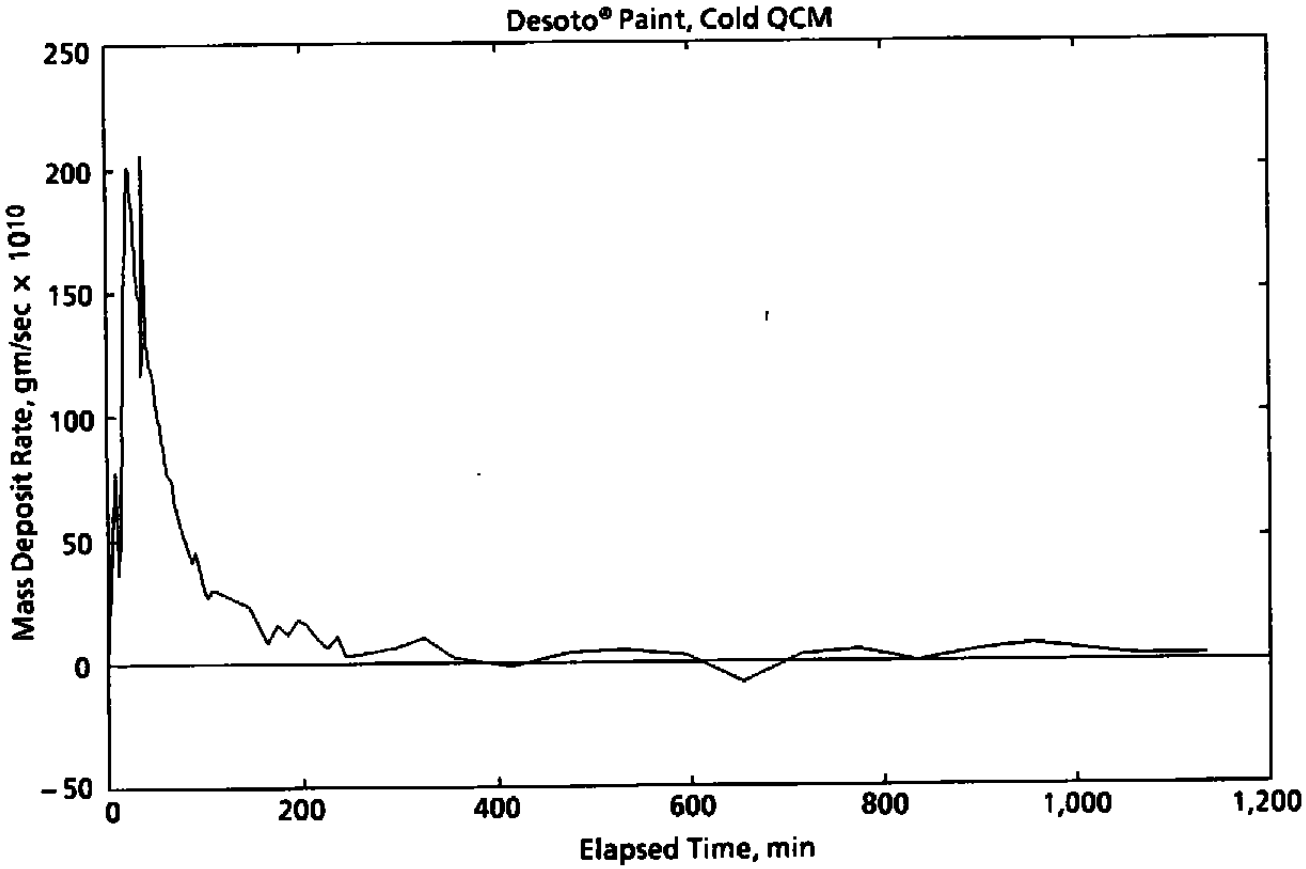

Figure 7. Rate of deposited mass as function of time.

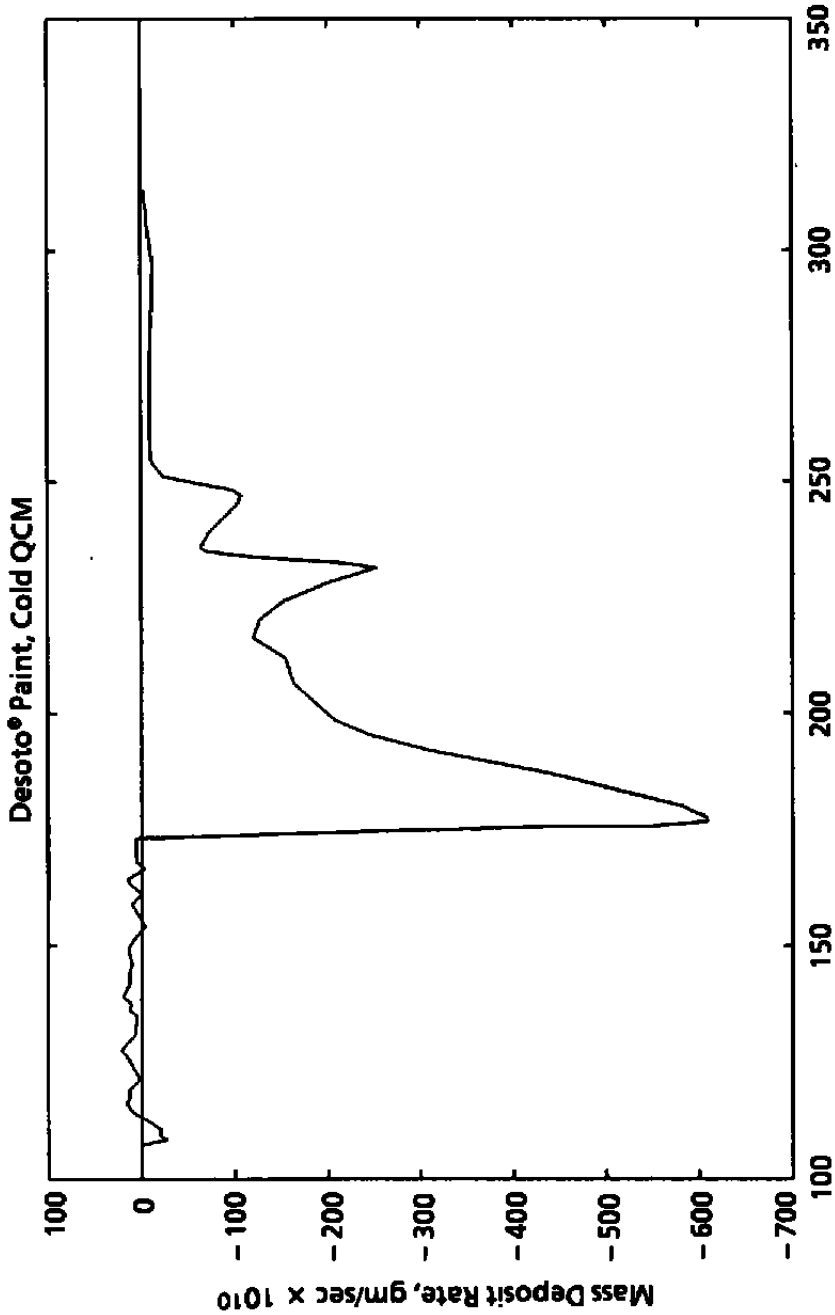

Figure 8. Rate of deposited mass as function of temperature.

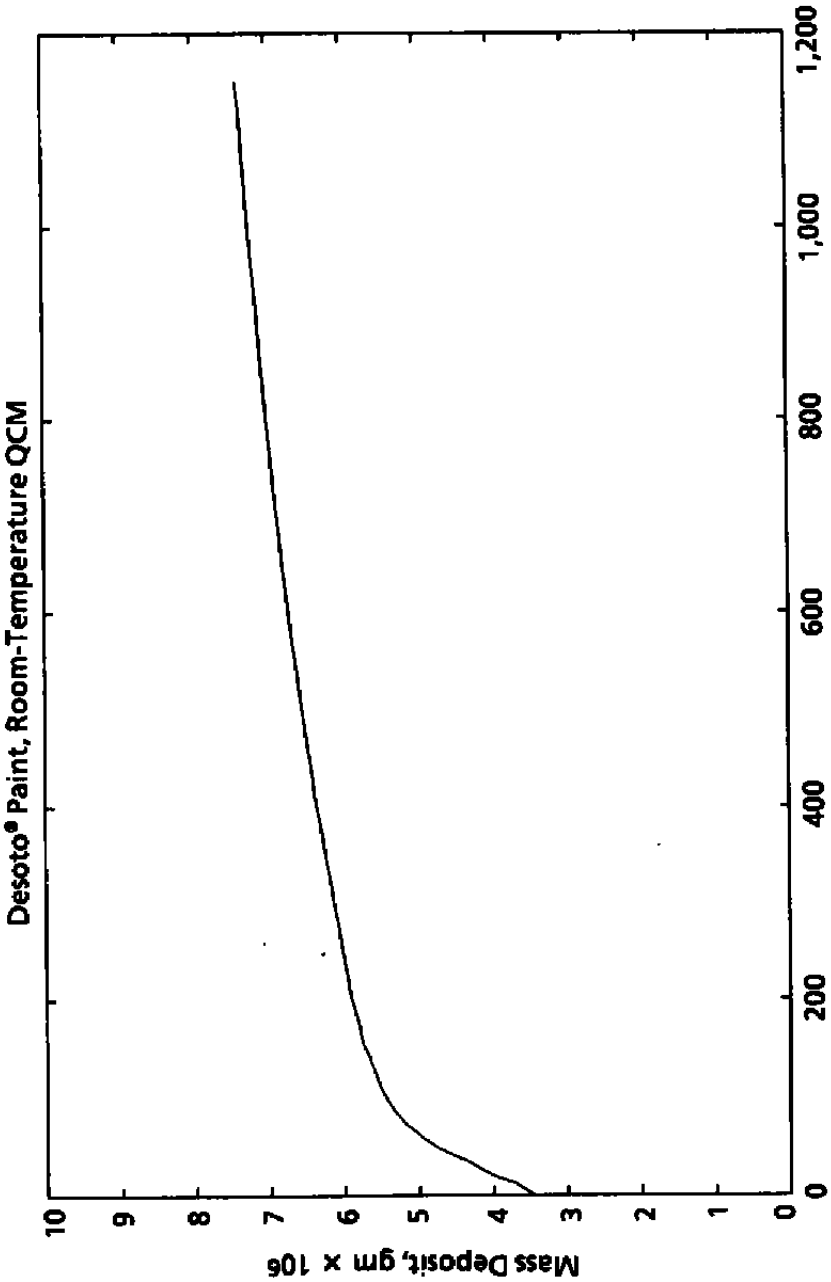

Figure 9. Deposited mass as function of time (room-temperature QCM).

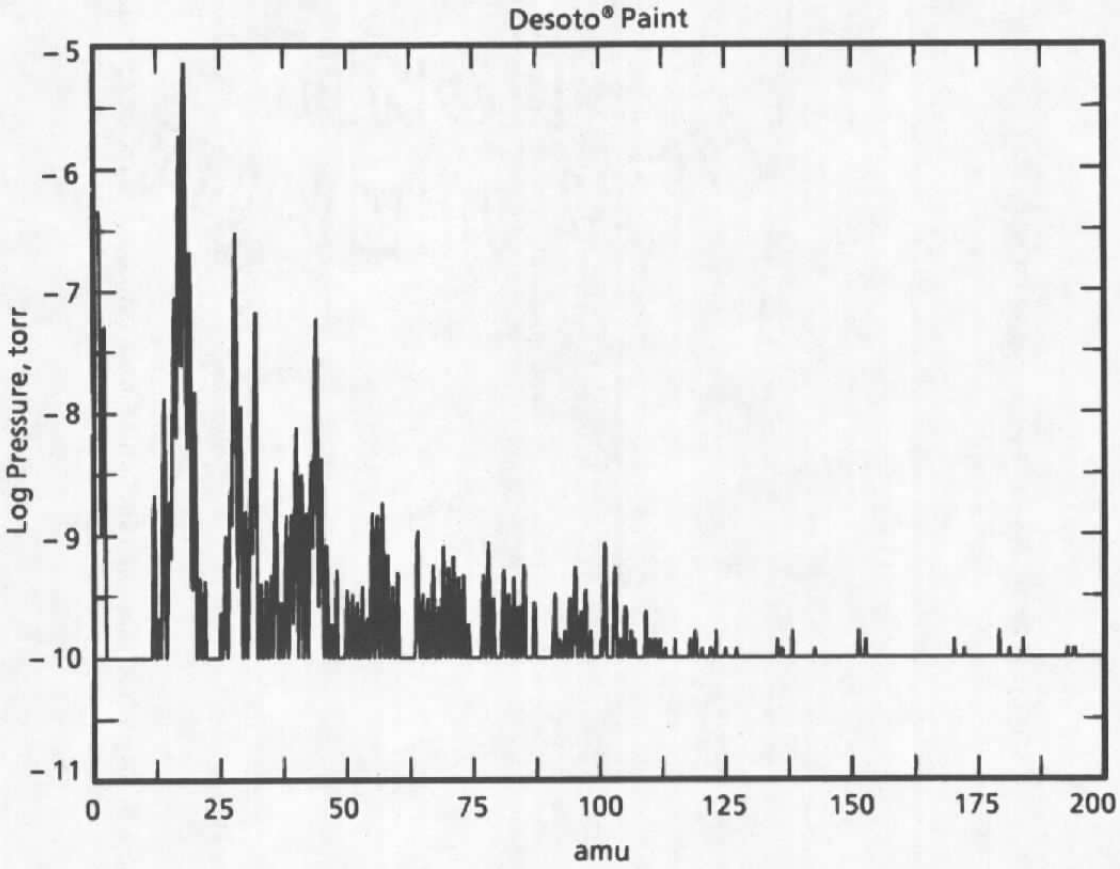

Figure 10. Sample mass spectrum for Desoto® paint.

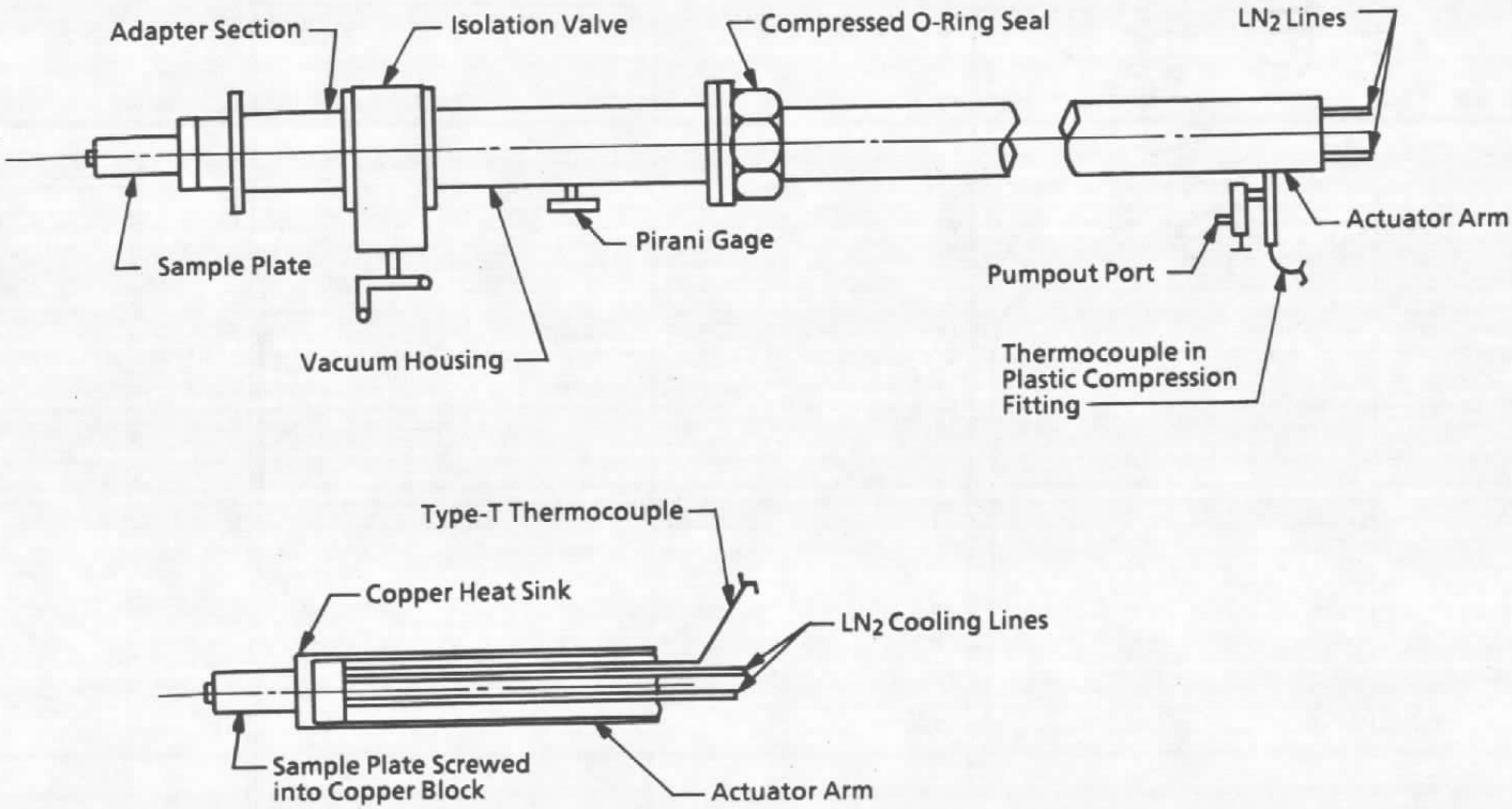

Figure 11. Sample transfer mechanism (STM).

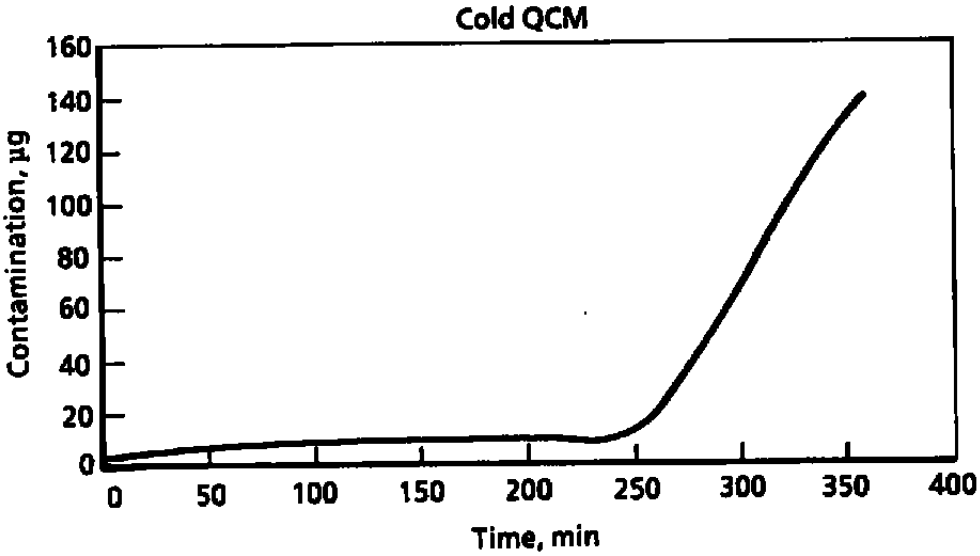

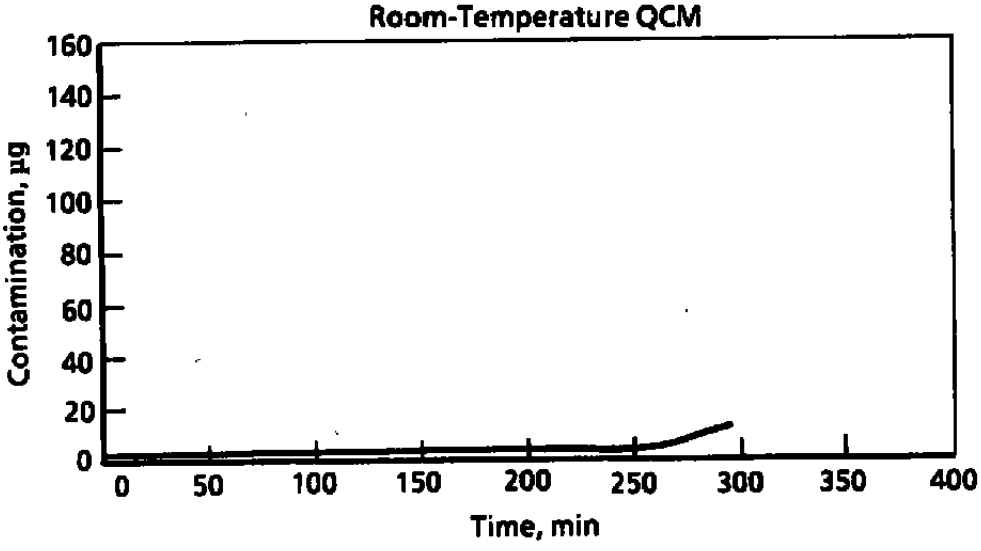

Figure 12. QCM contamination history.

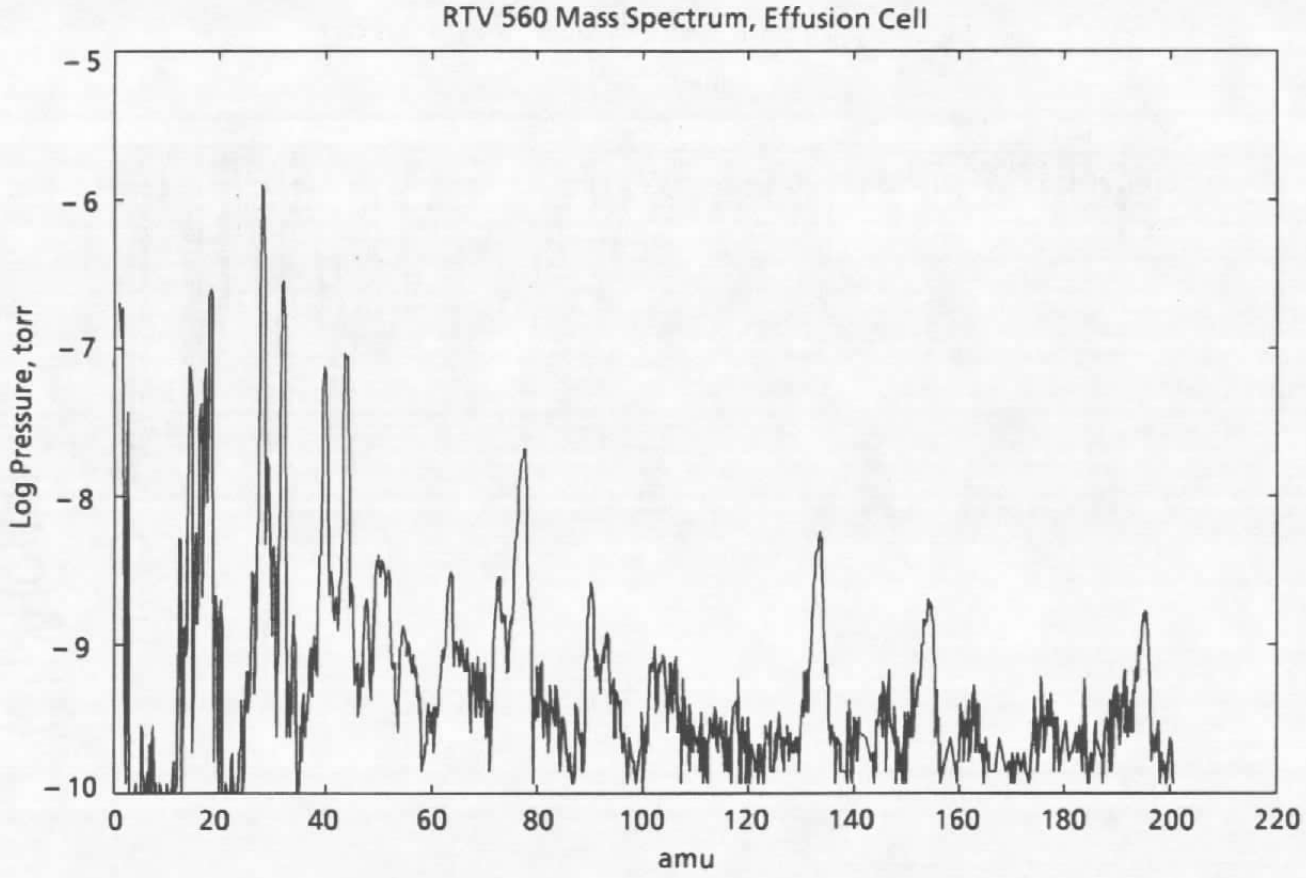

Figure 13. OGC mass spectrum while effusion cell operating at cryogenic conditions.

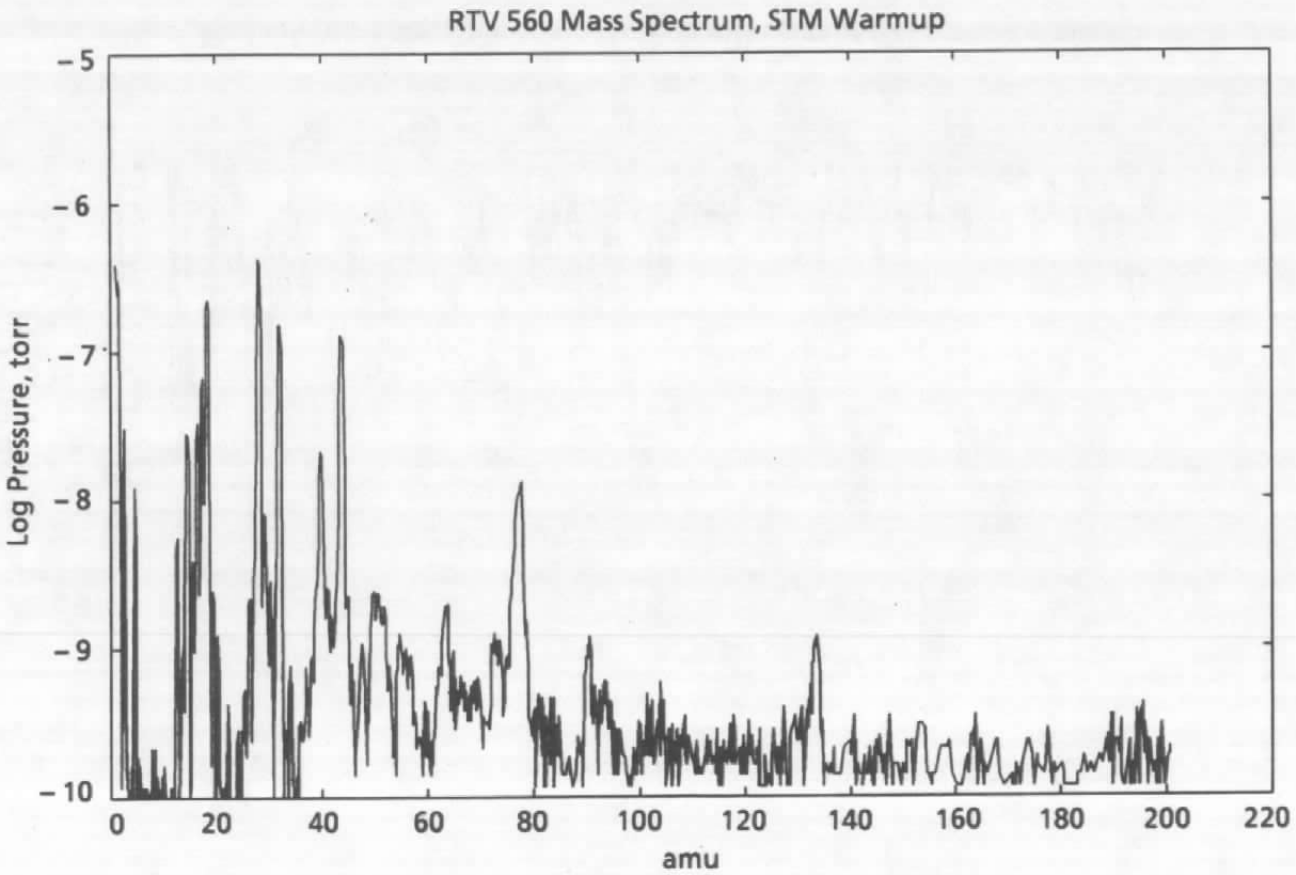

Figure 14. OGC mass spectrum after STM warmup.

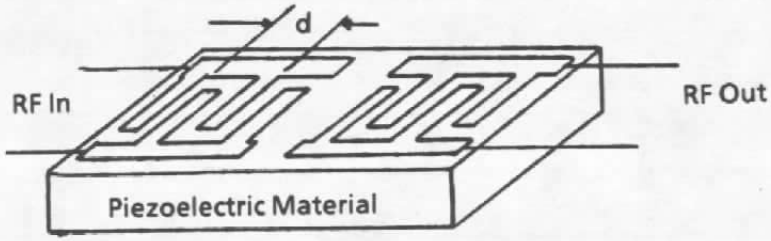

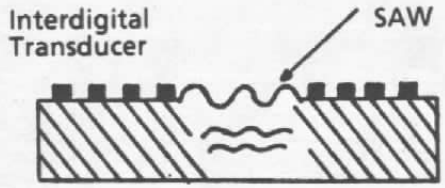

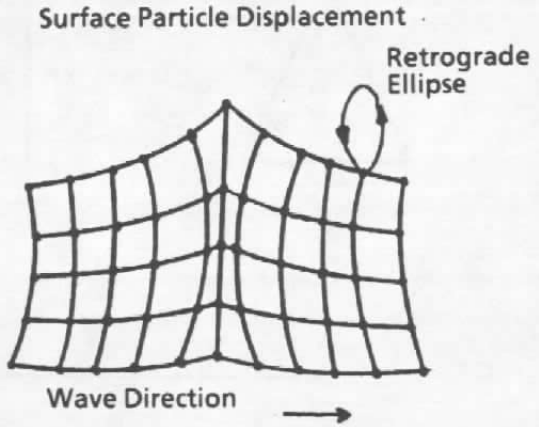

Figure 15. Surface acoustic wave (SAW) generation.

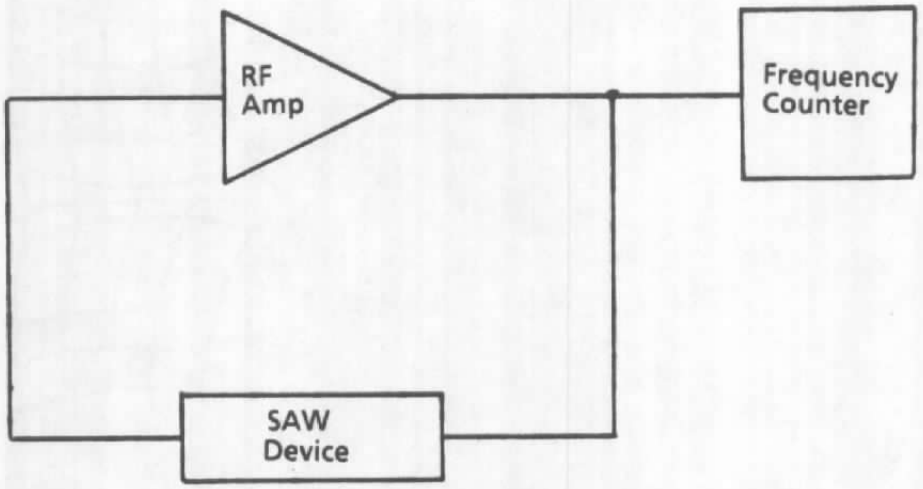

Figure 16. SAW delay line oscillator system.

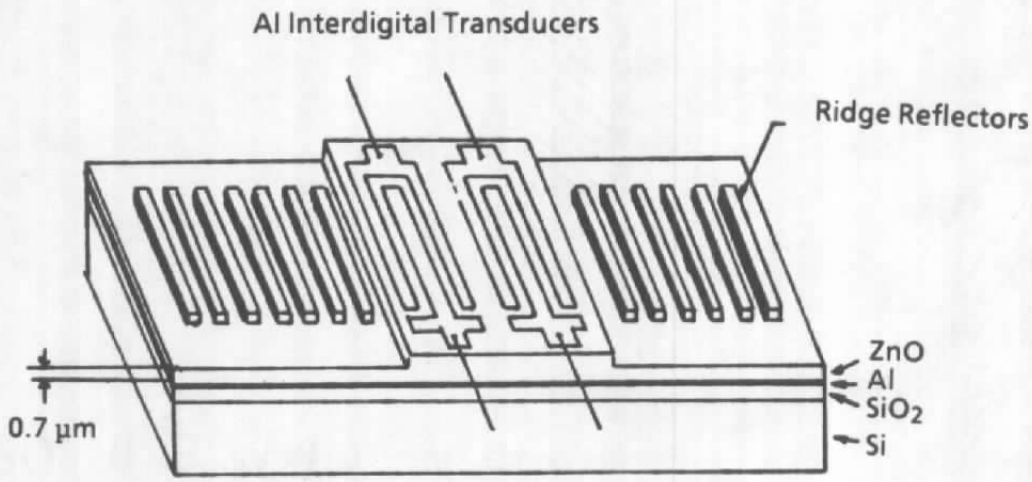

Zn0-on-Si SAW Resonator
f = 109 MHz, λ = 40.6 μm

Figure 17. Sandia SAW device.

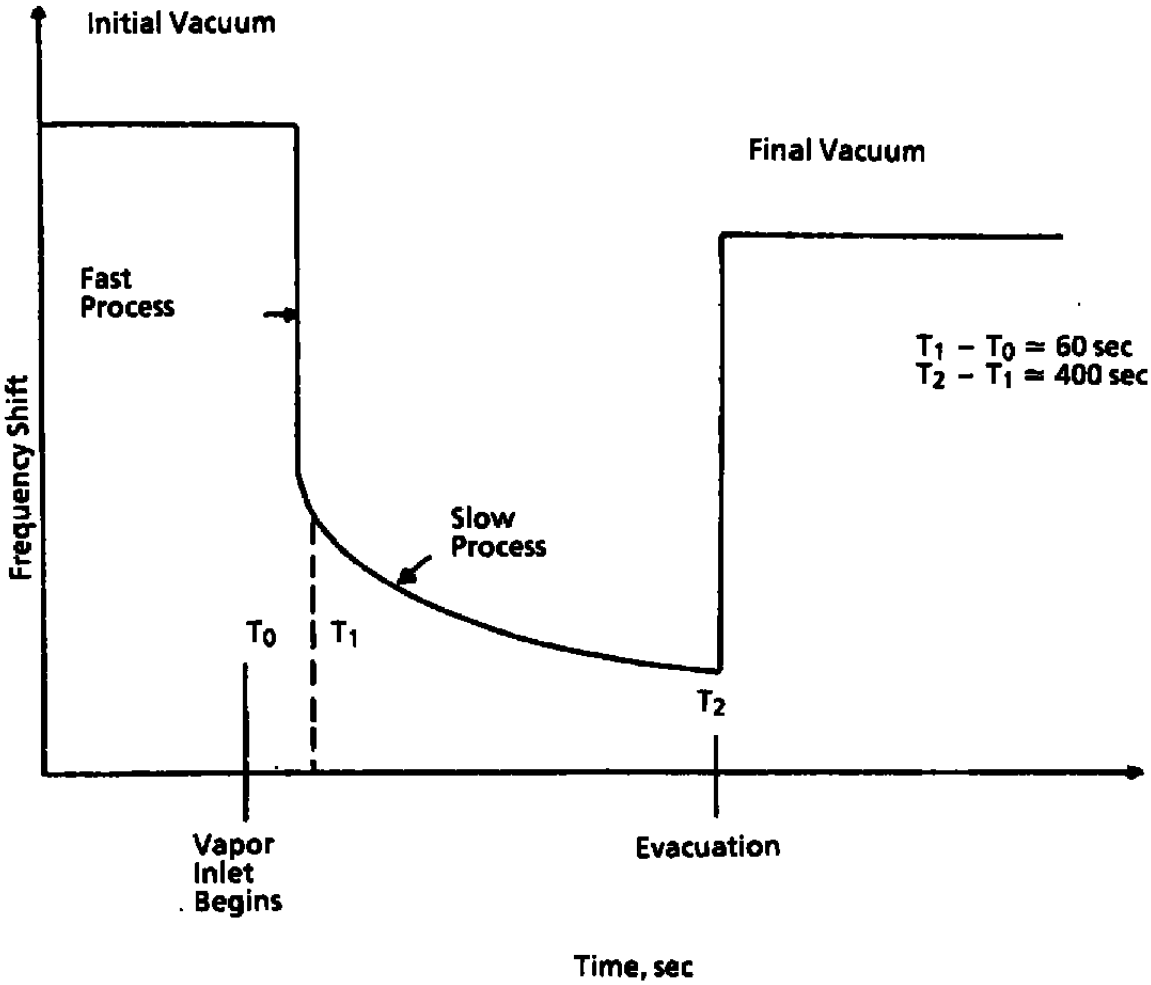

Figure 18. Time response of porous SAW sensor.

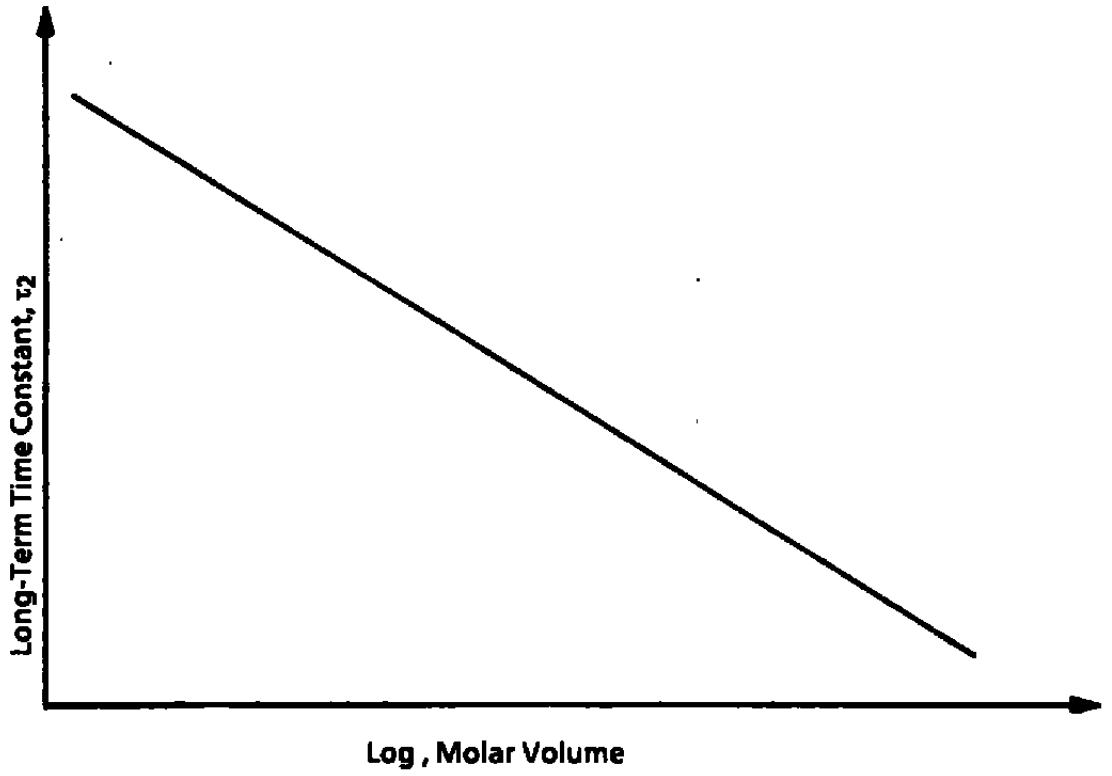

Figure 19. SAW long-term time constant versus molecular size.

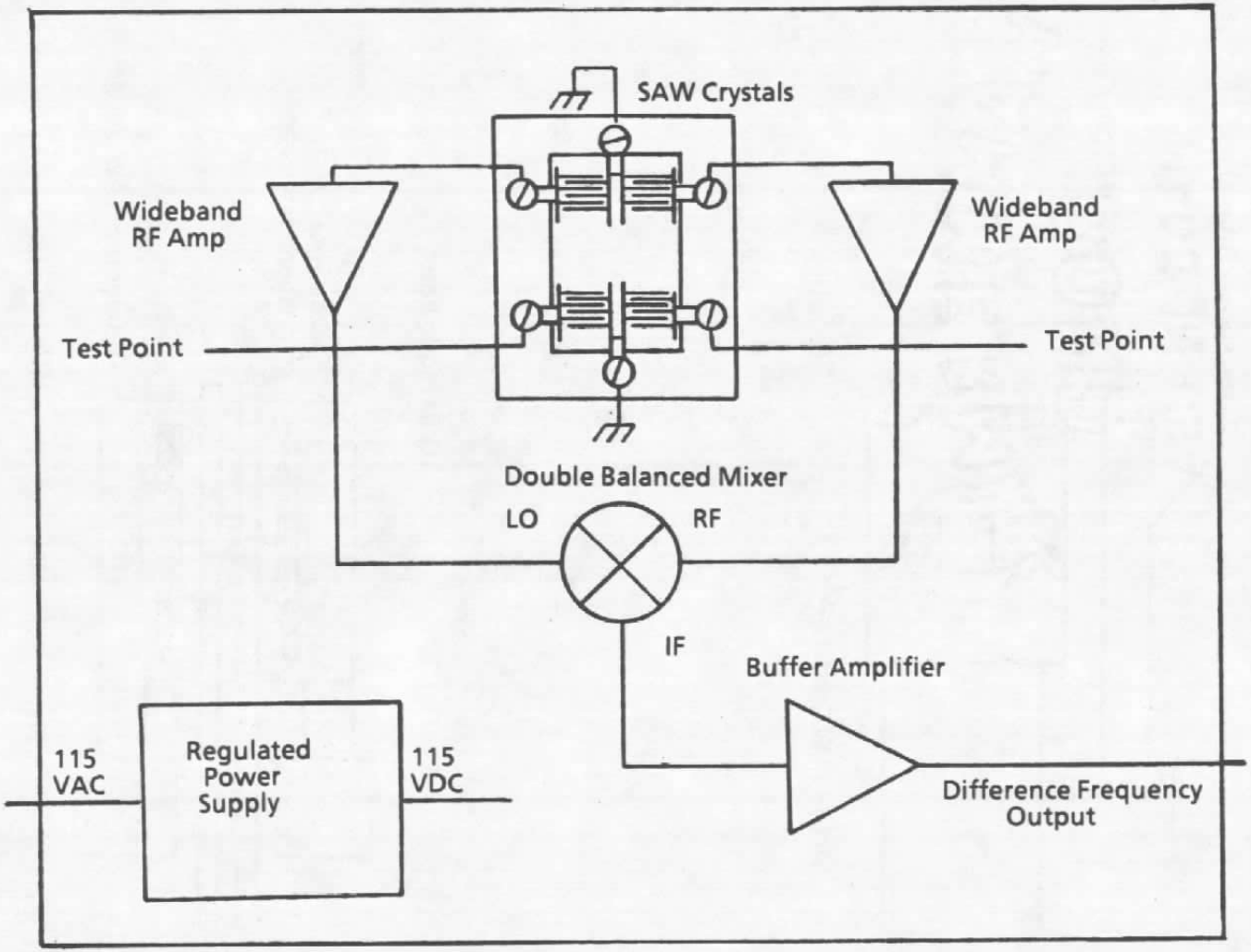

Figure 20. 158-MHz dual SAW delay line oscillator system diagram.

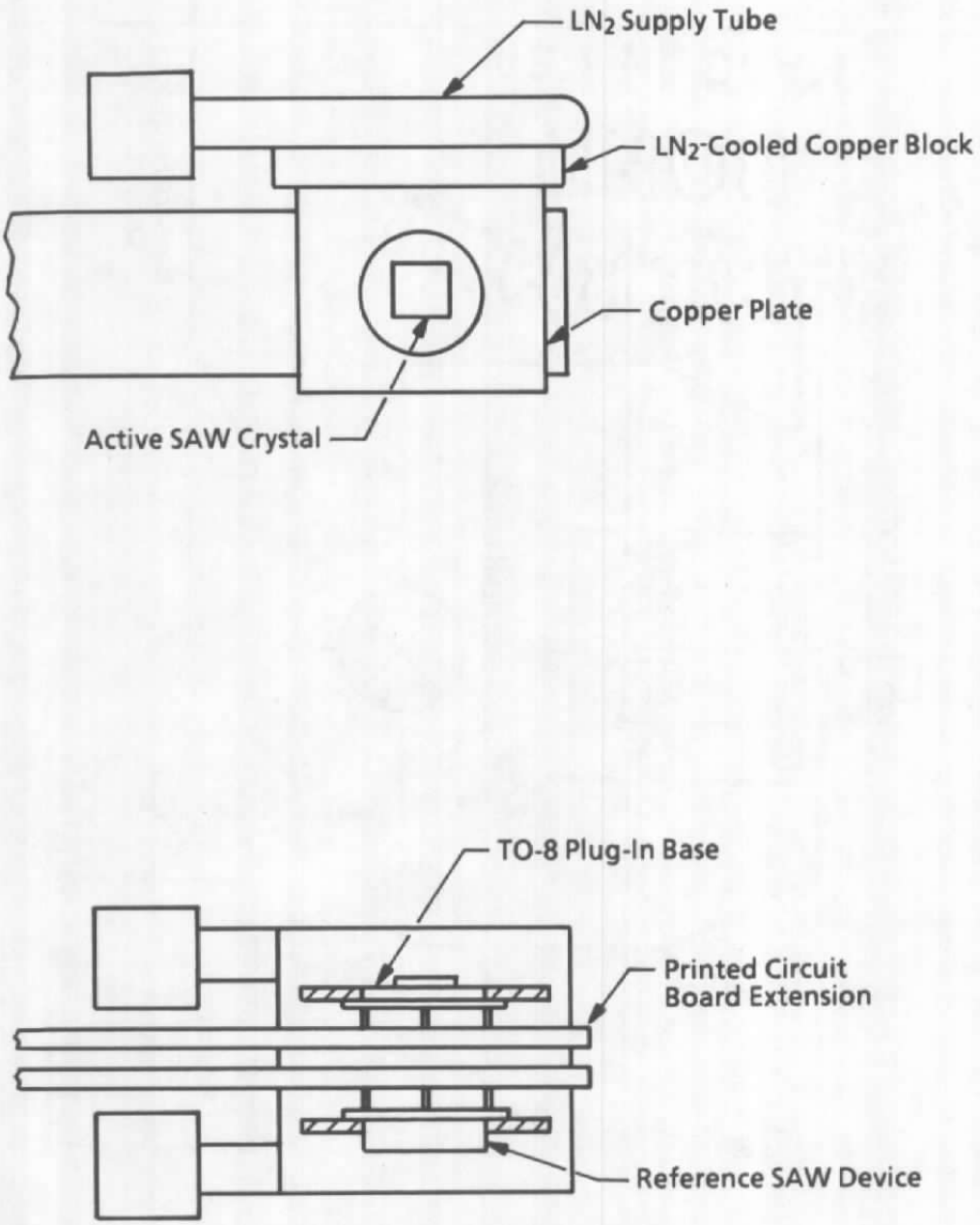

Figure 21. Cooling system for SAW crystals.

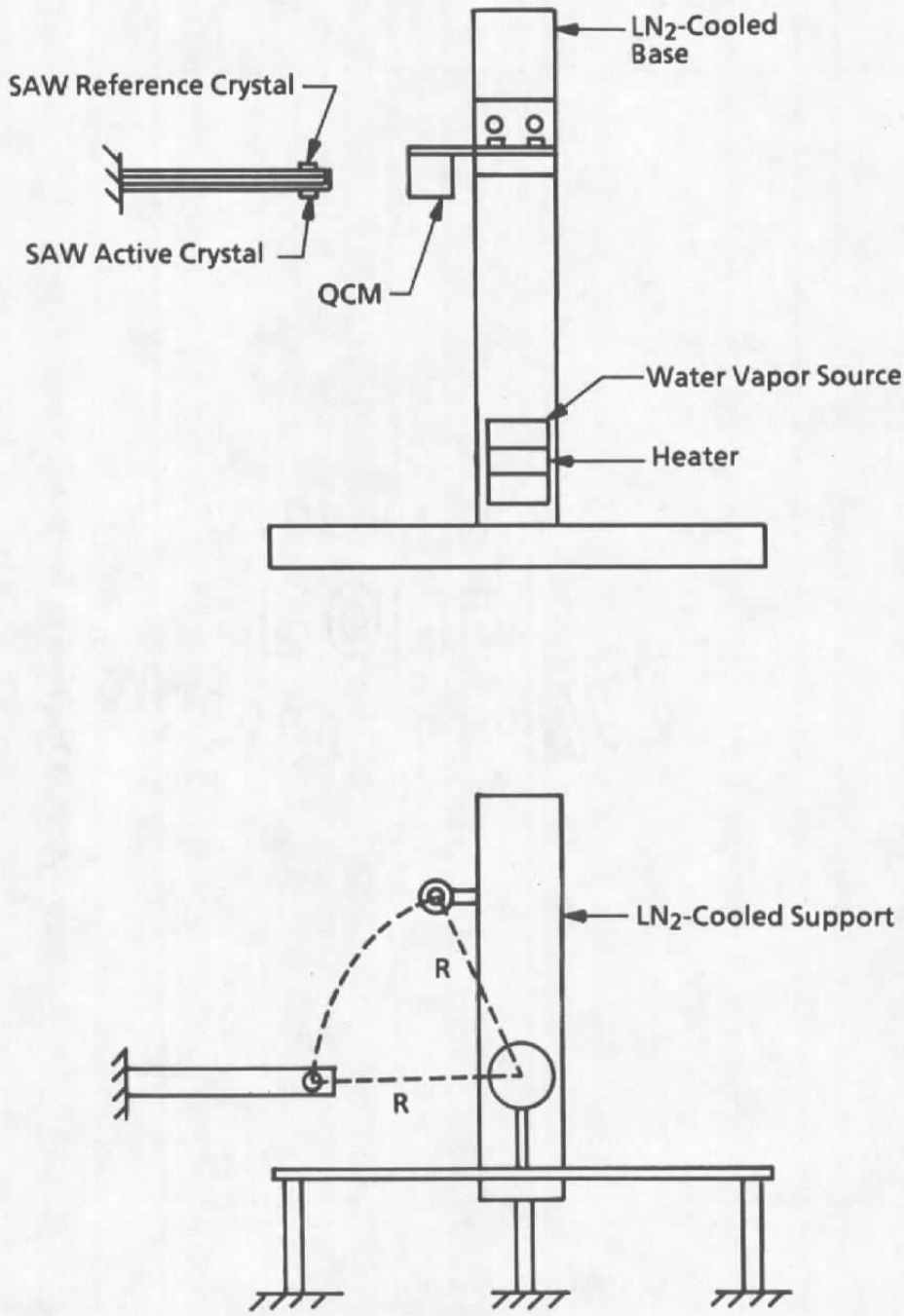

Figure 22. Experimental setup for vapor deposition test.

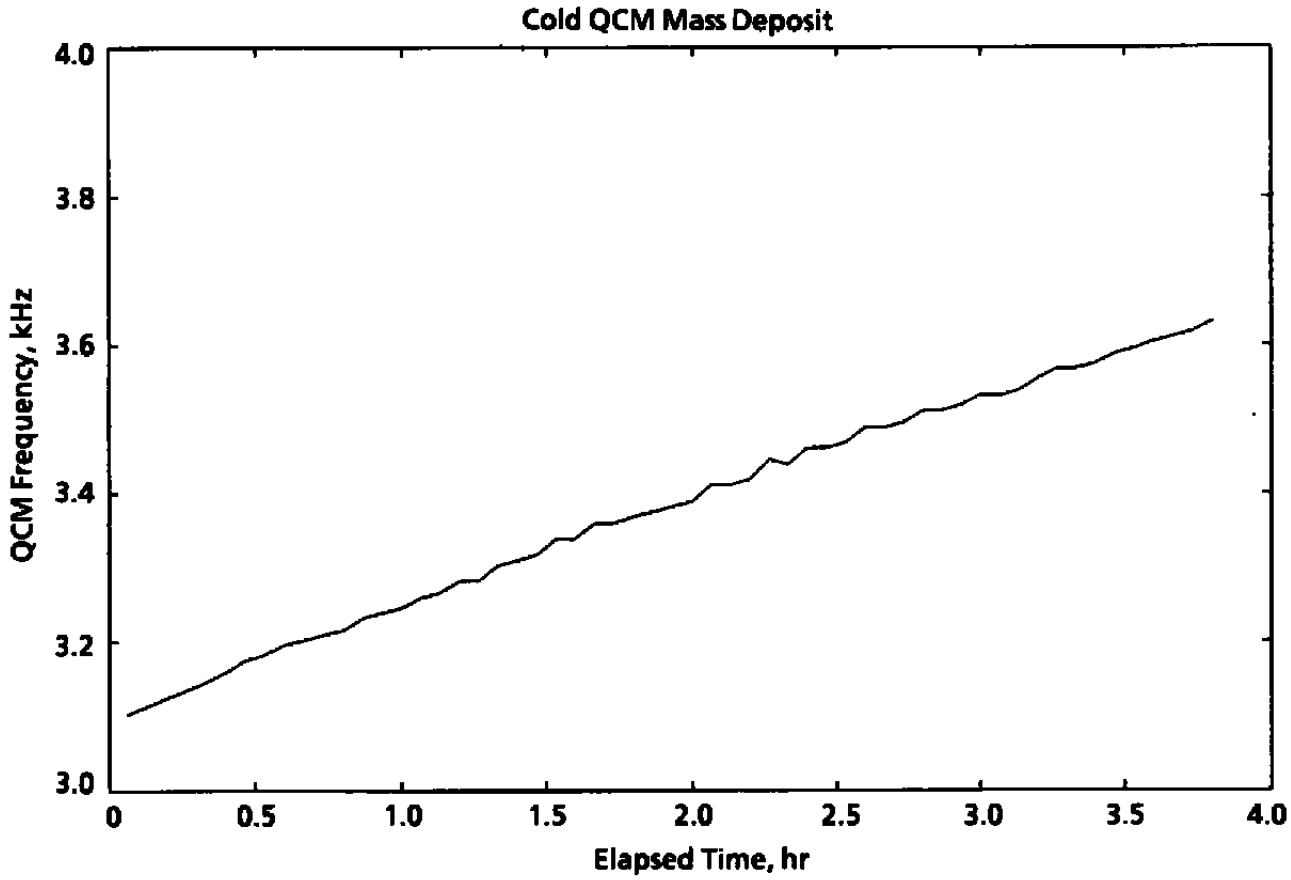

Figure 23. QCM frequency as function of time.

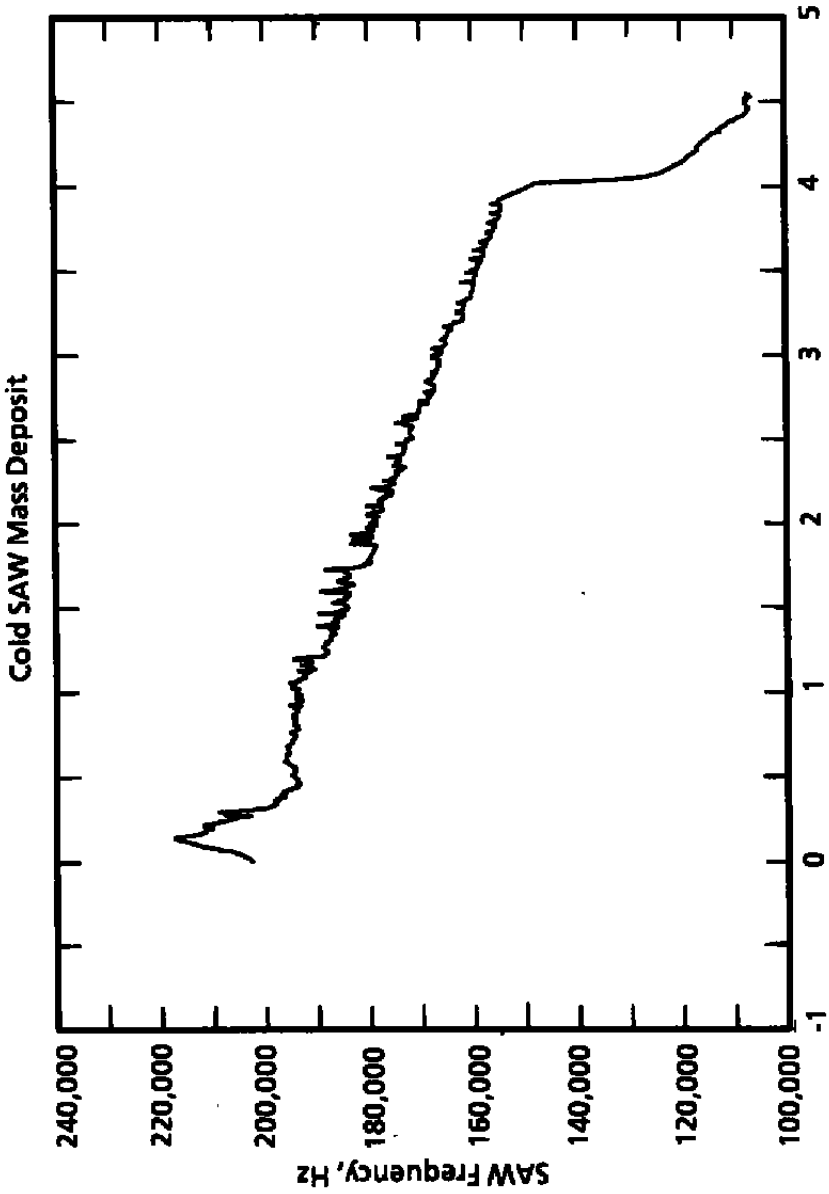

Figure 24. SAW frequency as function of time.

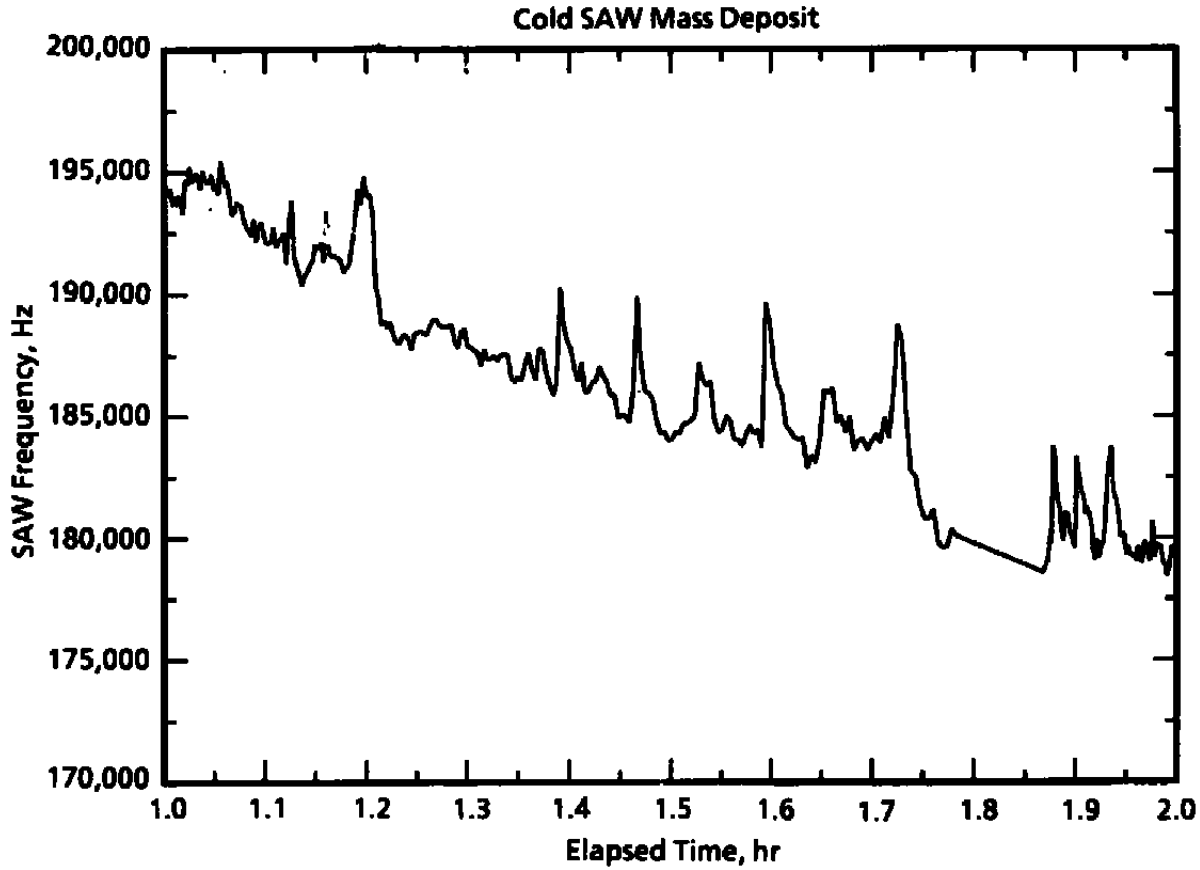

Figure 25. SAW frequency as function of time (expanded time scale).

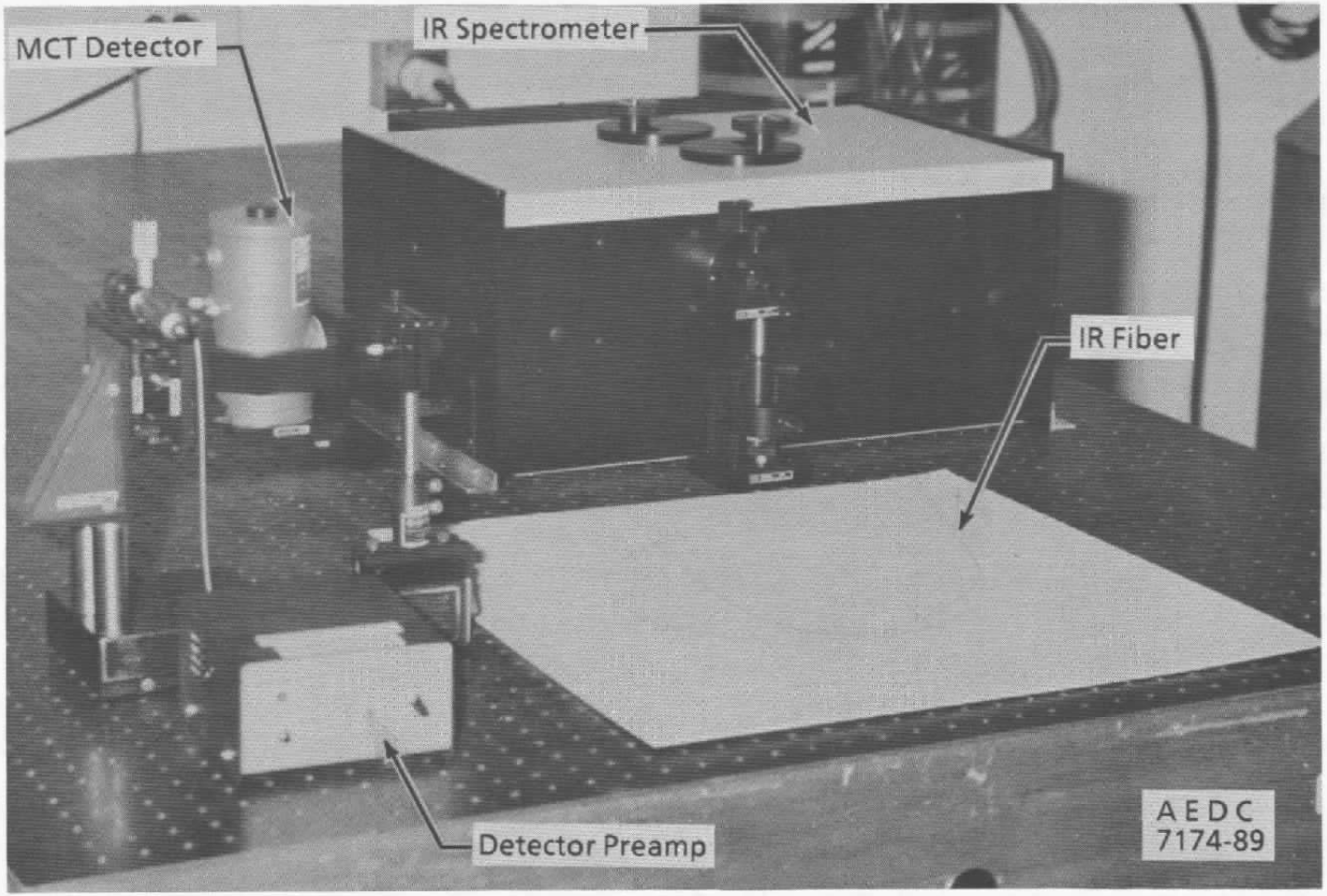

Figure 26. Fiber-optic transmission laboratory setup.

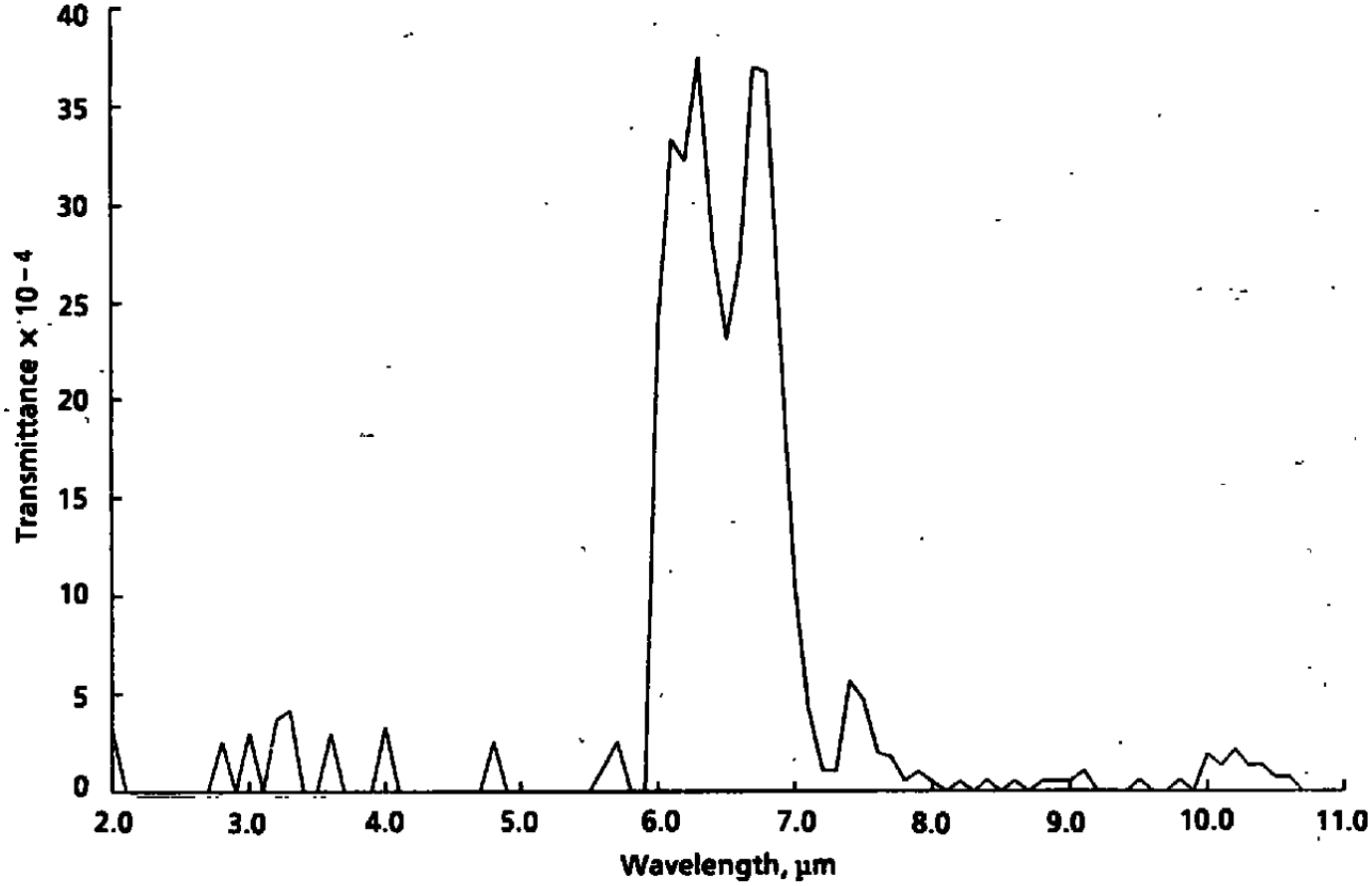

Figure 27. Chalcogenide IR fiber transmittance.

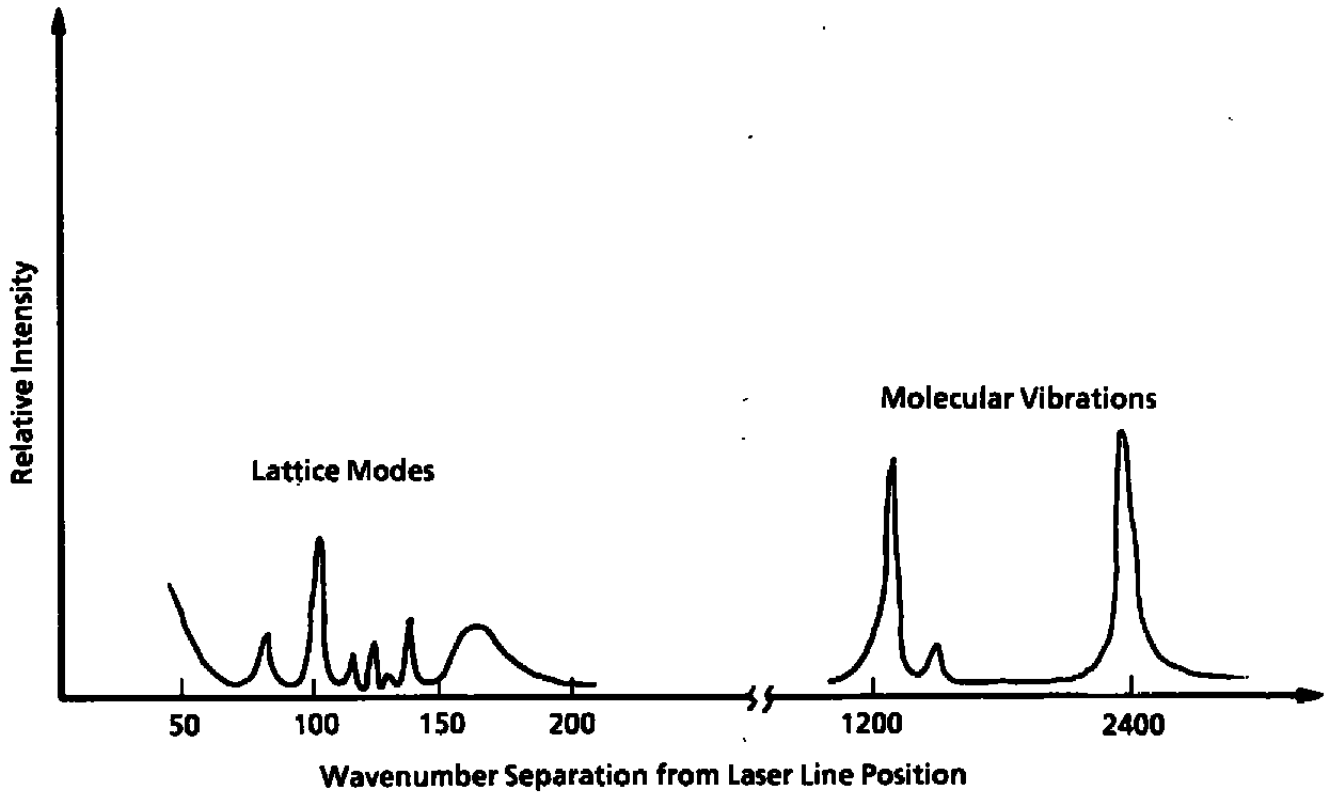

Figure 28. Typical Raman spectrum from condensed gas cryodeposit.

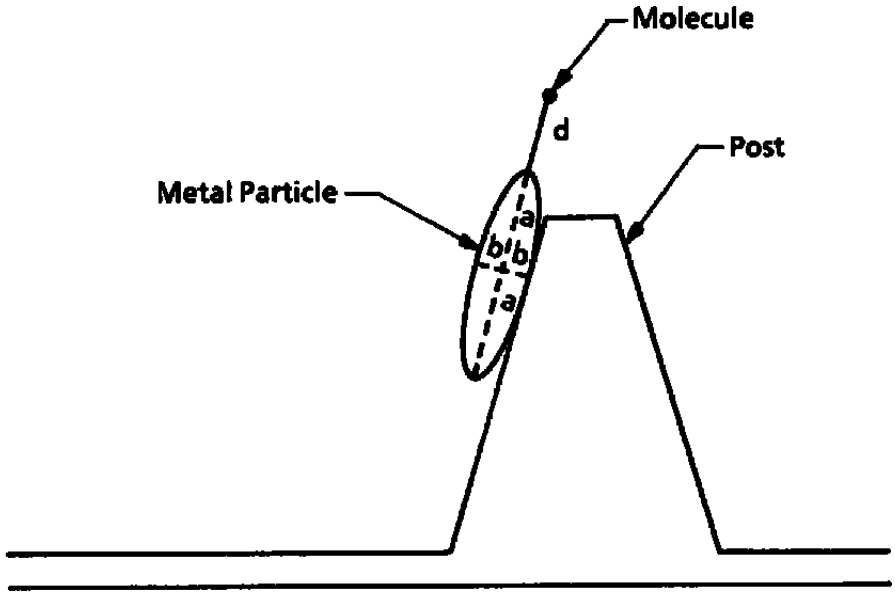

Figure 29. Spheriodal representation of SERS sample plate surface.

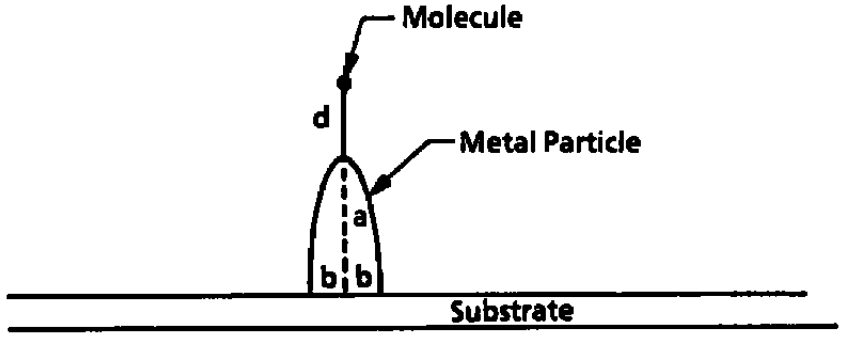

Figure 30. Hemi-spheriodal representation of SERS sample plate surface.

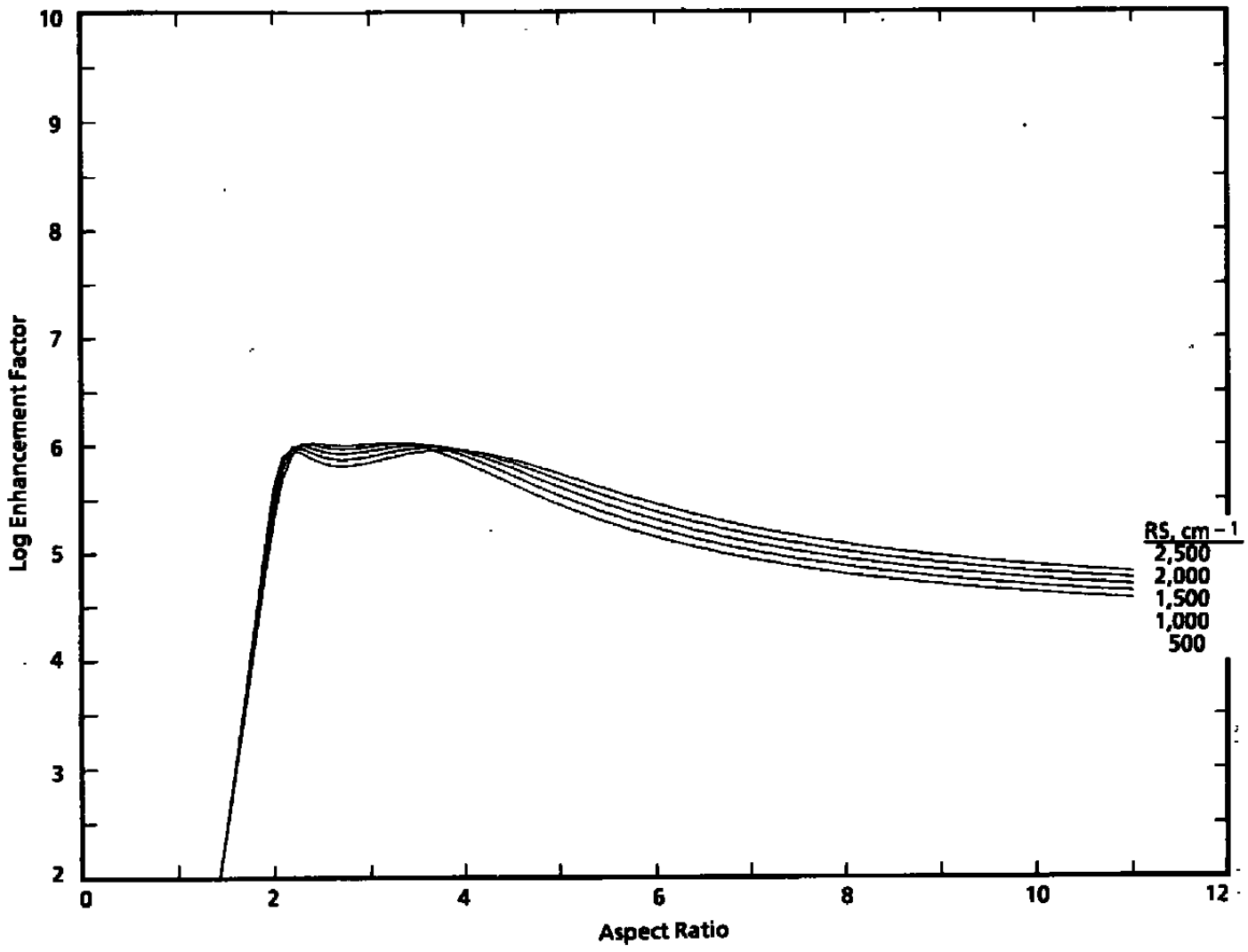

Figure 31. SERS EF for silver spheroids, λ_0 = 5,145 Å, a = 600 Å, d = 3 Å.

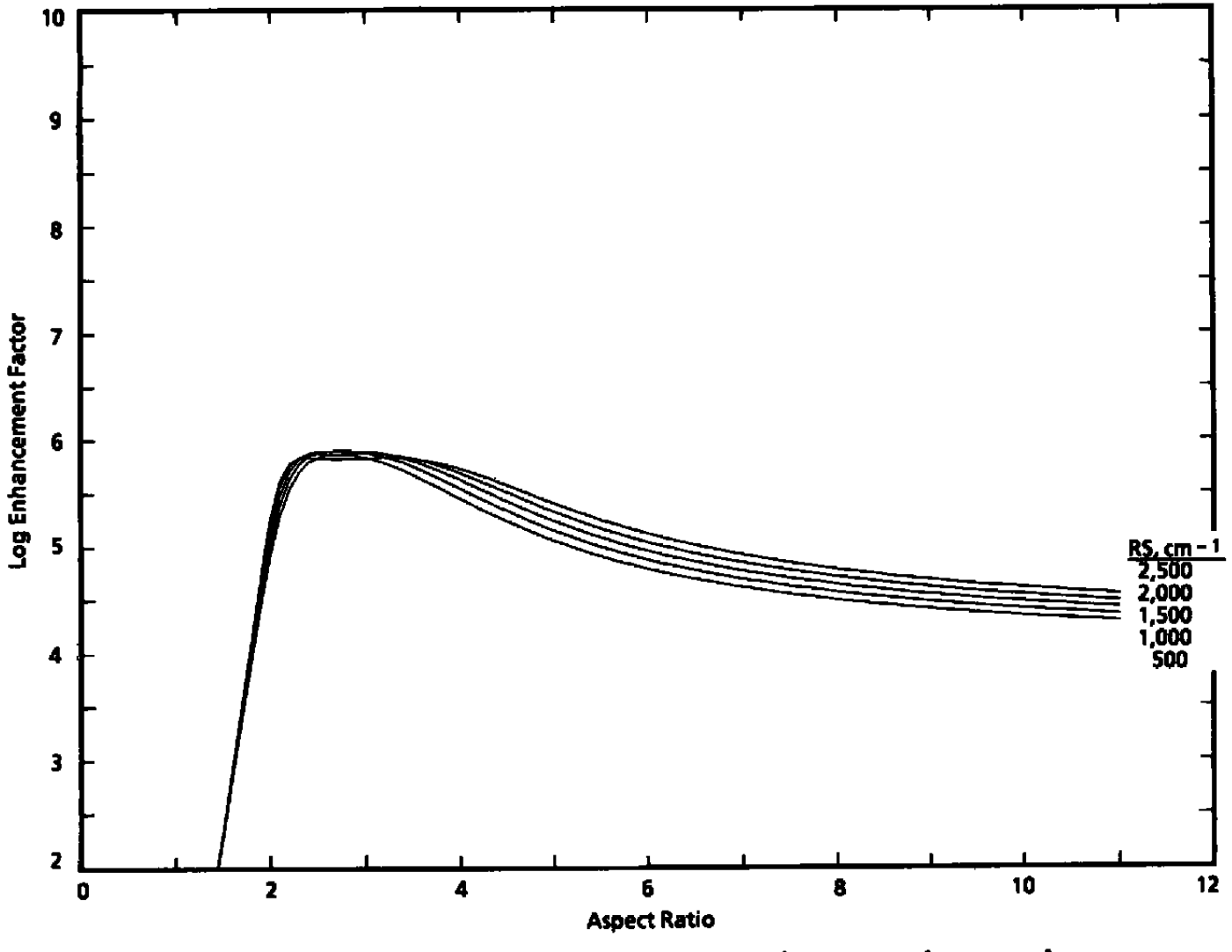

Figure 32. SERS EF for silver spheroids, λ_o = 4,800 Å, a = 600 Å, d = 3 Å.

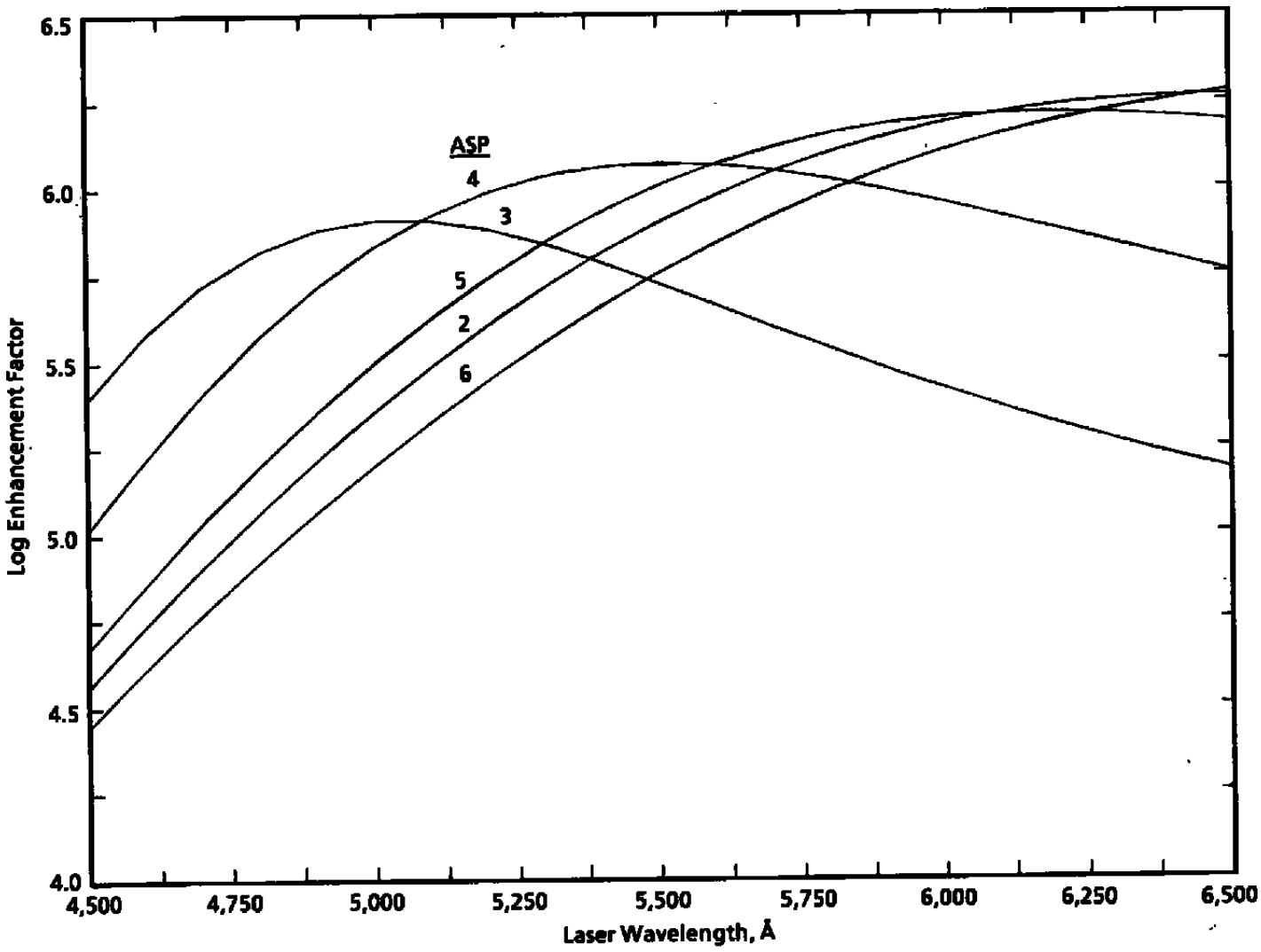

Figure 33. SERS EF for Ag spheroids, RS = 2,000 cm^{-1}, a = 600 Å, d = 3 Å.

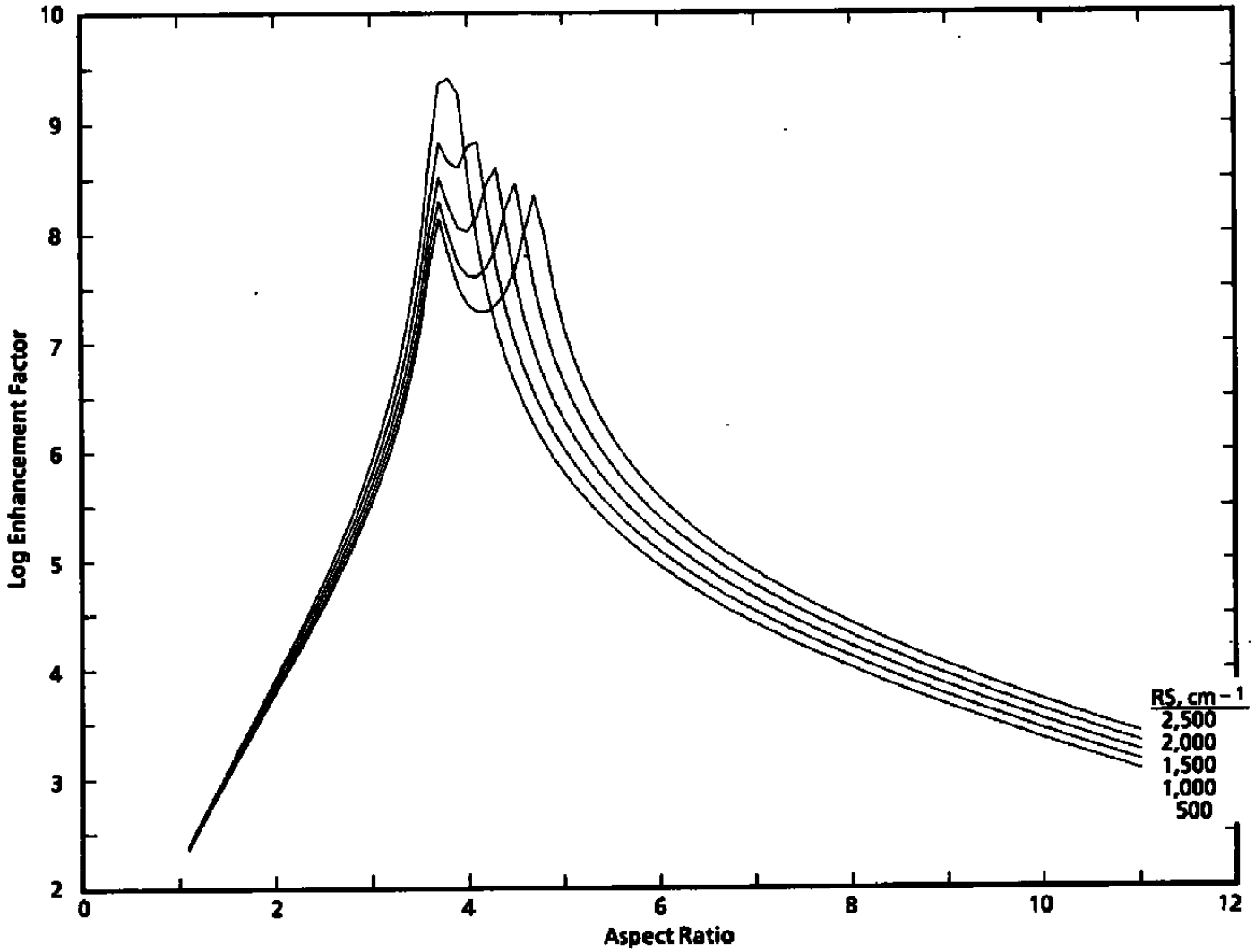

Figure 34. SERS EF for Ag hemi-spheroids, λ_o = 5,145 Å, a = 600 Å, d = 3 Å.

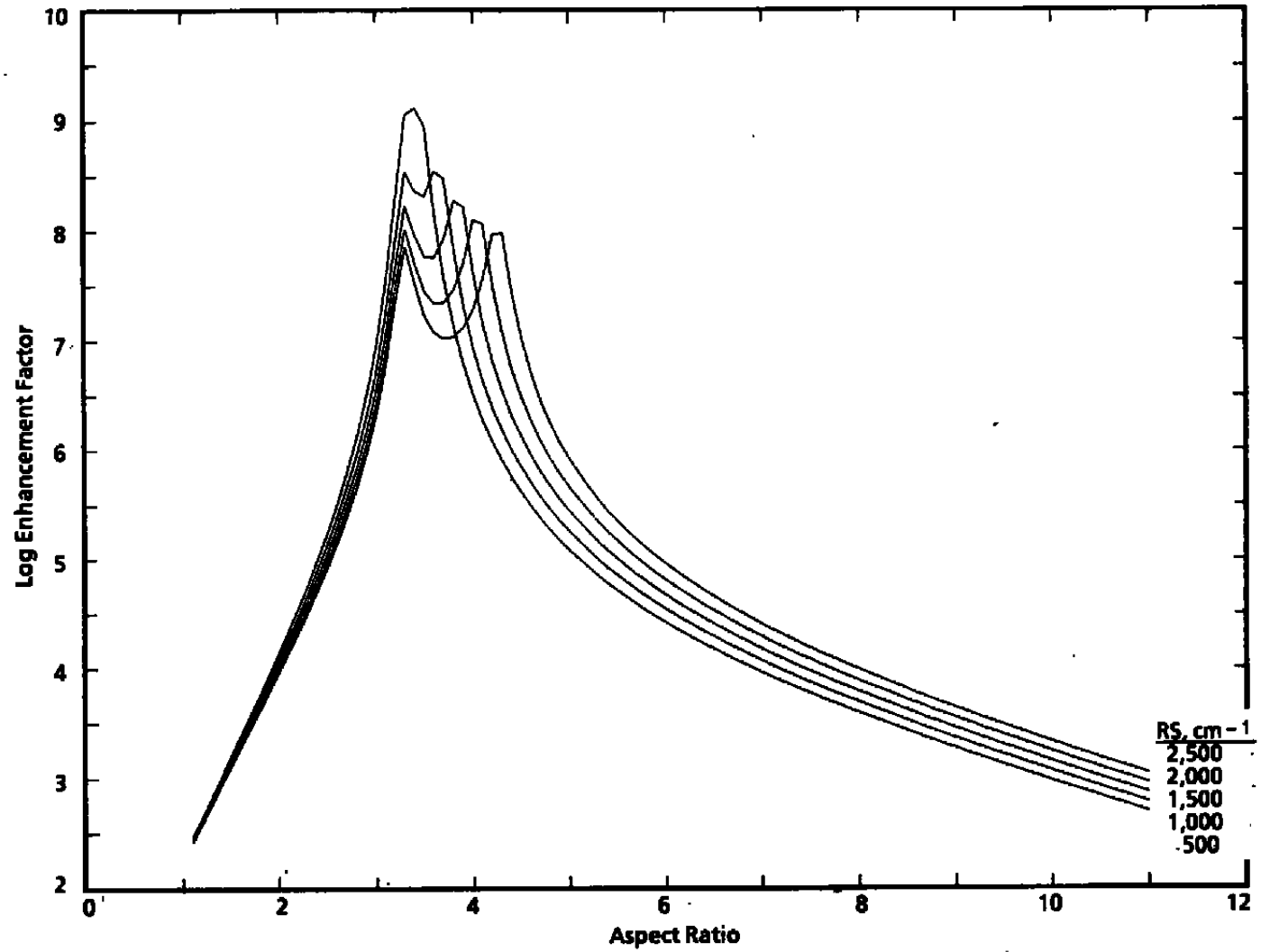

Figure 35. SERS EF for Ag hemi-spheroids, λ_o = 4,800 Å, a = 600 Å, d = 3 Å.

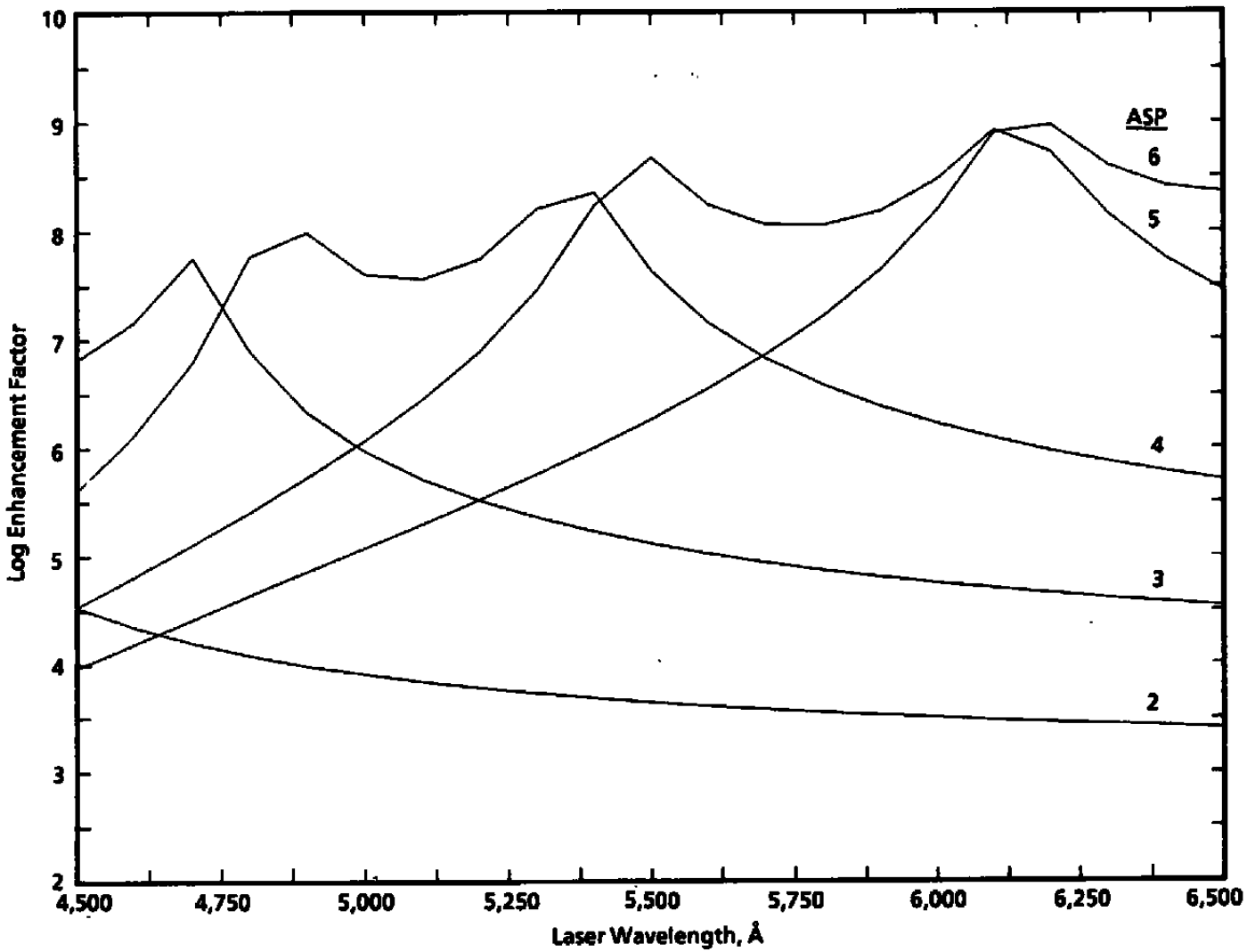

Figure 36. SERS EF for Ag hemi-spheroids, RS = 2,000 cm^{-1}, a = 600 Å, d = 3 Å.

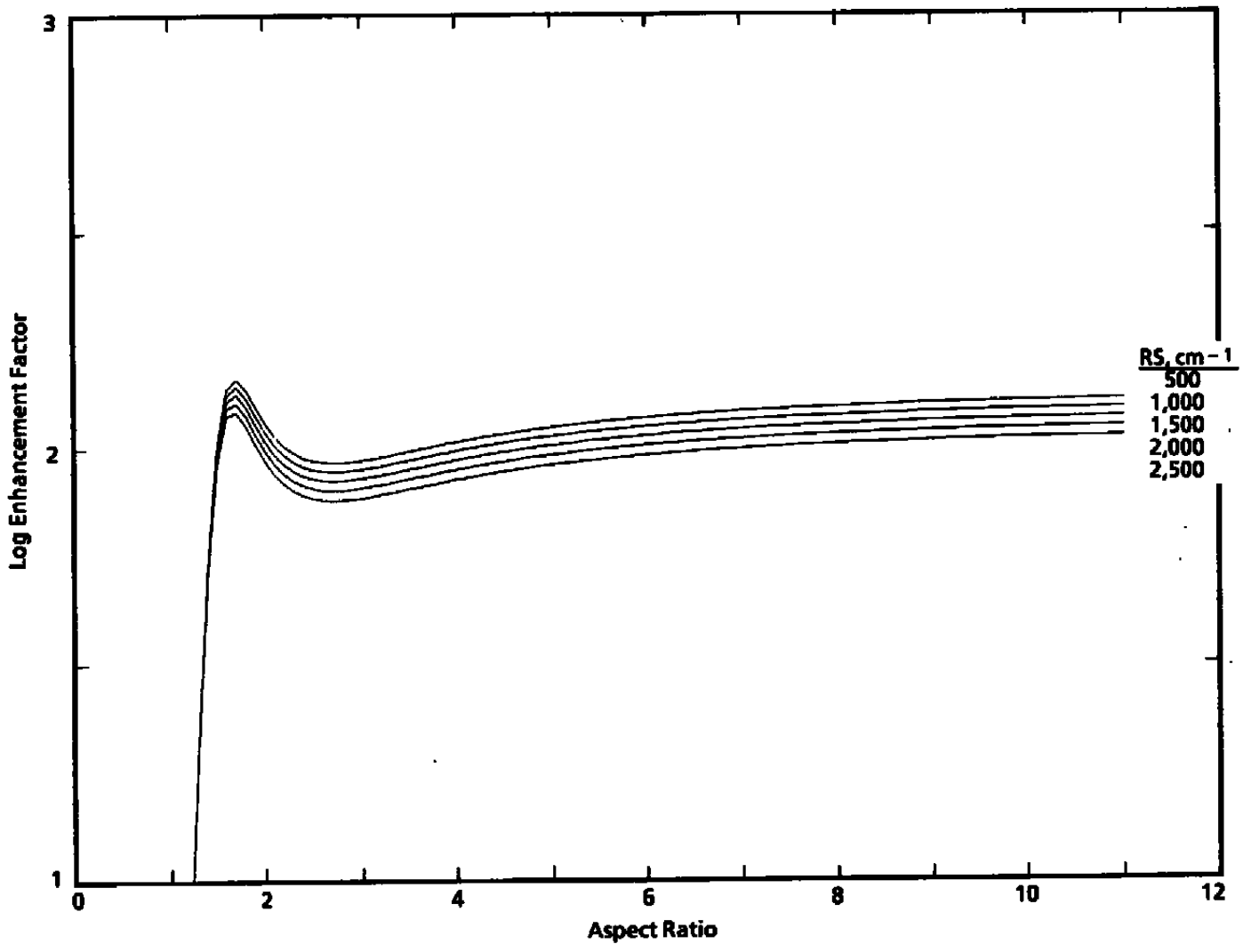

Figure 37. SERS EF for In spheroids, λ_o = 5,145 Å, a = 600 Å, d = 3 Å.

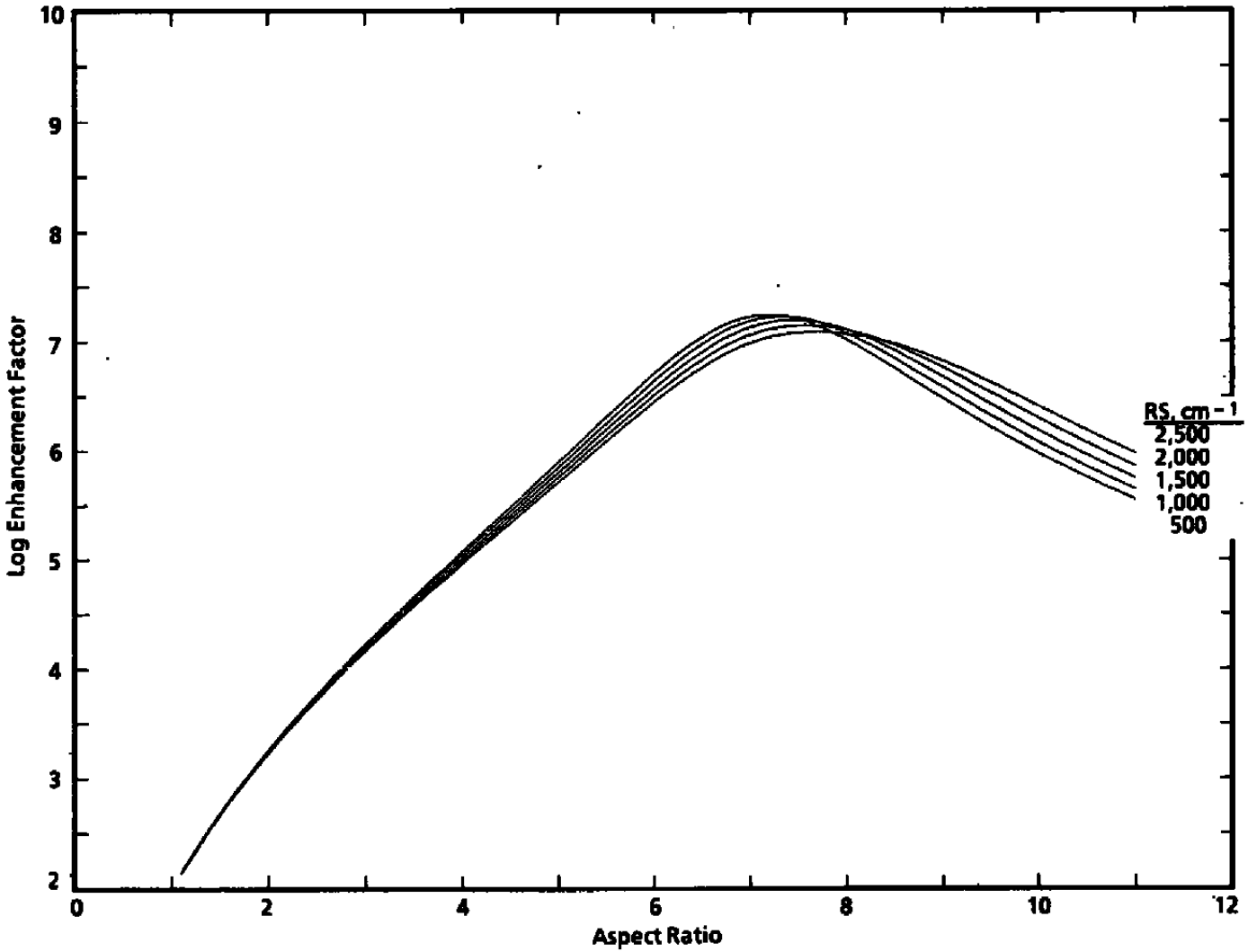

Figure 38. SERS EF for In hemi-spheroids, λ_o = 5,145 Å, a = 600 Å, d = 3 Å.

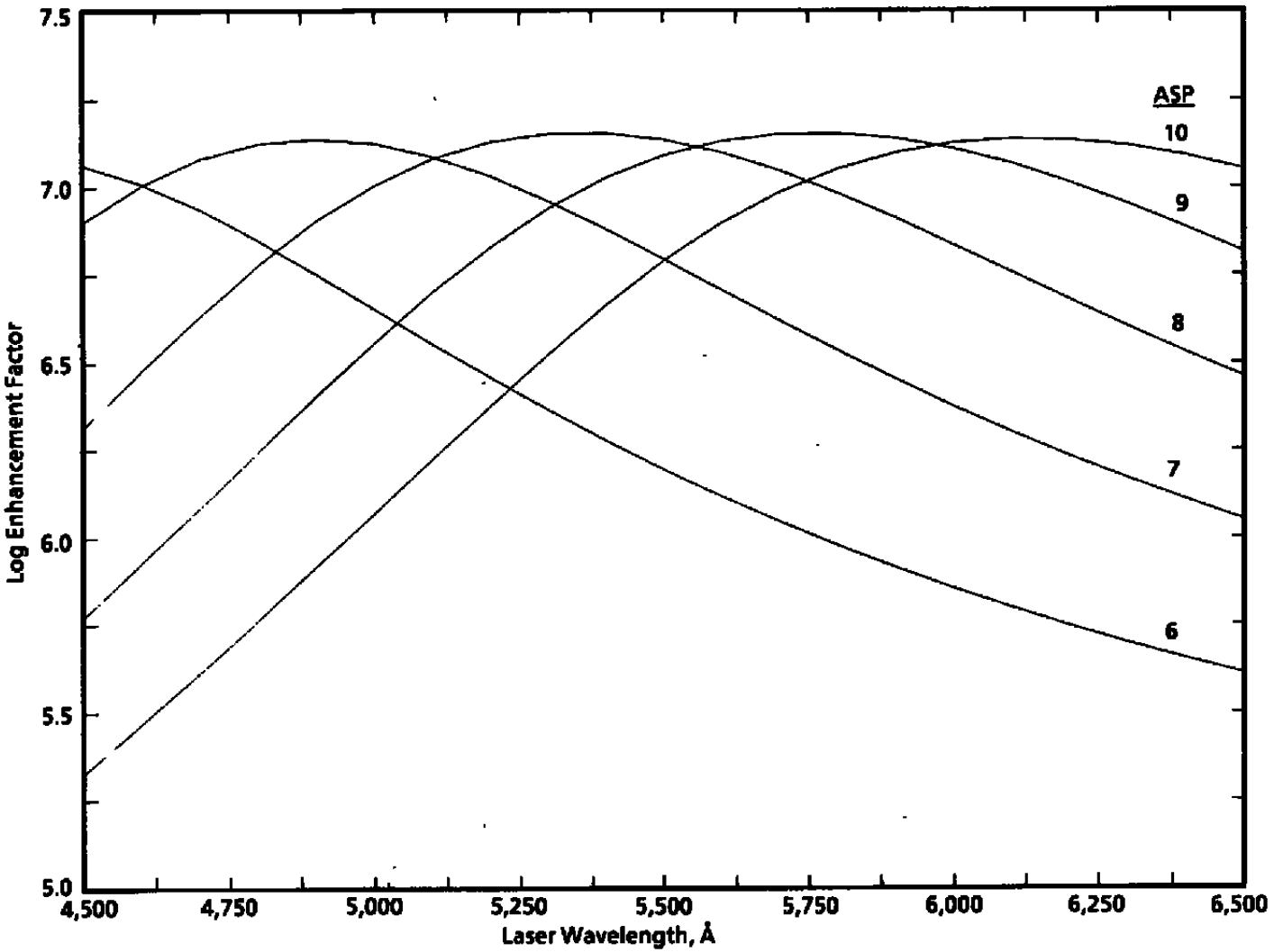

Figure 39. SERS EF for In hemi-spheroids, RS = 2,000 cm^{-1}, a = 600 Å, d = 3 Å.

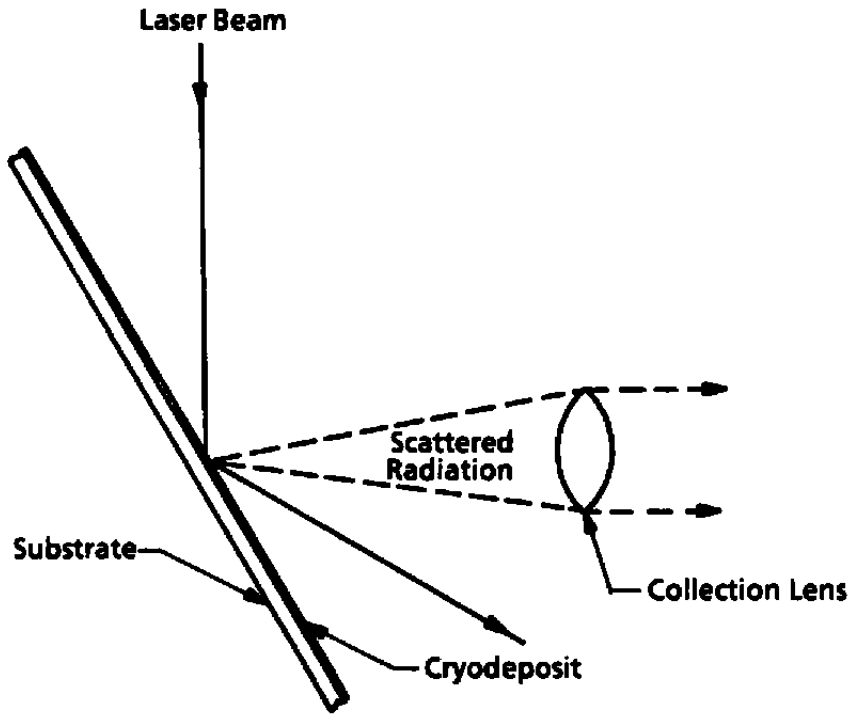

Figure 40. Assumed scattered geometry for calculation of normal Raman and SERS signal strength from cryodeposits.

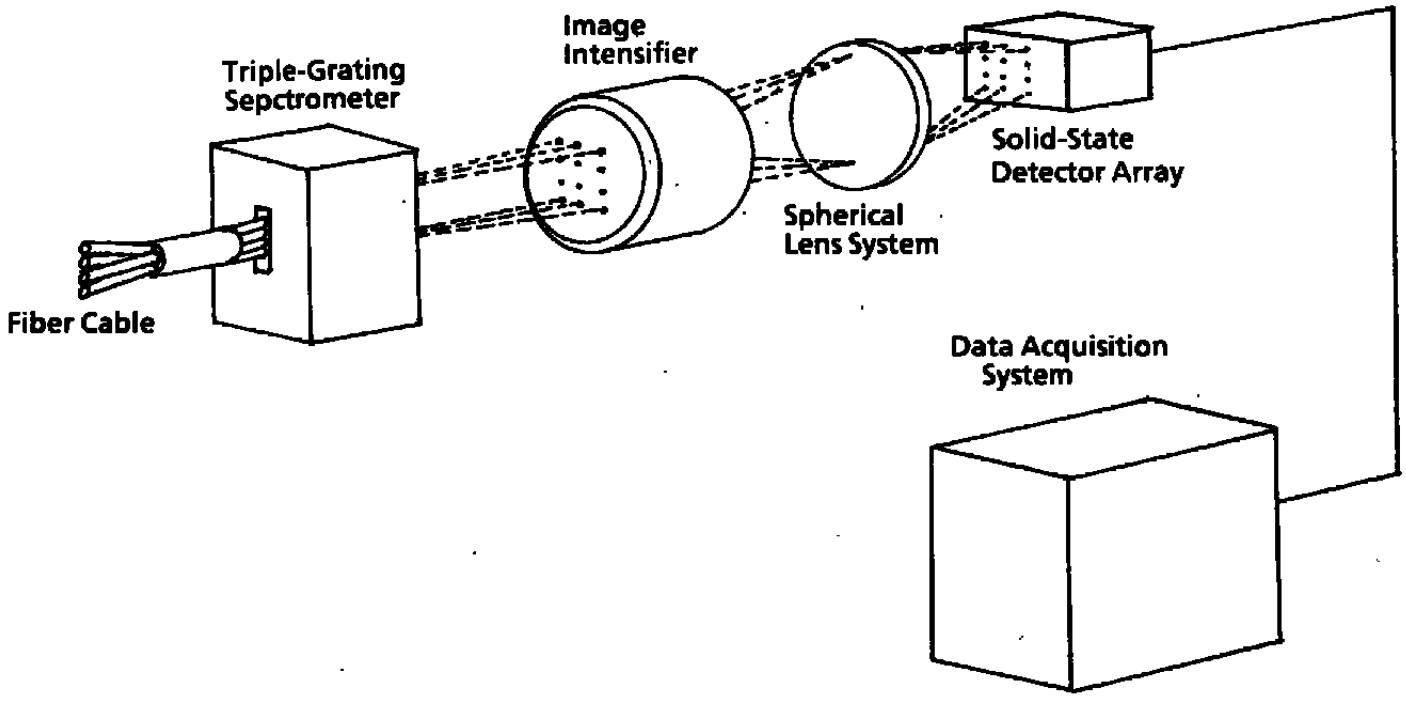

Figure 41. Laser microprobe detection system for AEDC chambers.

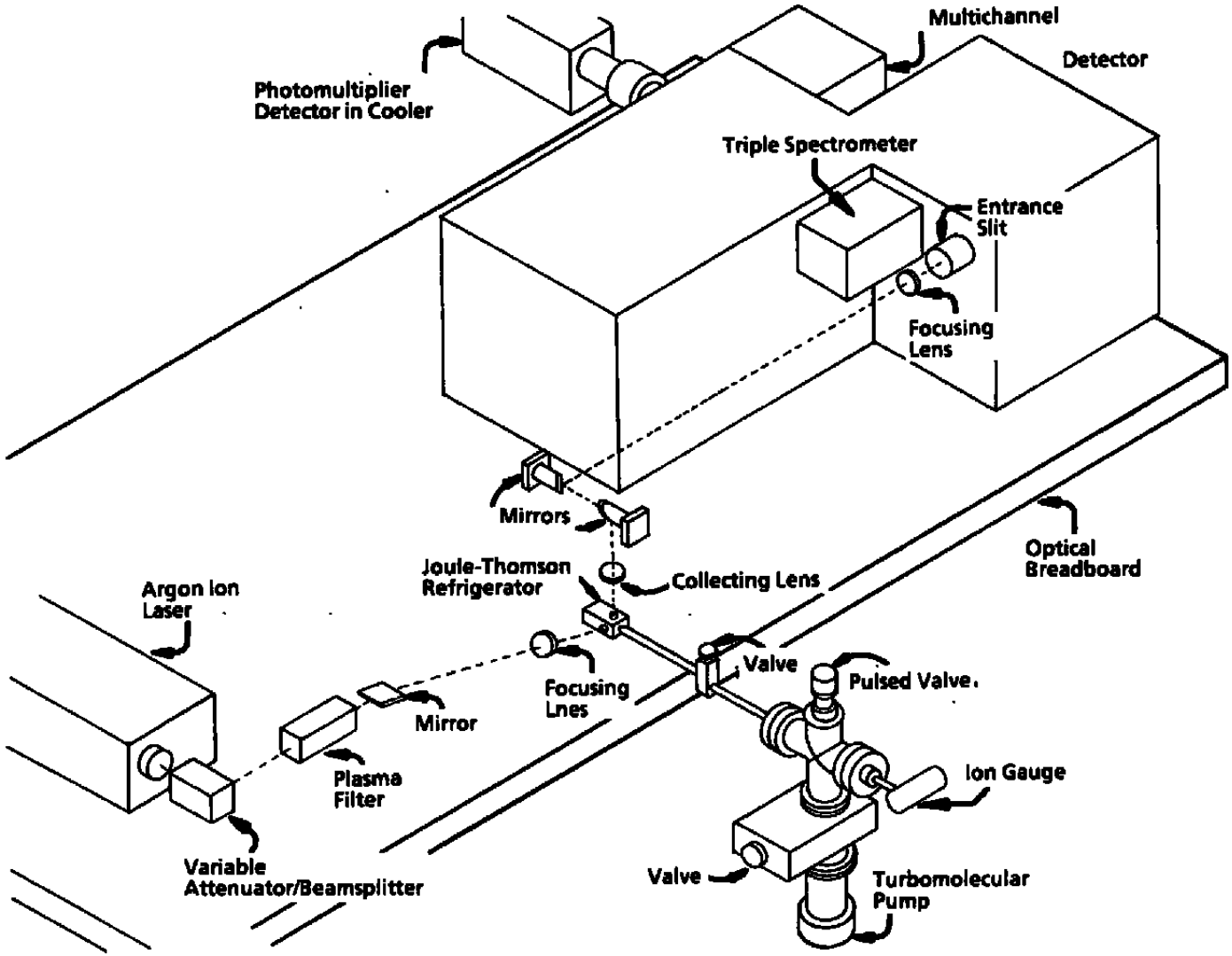

Figure 42. Laser microprobe development experimental configuration.

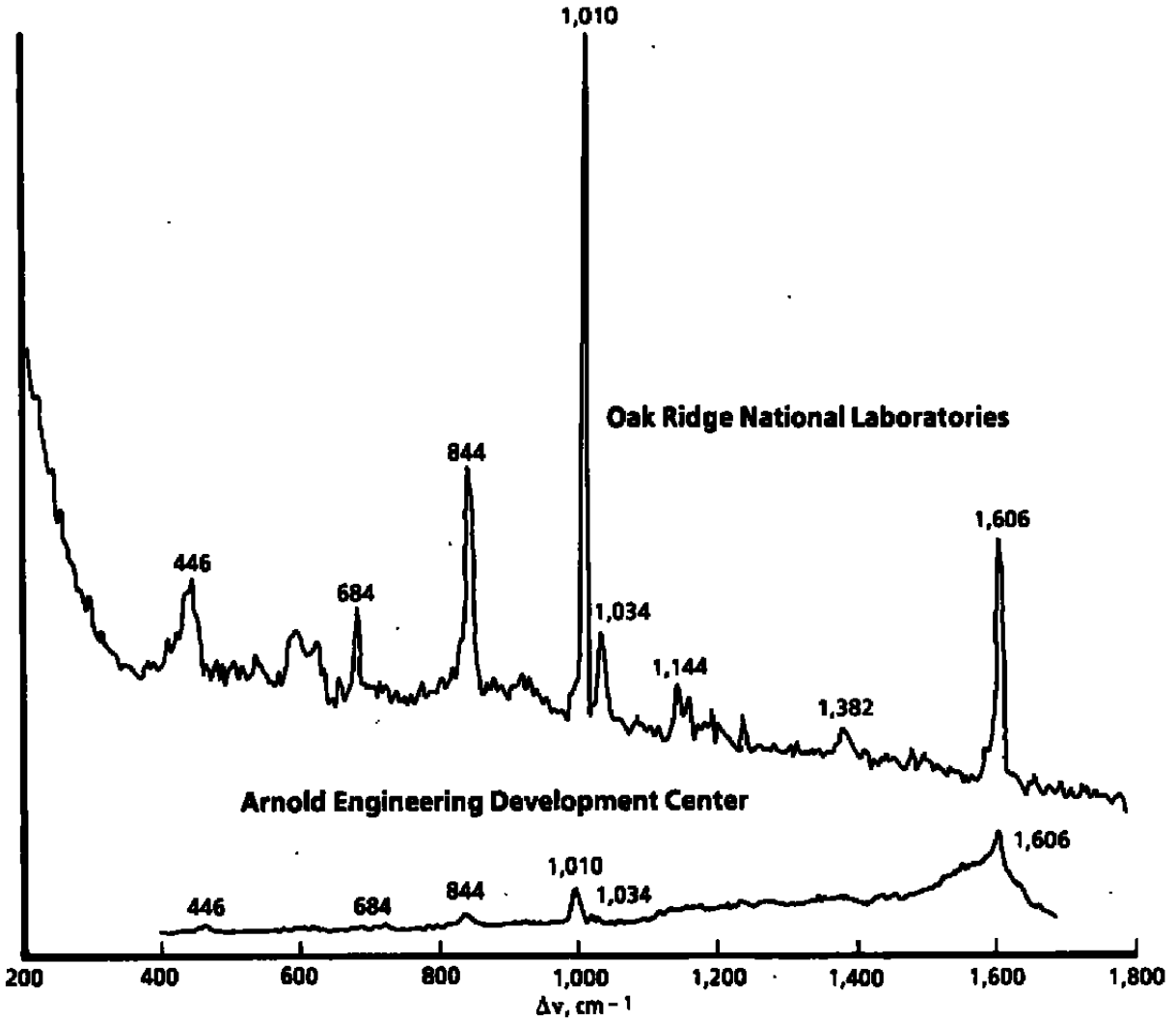

Figure 43. SERS spectra of benzoic acid recorded at Oak Ridge National Laboratory (ORNL) and AEDC.

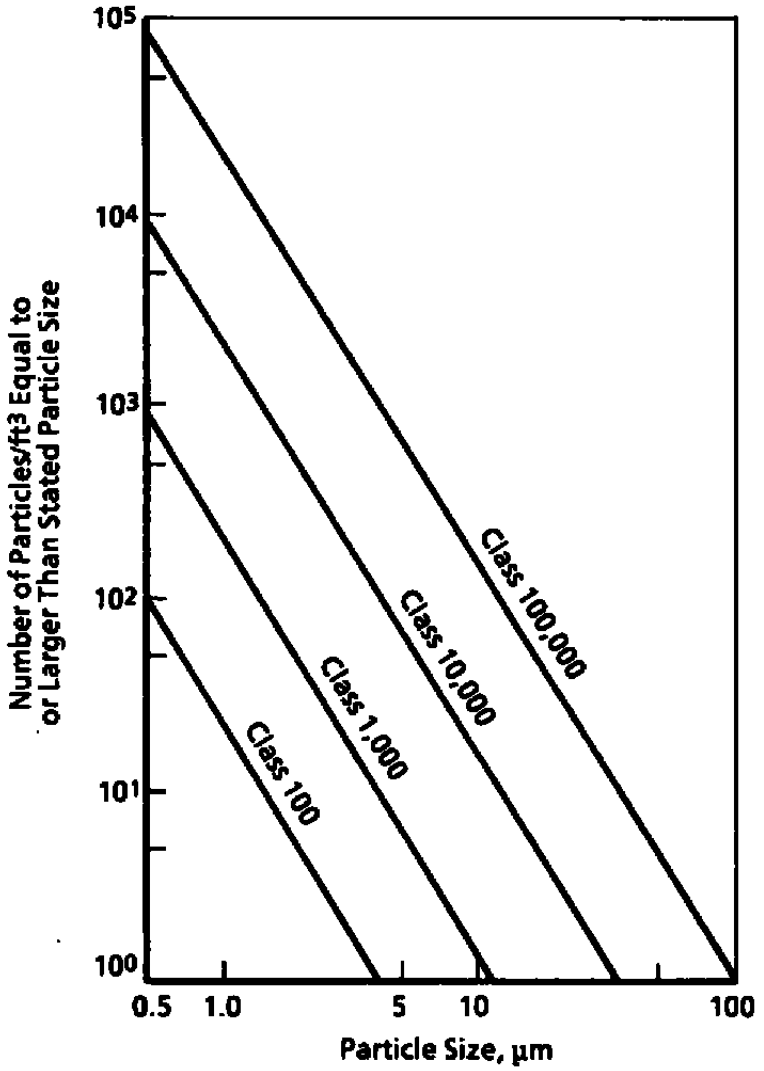

Figure 44. Federal Standard 209B particle size distribution.

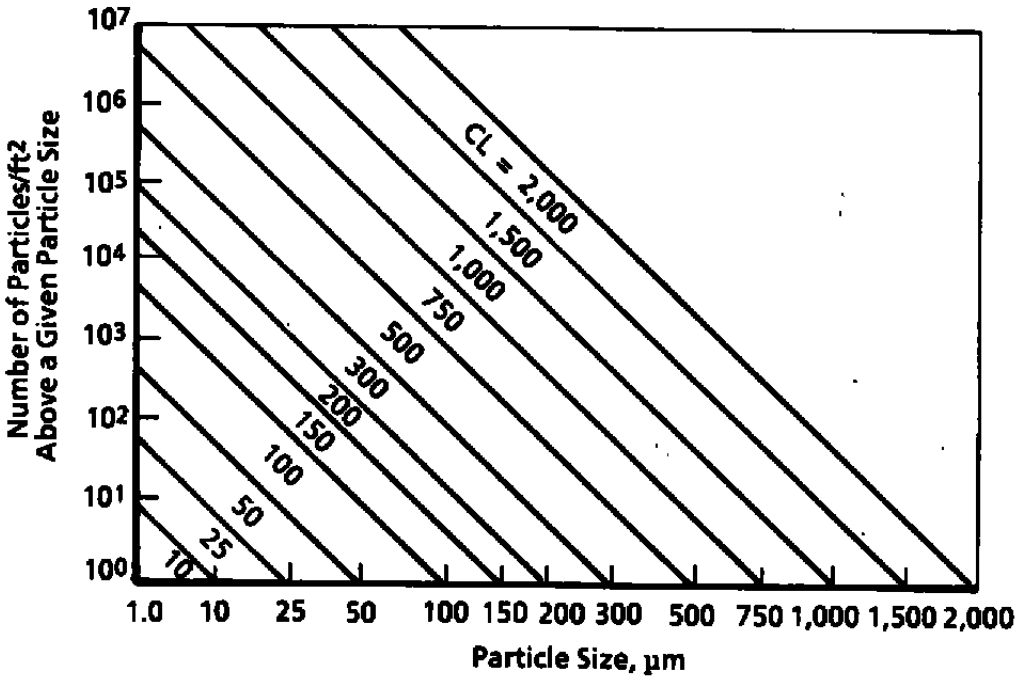

Figure 45. MIL-STD-1246A surface cleanliness levels.

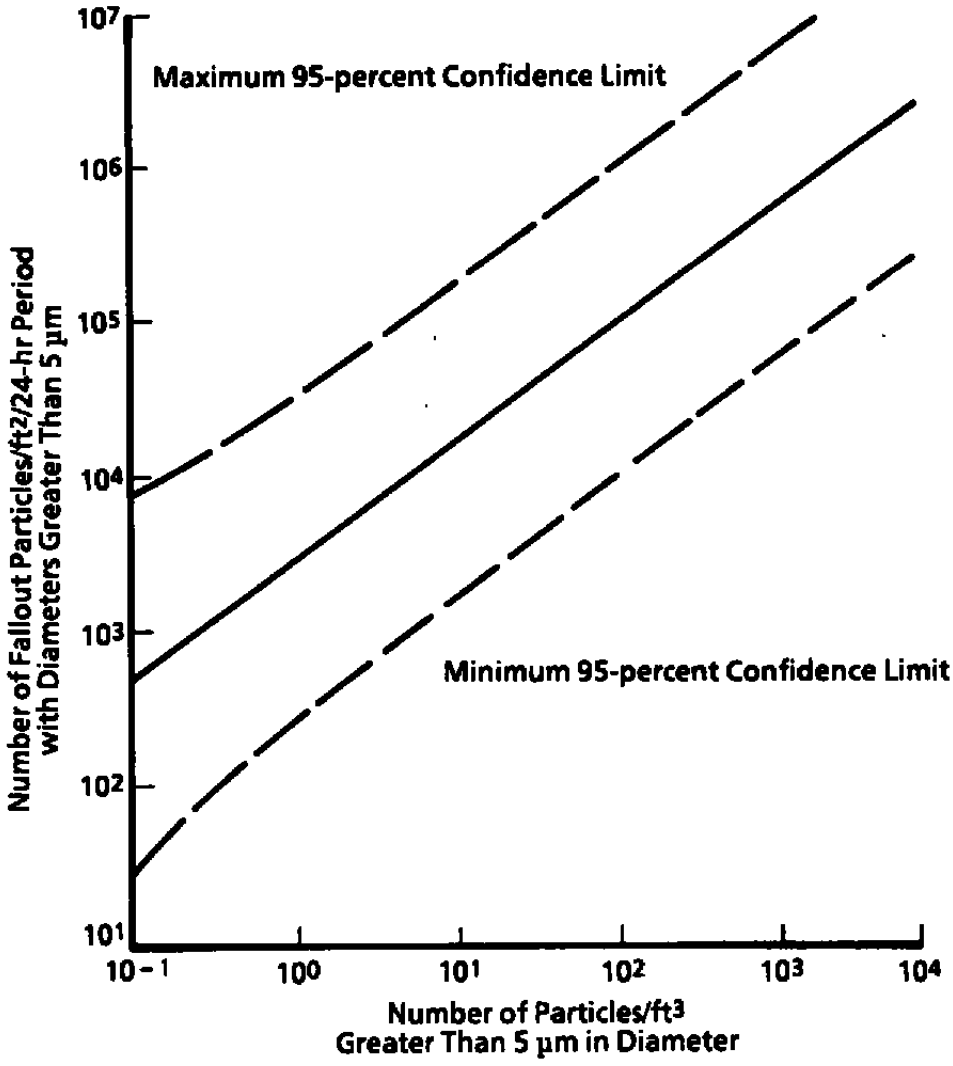

Figure 46. Hamberg model of particle fallout rates.

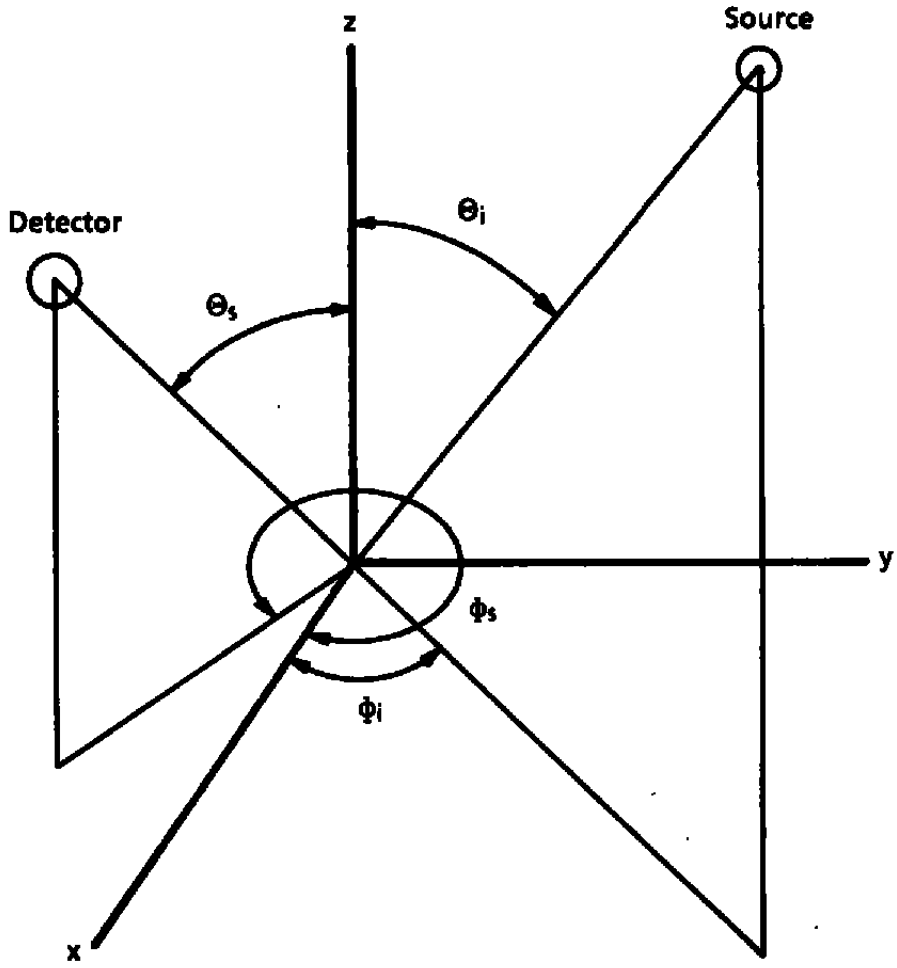

Figure 47. Coordinate geometry for BRDF.

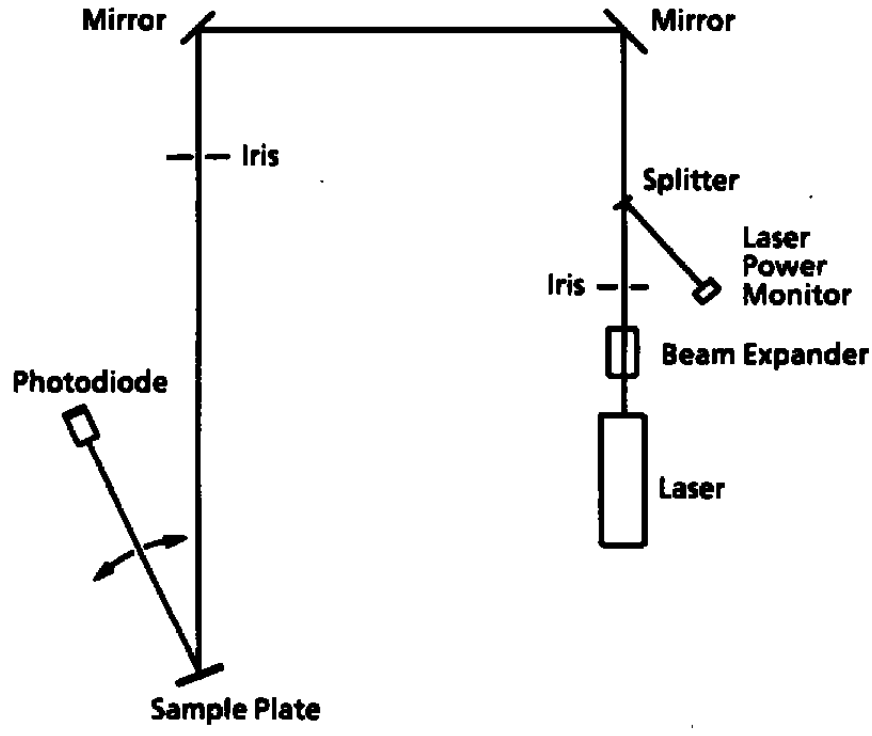

Figure 48. NASA Goddard Space Flight Center (GSFC) optical configuration for BRDF measurements.

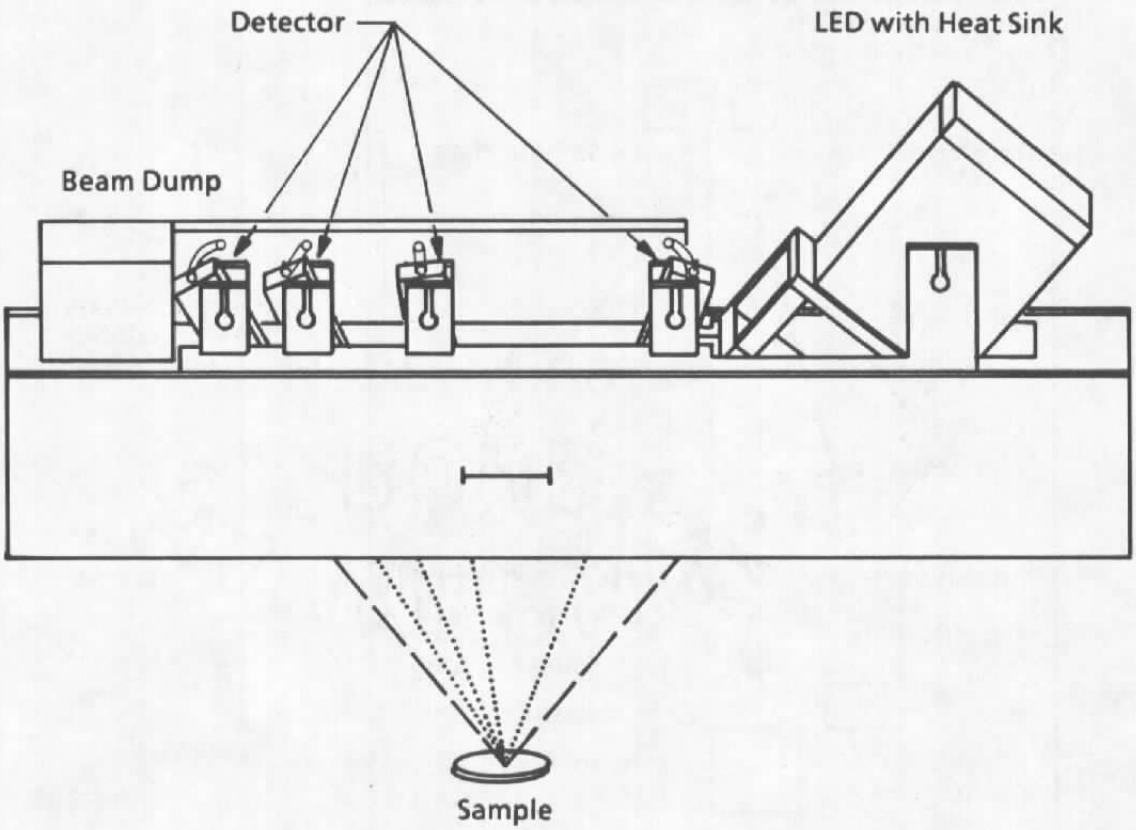

Figure 49. Preliminary sketch of the University of Arizona Optical Sciences Center (OSC) MICROSCAT.

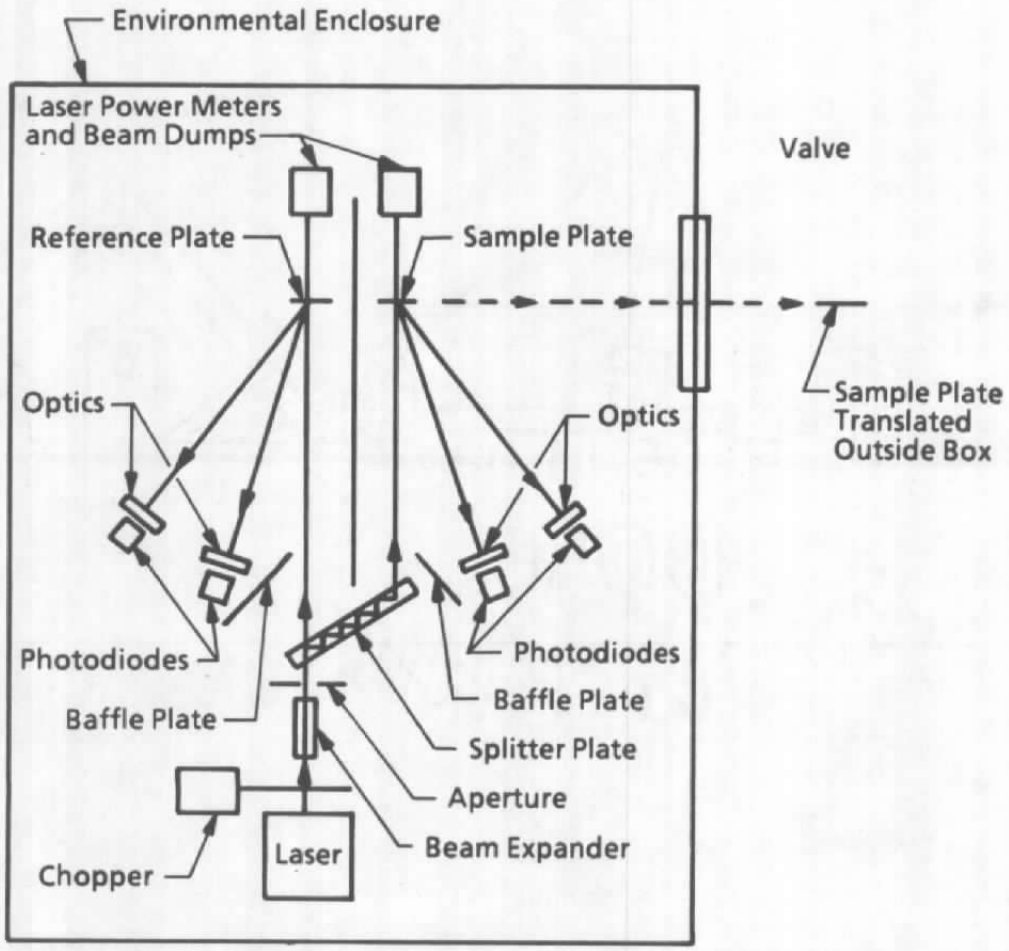

Figure 50. Initial concept for AEDC BRDF particulate instrument.

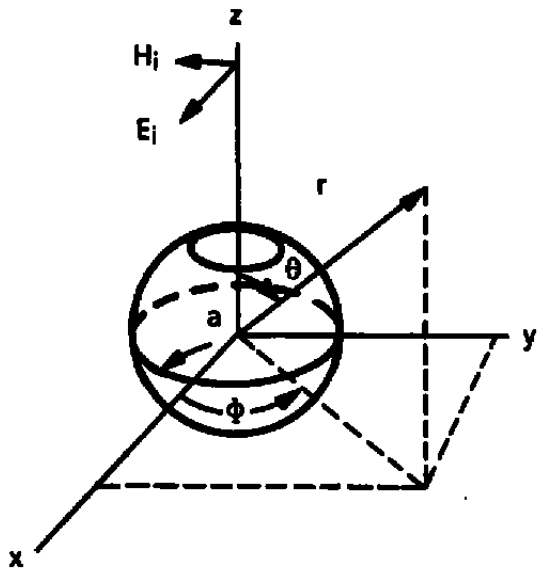

Note:
1. a Is the Radius of the Scattering Particle.
2. r Is the Radial Distance from the Particle to the Point of Observation.
3. The Incident Ray Travels Along the Positive Z Axis with Its Electric Vector Polarized Along the X Axis.

Figure 51. Geometry for particle scattering.

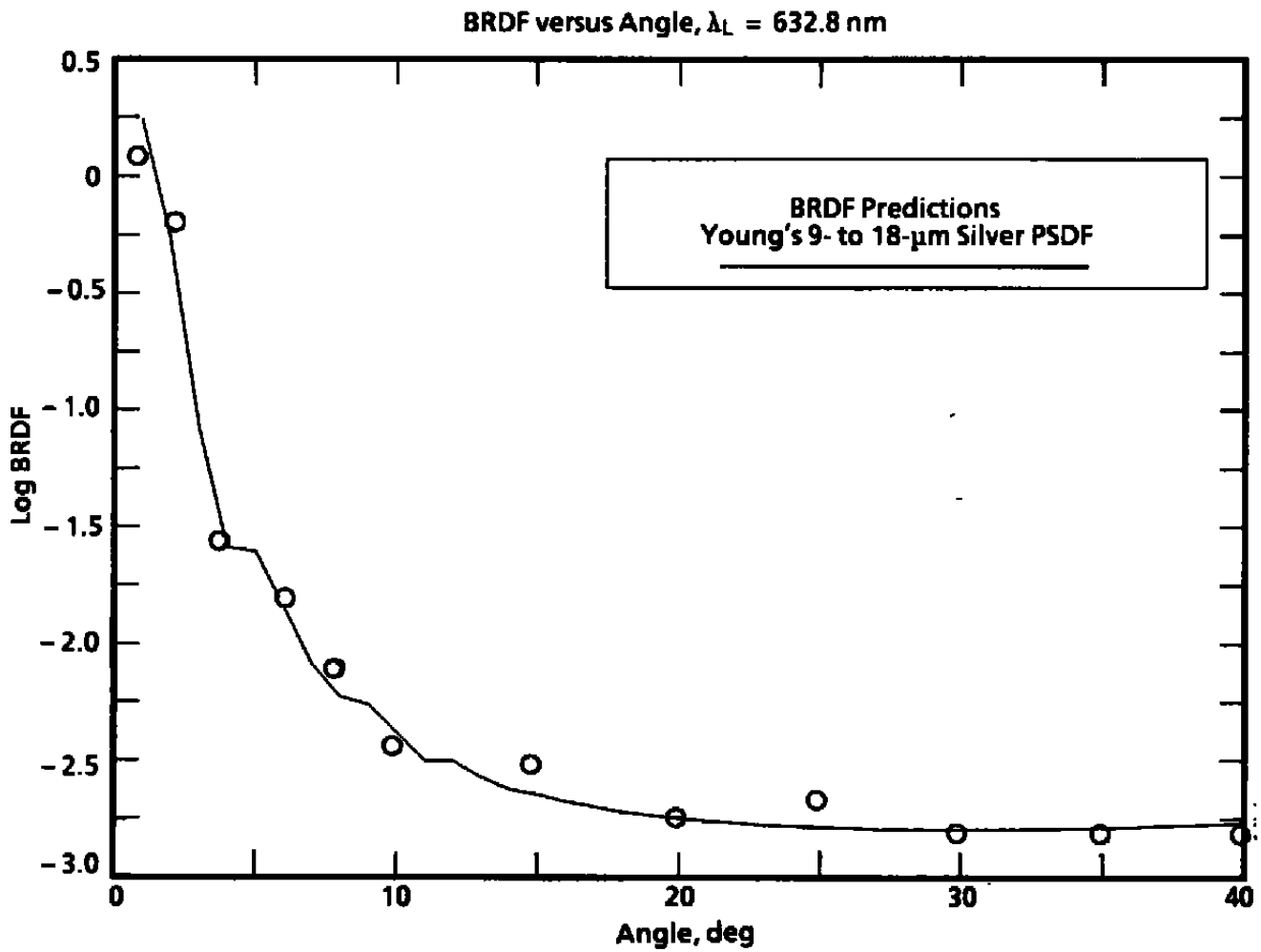

Figure 52. Comparison of code PBRDF predictions to Young's 9- to 18-μm silver measurements.

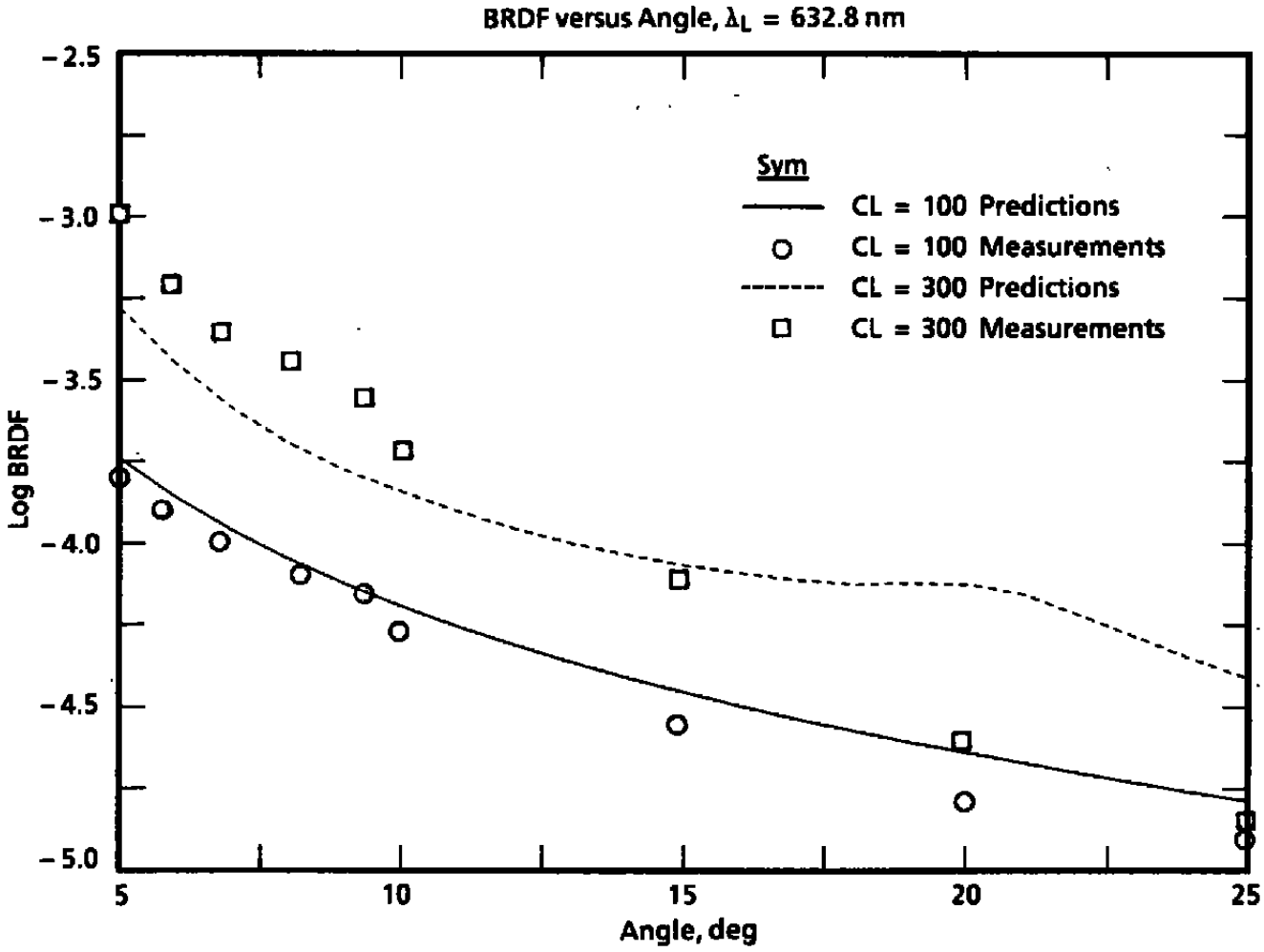

Figure 53. Comparison of code PBRDF predictions to NASA GSFC measurements on laboratory dust-contaminated sample plates.

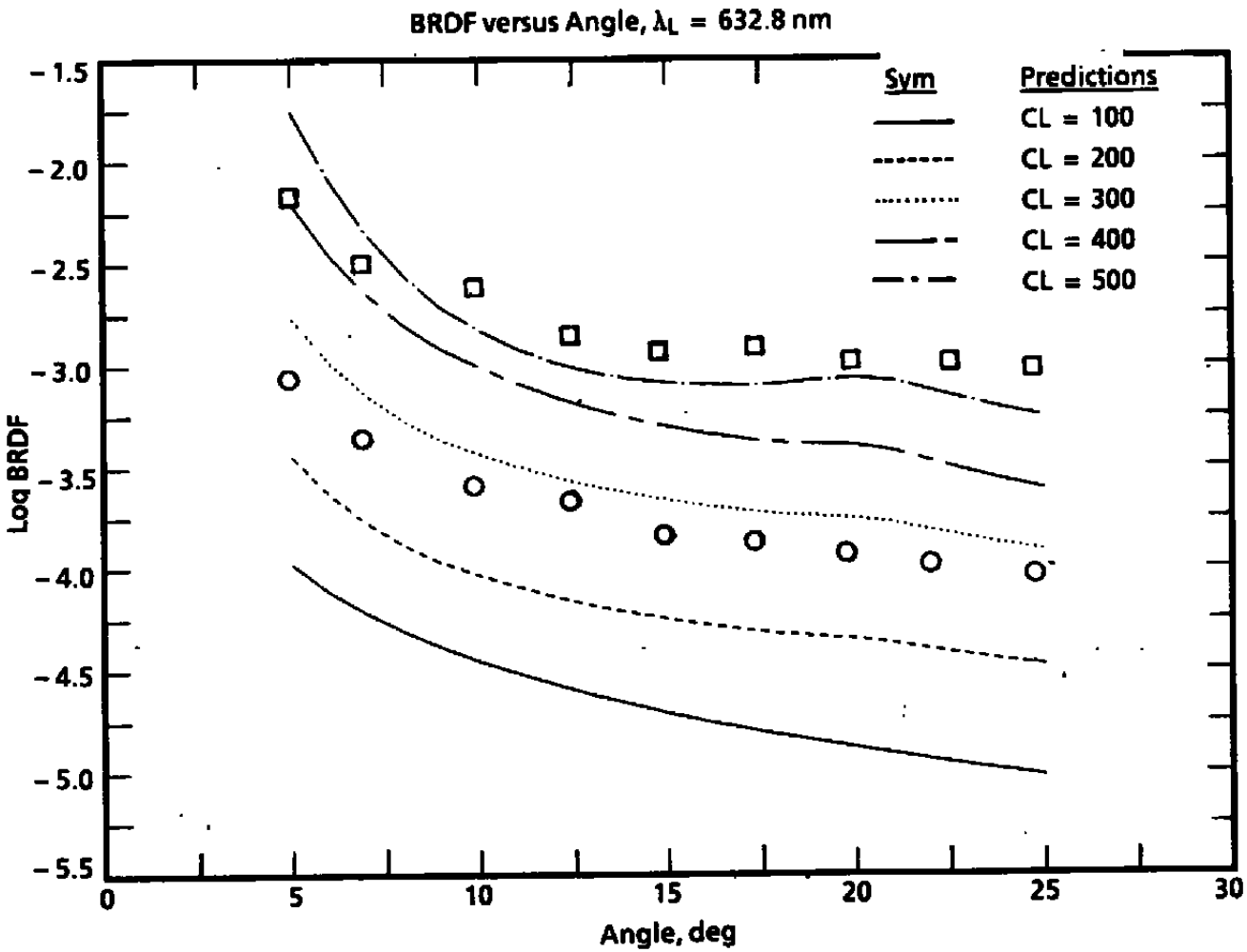

Figure 54. Comparison of code PBRDF predictions to Westinghouse measurements of laboratory dust-contaminated sample plates.

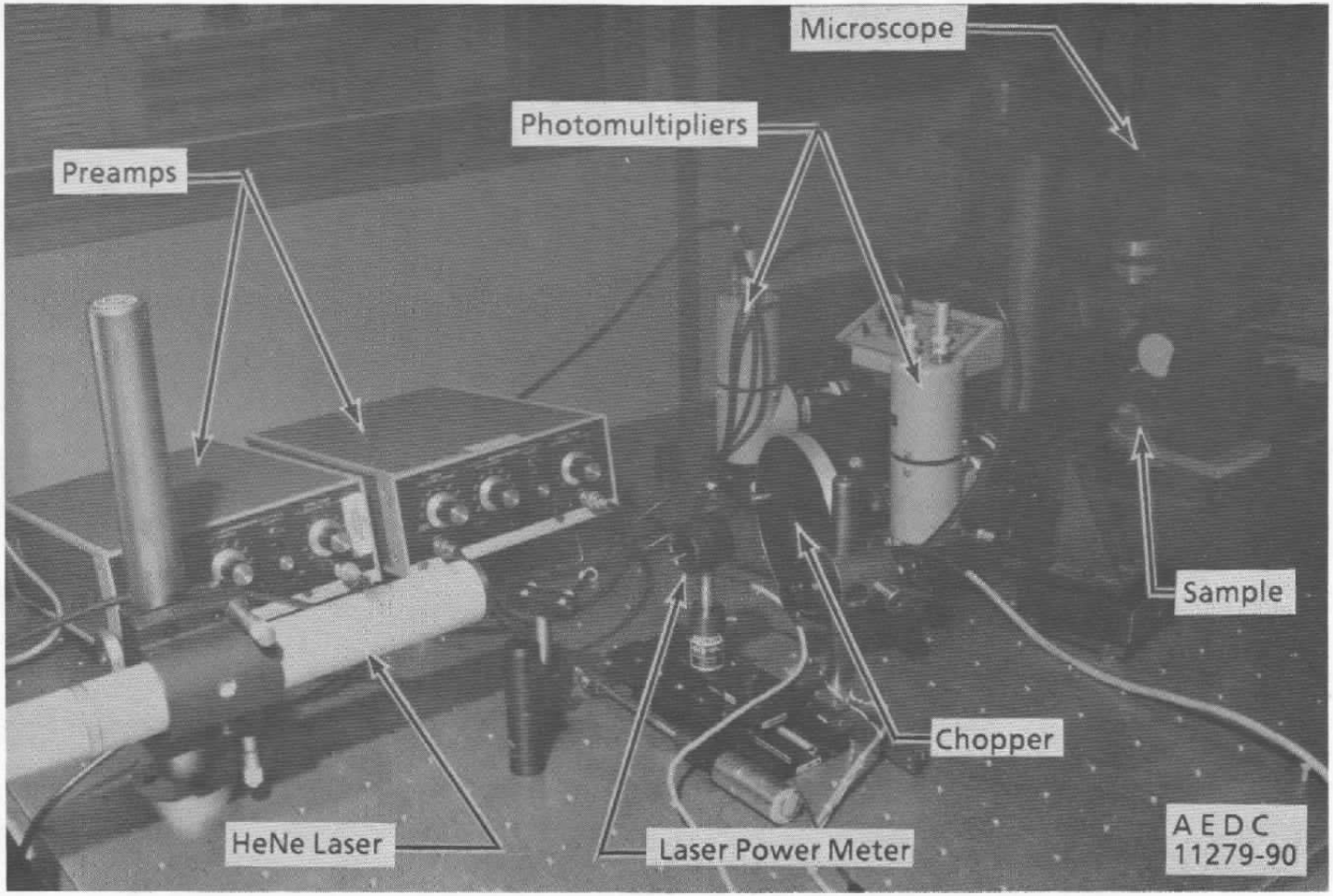

Figure 55. AEDC BRDF particle monitor prototype.

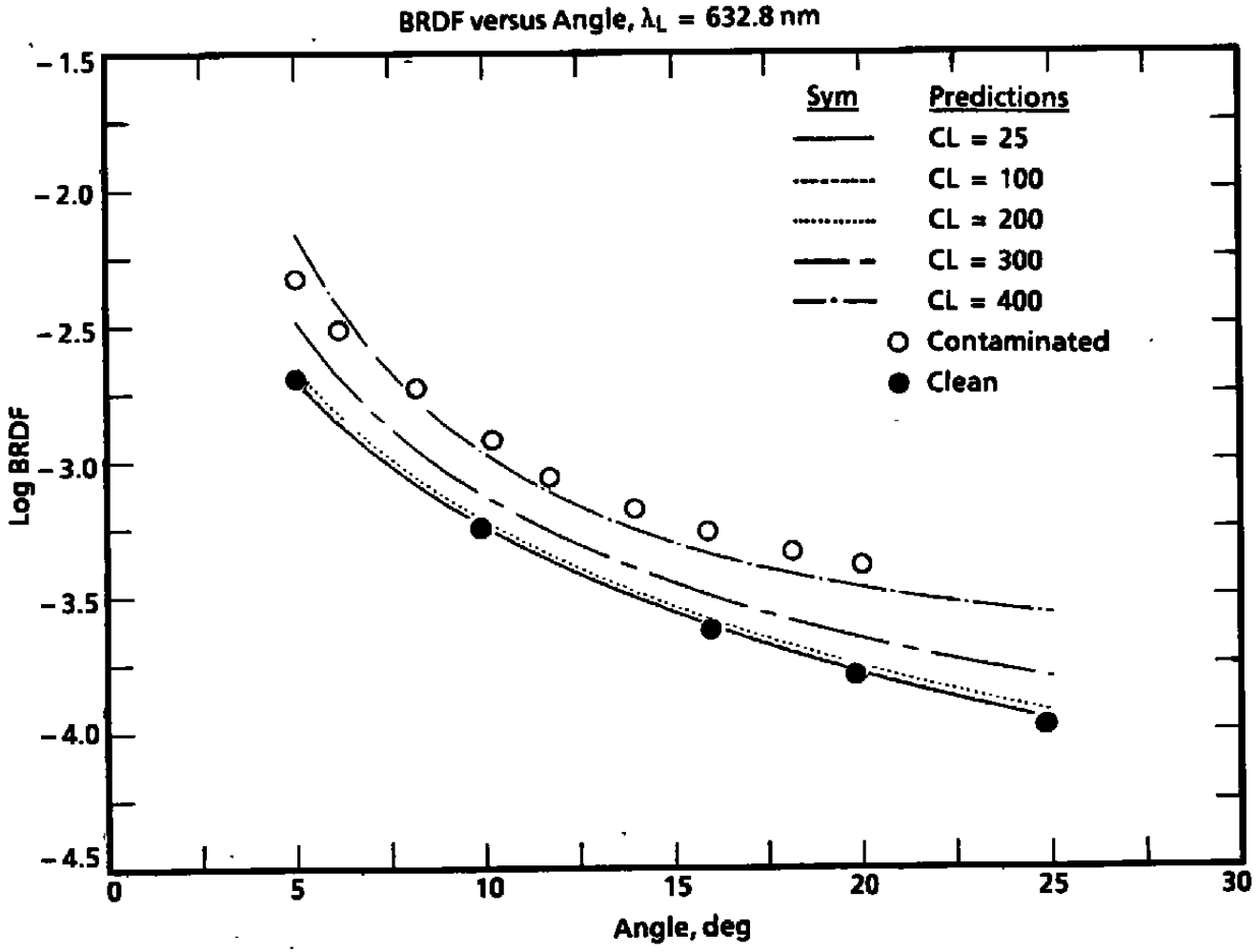

Figure 56. Comparison of code PBRDF predictions to AEDC measurements of MK-I cleanroom dust-contaminated Pyrex® mirror.

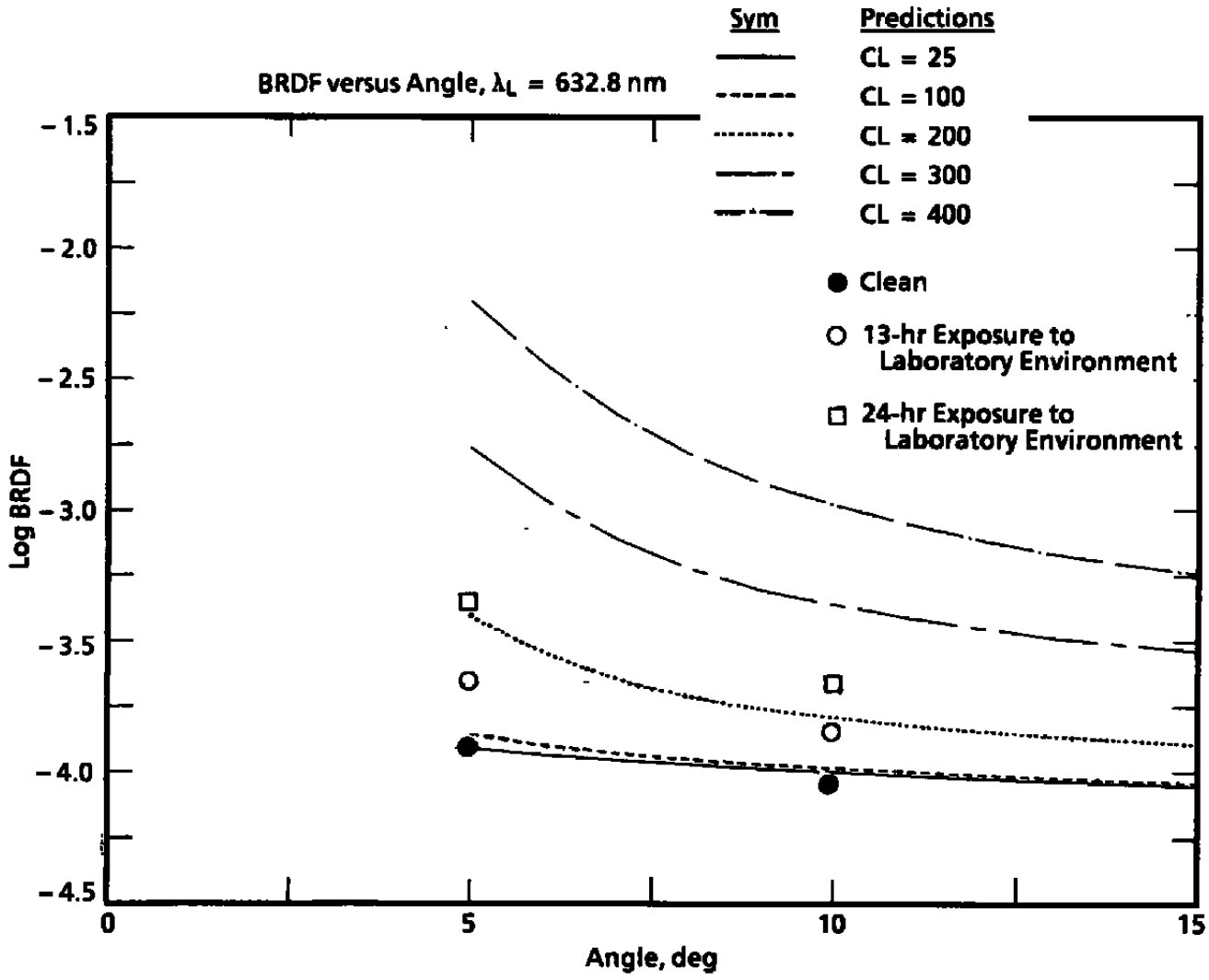

Figure 57. Comparison of code PBRDF predictions to AEDC measurements of laboratory dust-contaminated mirror sample plate.

Table 1. Initial AEDC Chamber Materials List

1. **Lubricants/Oils/Waxes**

   Dow Corning Vacuum Grease
   Apiezon Q Wax
   Braycote 600

2. **Adhesives**

   Dubois Duhesive 300
   DC6 - 1104
   RTV 560

3. **Adhesive Tapes**

   Aluminum — Stock Item

4. **Paints**

   Desota® Flat Black
   Bostik® Flat Black

5. **Epoxy®**

   Double Bubble® — Stock Item

6. **Aluminized Mylar®**

7. **Shrinkable Tubing**

8. **Indium**

APPENDIX A

CHAMBER MATERIALS DATABASE

A-1.0 DATABASE CONTENT

As noted in Section 4.3, the Chamber Materials Database (CMDB) should maintain contamination-related information. With this in mind, it was designed to store only certain material properties such as density, melting temperature, vapor pressure, collected volatile condensable materials (CVCM), total mass loss (TML), refractive index, and various types of spectra.

A-1.1 DESCRIPTIVE INFORMATION

Certain descriptive information must be maintained in the database to make it complete. Each material must be identified by storing its name, manufacturer, batch number, category, and an identification number used in correlating the different data properties with the material. This collection of information is called the material descriptor.

A unique material descriptor must be stored for each material before any information can be stored in the database for that material. During the storage of this descriptor, the identifier number will be assigned by the system, and all future references to this material must include this number. The number is stored in each property relation to tie each property value back to the specific material. This technique affords flexibility and saves storage by not consuming any storage for a material property until that information is entered into the database.

Each manufacturer is also allotted a descriptor and a unique number to identify it. Each material descriptor contains a manufacturer number that refers to a unique manufacturer descriptor. Therefore, before a material descriptor may be stored, the manufacturer descriptor may contain addresses, telephone numbers, names, or any other pertinent information, because the storage of the descriptor is in a free form that follows no rigid format requirement. The descriptor method of identifying manufacturers saves storage space, because a single manufacturer may have produced several of the materials in the database.

Each material category is specified in a descriptor form that contains the name of the category and a unique identification number. Each material descriptor stores the category identification number to designate its category. This method saves storage space by replacing the category name by a much smaller identifier and not storing the entire name of the category with each material descriptor. A category relation maintains these names and numbers to allow the user easy access to the category information.

Each item of information entered into the database must be tagged with the source of the data. Therefore, a reference relation is used to store all data sources. Each reference descriptor contains the reference or source information in free form and a unique reference identification number that is used to link each data item to its reference. When the user is entering the data item, he must specify a reference number to store with that item. If the reference is not already in the database, it may be easily added before attempting to store the data or may be entered during the data item entry procedure.

Each item of information must also be tagged with the units in which the data values are expressed. Therefore, a units relation is used to store all data units. Each units descriptor contains the units and a unique units identification number that is used to link each data item to its units. When the user is entering the data item, he must specify a units number to store with that item. If the units are not already in the database, they may be easily added before attempting to store the data or may be entered during the data item entry procedure. This method of units storage saves space by not storing the units name with each data item but stores a much smaller number that is converted into a units name at retrieval and display time.

The date is also maintained with each data item to give the user the time of the entry of that data into the database. The time and date are obtained from the computer system at the moment of storage.

A-1.2 DATABASE STRUCTURE

There are relations for each of the following:

1. materials descriptors,
2. manufacturers,
3. categories,
4. data units,
5. sources,
6. property types, and
7. each individual property.

The property types relation is maintained in the database for use by the database manager. This relation lists the content of all other relations and cannot be modified by the user because adding a property requires the addition of a new relation and new software to support it.

In addition to these relations, there are views that cross the information from various relations to give a full information packet for a material property. These views serve the

purpose of eliminating the identification numbers and replacing them with the corresponding descriptor data. Therefore, the data packet will contain only descriptive information for the selected property.

Each relation is given an index to allow speedy data retrieval. The material number is used as the index for all property relations and the materials descriptor relation. The unique identification number is used as index in the category, units, reference, and manufacturers relations. For the materials descriptor relation, the material name is also used as an index to allow speedy searches according to name. For the properties relation, the property name is used as a unique index.

Certain constraints are imposed upon the data before a successful storage can be accomplished. The following constraints are used:

1. A category and its identification number must be stored in the database before that number may be stored with a material descriptor.

2. The category identification number must be a unique number between 1 and 32,000.

3. A manufacturer and its identification number must be stored in the database before that number may be stored with a material descriptor.

4. The manufacturer identification number must be a unique number between 1 and 32,000.

5. A material descriptor and its identification number must be stored in the database before its identification number may be stored in a property data item.

6. The material identification number must be a unique number between 1 and 32,000.

7. The material name must be stored in capital letters as a standard to allow correct search processes.

8. A units descriptor and its identification number must be stored in the database before its identification number may be stored in a property data item.

9. The units identification number must be a unique number between 1 and 32,000.

10. A reference descriptor and its identification number must be stored in the database before its identification number may be stored in a property data item.

11. The reference indicator number must be a unique number between 1 and 32,000.

12. Single-valued data items such as density are allowed to have only one value stored in the database for a particular material.

13. The user cannot enter a property descriptor into the database. That procedure is the responsibility of the database manager.

A-1.3 DATA STRUCTURES

Data structures for storing each item of information must be defined in the database to let the database know how to handle each item. The structures used in the CMDB includes SIGNED WORD, VARYING STRING, DATE, F____FLOATING, and SEGMENTED STRING.

Identification numbers are specified as SIGNED WORD, which corresponds to FORTRAN data type INTEGER*2.

Single-valued property data are specified as F____FLOATING, which corresponds to FORTRAN REAL*4. The CMDB single-valued properties are density at STP, melting temperature at 1 atm, TML, and CVCM.

VARYING STRING, which corresponds to CHARACTER**data type, with various maximum sizes is used for such items as material name, batch number, units name, property name, and material category name.

DATE, of course, must be used for date storage. It has no set FORTRAN data type but can be manipulated through data type INTEGER*4.

SEGMENTED STRING is used for storing manufacturer descriptors, references/sources, an all spectral/graphical data. The following properties are maintained as spectra or graphs in the CMDB:

1. vapor pressure,
2. gas chromatograms,
3. mass spectra,
4. IR ATR plate spectra,
5. real refractive index,
6. imaginary refractive index,
7. reflectivity,
8. transmissivity, and
9. solar absorptance.

Lists of chemical genealogy and outgassing species are also maintained in SEGMENTED STRINGS in the CMDB.

The SEGMENTED STRING data type has no set FORTRAN data structure that corresponds to it and can be used to store unstructured data. Therefore, strings, arrays, graphs, etc., can be stored in this free form of storage. The database stores the data in this form and leaves the actual manipulation of the information in this data structure to the database designer. This makes it easy to store an array of spectral data whose size may vary and is unknown at database definition time.

A-2.0 DATABASE INITIALIZATION

The database was initalized by first defining the structure in a command file called CHAMBER___MATERIALS.RDO. All field, relation, constraint, index, and view definitions were included in this file. This command file was then invoked from the "RDO>" prompt, and the database was thereby defined and structured automatically to yield the CHAMBER___MATERIALS.RDB and CHAMBER___MATERIALS.SNP files. The ".RDB" file contains the database definitions and all data. The ".SNP" file is used in database manipulation for temporary storage.

The command file also initialized certain relations to contain a starter set of data. The category relation was initialized with the following:

1. ADHESIVES,
2. ADHESIVE TAPES,
3. CERAMICS,
4. COMPOSITES,
5. COOLANTS,
6. ELASTOMERS,
7. ELECTRICAL/ELECTRONIC HARDWARE,

8. EPOXIES,
9. FERROUS METALS,
10. FILMS,
11. FOAMS,
12. FUELS,
13. GASES,
14. GLASSES,
15. GREASES,
16. INSULATIONS,
17. LIQUIDS,
18. LUBRICANTS,
19. NONFERROUS METALS,
20. OILS,
21. PAINTS/SURFACE COATINGS,
22. PLASTICS,
23. POTTING COMPOUNDS,
24. REFRACTORIES,
25. RUBBERS,
26. SOLIDS, and
27. WAXES.

The numbers given in this list also correspond to the identification numbers used to designate each category.

The properties relation was initialized with the following properties:

1. MATERIAL NAME,
2. MANUFACTURER,
3. CHEMICAL GENEALOGY,
4. BATCH NUMBER,
5. DENSITY,
6. VAPOR PRESSURE DATA,
7. MELTING TEMPERATURE,
8. GAS CHROMATOGRAPH SPECTRUM,
9. MASS SPECTRUM,
10. IR ATR PLATE SPECTRUM,
11. REAL REFRACTIVE INDEX,
12. IMAGINARY REFRACTIVE INDEX,
13. REFLECTIVITY,
14. TRANSMISSIVITY,

15. TOTAL MASS LOSS,
16. COLLECTED VOL. CONDENS. MATLS,
17. OUTGASSING SPECIES, and
18. SOLAR ABSORPTANCE.

The data units relation was initialized with the following:

1. (unitless designator),
2. % (percentage),
3. deg K (Kelvins),
4. deg C (degrees Centigrade),
5. deg R (degrees Rankine),
6. deg F (degrees Fahrenheit),
7. μsec (microseconds),
8. msec (milliseconds),
9. sec (seconds),
10. min (minutes),
11. hr (hours),
12. nm (nanometers),
13. microns,
14. mm (millimeters),
15. cm (centimeters),
16. m (meters),
17. cm^{-1} (per centimeter),
18. gm cm^{-1} (grams per cubic centimeter),
19. torr, and
20. amu (atomic mass units).

The numbers used in this list also correspond to the identification numbers used to designate the units.

The manufacturer relation was initialized with the "UNKNOWN" descriptor that was given the identification number 1. The reference/source relation was also initialized with the "UNKNOWN" descriptor with identifier of 1. The material descriptor relation was left empty during initialization.

A-3.0 DATABASE QUERIES

The CMDB database can be used to store and retrieve data by using the program CHAMBER___MATERIALS.EXE mentioned in Section 1.0. This program displays a series

of menus and for each one expects the user to select a processing option by number. Each option either passes the user to another menu or to a data manipulation procedure.

The program first displays the root menu as follows:

Root menu:

1. STORE DATA
2. RETRIEVE DATA
3. QUIT

Select option by number:

Option 1 sends the user to the data storage process and Option 2 sends the user to the data retrieval process. Option 3 ends processing by exiting.

A-3.1 DATA STORAGE

Selection of the data storage option in the root menu prompts display of the following menu:

List of store options:

1. material descriptor,
2. reference or source,
3. manufacturer name and address,
4. units,
5. category,
6. specific property, and
7. quit.

Select option by number:

Selection of Option 7 causes the program to terminate storage processing and to return to the root menu.

A-3.2 STORAGE OF A MATERIAL DESCRIPTOR

When Option 1 of the store options menu is selected, the program begins by asking questions to determine whether or not the material descriptor desired is in the database or

if it needs to be added to the database. The user is given the option of looking at all descriptors to determine that the needed one is not present. If it is not present, the system can assign a material number to be used for the new descriptor. If the material is present already, the system stops the descriptor storage procedure.

Next the system asks for the manufacturer number and will, if needed, list all manufacturers in the database to allow the user to extract the correct number. If the manufacturer does not have a descriptor in the database, the user is taken back to the store options menu from which he may execute the manufacturer descriptor storage procedure described in Section 4.1.3.

Given that the manufacturer descriptor was already in the database, the system then asks for the category number and will, if needed, list all categories in the database to allow the user to extract the correct number. If the category does not have a descriptor in the database, the user is taken back to the store options menu from which he may execute the category descriptor storage procedure described in Section 4.1.5.

Given that the category descriptor was already in the database, the user is then requested to input the material name and batch number by filling in the blanks of the following query messages:

Material:

_____

_____

Batch number:

_____

_____

The material name should be input in capital letters, and to ensure that the name is stored in capitals, all lowercase letters are automatically converted to capitals. This is done to allow a standard search on material name. The batch number may be any combination of printing ASCII characters.

Once all the information for the material under consideration has been entered, the user may proceed to store the descriptor in the database. If an error has been committed in the entry, the user may choose to input the data again before storage. The material descriptor storage procedure may be terminated without storing anything in the database if desired.

A-3.3 STORAGE OF A REFERENCE DESCRIPTOR

When Option 2 of the store options menu is selected, the program begins by asking questions to determine whether or not the reference descriptor desired is in the database or if it needs to be added to the database. The user is given the option of looking at all descriptors to determine that the needed one is not present. If it is not present, the system can assign a reference number to be used for a new descriptor. If the reference is present already, the system stops the descriptor storage procedure.

Next, the user is asked to input the reference descriptor information by filling in a series of blank lines. Any printing ASCII character may be used, and no fixed format of data entry is required as long as the user does not exceed the limits set forth by the blank lines. Data entry may be terminated before all blank lines are filled merely by hitting RETURN at the beginning of the current line. The program will check to determine that the user has entered information on at least one line and will terminate the procedure otherwise.

Given the proper entry of the reference information, the user may then proceed to store the reference descriptor, may go back and make changes, or may quit the procedure all together.

A-3.4 STORAGE OF A MANUFACTURER DESCRIPTOR

When Option 3 of the store options menu is selected, the program begins by asking questions to determine whether or not the manufacturer descriptor desired is in the database or if it needs to be added to the database. The user is given the option of looking at all descriptors to determine that the needed one is not present. If it is not present, the system can assign a manufacturer number to be used for a new descriptor. If the manufacturer is present already, the system stops the descriptor storage procedure.

Next the user is asked to input the manufacturer descriptor information by filling in a series of blank lines. Any printing ASCII character may be used, and no fixed format of data entry is required as long as the user does not exceed the limits set forth by the blank lines. Data entry may be terminated before all blank lines are filled merely by hitting RETURN at the beginning of the current line. The program will check to determine that the user has entered information on at least one line and will terminate the procedure otherwise.

Given the proper entry of the manufacturer information, the user may then proceed to store the manufacturer descriptor, may go back and correct any errors, or may quit the procedure all together.

A-3.5 STORAGE OF A UNITS DESCRIPTOR

When Option 4 of the store options menu is selected, the program begins by asking questions to determine whether or not the units descriptor desired is in the database or if it needs to be added to the database. The user is given the option of looking at all descriptors to determine that the needed one is not present. If it is not present, the system can assign a units number to be used for a new descriptor. If the units are present already, the system stops the descriptor storage procedure.

Next the user is asked to input the units descriptor information by filling in a blank line. Any printing ASCII character may be used, and no fixed format of data entry is required as long as the user does not exceed the limits set forth by the blank line.

Given the proper entry of the units information, the user may then proceed to store the units descriptor, may go back and make changes, or may quit the procedure all together.

A-3.6 STORAGE OF A CATEGORY DESCRIPTOR

When Option 5 of the store options menu is selected, the program begins by asking questions to determine whether or not the category descriptor desired is in the database or if it needs to be added to the database. The user is given the option of looking at all descriptors to determine that the needed one is not present. If it is not present, the system can assign a category number to be used for a new descriptor. If the category is present already, the system stops the descriptor storage procedure.

Next the user is asked to input the category descriptor information by filling in a blank line. Any printing ASCII character may be used, and no fixed format of data entry is required as long as the user does not exceed the limits set forth by the blank line. Any lowercase letters will be converted to capitals.

Given the proper entry of the category information, the user may then proceed to store the category descriptor, may go back and make changes, or may quit the procedure all together.

A-3.7 STORAGE OF DATA FOR A SPECIFIC PROPERTY

When Option 6 of the store options menu is selected, the program begins by asking questions to determine whether or not the material descriptor desired is in the database or if it needs to be added to the database. The user is given the option of looking at all descriptors to determine that the needed one is present. If the material is not present already, the system stops the property data storage procedure.

The following menu of properties is then printed to permit the user to select the property he needs to store:

List of properties for storage:

1. chemical genealogy,
2. density,
3. vapor pressure,
4. melting temperature,
5. gas chromatograph spectrum,
6. mass spectrum,
7. IR ATR plate spectrum,
8. real refractive index,
9. imaginary refractive index,
10. reflectivity,
11. transmissivity,
12. total mass loss,
13. CVCM,
14. outgassing species,
15. solar absorptance, and
16. quit.

Select option by number:

Selection of Option 16 takes the user back to the store options menu. The other options take the user through the property data input stream.

The property data input stream begins by inputting the number of the reference that gives the source of the data. A series of questions are asked as described in Section 4.1.2 to input the reference number and determine that the reference so input is in the database.

Once the reference has been input and verified, the units in which the data are expressed must be defined. This units input procedure follows the steps described in Section 4.1.4. If the option selected from the data I/O menu were 1 or 14, no units input is necessary, and the program skips this procedure. Options 2, 4, 12, and 13 require that a single set of units be defined. The remaining options require that units be defined for both the independent and dependent variables of these graphical/spectral data sets.

Then the procedure executes the data input process, the actual method of input depending upon the option selected. Selection of option 2, 4, 12, or 13 takes the user through a fill-in-

the-blanks procedure for inputting a single value for that property. Selection f option 1 or 14 takes the user through a fill-in-the-blanks list input procedure for entering specie names. Selection of any of the other options takes the user through a menu-driven procedure for inputting the data that are described in Section 4.1.6.1.

Given the proper entry of the property data packet, be it for single valued, list, or graphical/spectral data, the user may then proceed to store that data in the database, may go back and make changes, or may quit the procedure all together. After storage attempts, a message will be displayed to indicate whether or not the storage was successful. Any unsuccessful attempts will have no effect on the database and must be retried, possibly requiring that the previous inputs be modified to conform to the database constraints.

A-3.8 DATA SET INPUT PROCEDURE

The data set input procedure was designed for inputting graphical or spectral data sets and operates by first displaying the following menu:

List of data I/O operations:

1. input through keyboard,
2. input from file,
3. allow examination and modification of current data set,
4. store current data set to file,
5. return to calling procedure with current data set, and
6. quit after deleting current data set.

Select option by number:

This procedure allows the user to input via keyboard, from a file, operate on a previously input data set, or to store the data into a new file. File names are supplied by the user at the time of the data transfer. The format of external data files read from or written to is described in Section 4.1.6.11.

Option 5 returns the user to the property data input stream while maintaining the data set just input. Option 6 erases the data set before existing and in essence kills the current property storage procedure.

Option 3 of the I/O menu allows the user to further examine or process the data set. This subprocedure displays the following menu:

List of data display/correction operations:

1. print current data set to terminal,
2. correct individual point in data set,
3. window operations (view, insert, delete),
4. sort in ascending order,
5. sort in descending order, and
6. quit.

Select option by number:

Selection of Option 6 takes the user back to the data I/O procedure. Options 1, 2, 4 and 5 are self-explanatory.

Option 3 of the display/correction menu causes display of the following menu:

List of data window operations:

1. define window range,
2. view contents of window,
3. insert into data set before beginning of window,
4. insert into window at end,
5. delete data in window, and
6. quit.

Select option by number:

Selection of Option 6 takes the user back to the data display/correction procedure. Option 1 defines the range of a certain portion of the data set for window operations. Option 2 merely displays the content of the defined window. Option 3 allows the user to insert data into the data set immediately ahead of the window. Option 4 allows insertion into the window at its end. Option 5 will permit deletion of the window content.

Data point insertion is performed one point at a time through the keyboard. The user is queried at each step of the procedure for the expected input. These queries provide flexibility to correct input errors, store the points, and terminate the procedure. The number of points in the data set is automatically updated for each insertion making it is unnecessary for the user to count points.

The range of the window is defined by the numbers of the first and last data points in the window. The range may encompass the entire data set or only one point, whatever the user needs. Window definitions are checked during input and any window that exceeds the range of the data set is not allowed. Attempts to execute Options 2 through 5 without a window first being defined will not execute.

Empty data sets cannot be operated on by any of the window options. At least one data point must be in the data set upon entry to the window process. Should the entire data set be deleted during the window delete operation, further window processing will not be allowed, and control will pass back to the data display/correction menu.

A-4.3.9 EXTERNAL DATA FILE FORMAT

Whenever the user wants to read a data set from a file, he must ensure that the file follows the exact format that the CMDB software expects. The file must contain the data in sequential access, formatted form. This file format was chosen to allow the user to edit the data file when changes are needed, although image formatting would save storage space.

The first record of the file must specify the number of points in the data set. This number will be read from the file according to the format (20X,15). The first twenty characters are skipped to allow the caption "NUMBER OF POINTS =" to be in the file as in the case for files created by the CMDB software. It does not matter what is in this field as long as the point count is properly located in the 15 field.

The remainder of the file must contain the data points with one point per record, each record being written in format (1X,1PE14.7,1PE14.7) or one compatible with it. This format is the one used by the CMDB software to store its data point records. Each record will be read from the file with format (1X,E14.0,E14.0). The first field must contain the independent variable, and the second field the dependent variable.

A-4.0 DATA RETRIEVAL

Selection of the data retrieval option in the root menu prompts display of the following menu:

List of retrieve options:

1. materials in database,
2. materials in database by category,
3. references and sources,

4. manufacturer names and addresses,
5. units in database,
6. categories in database,
7. specific property, and
8. quit.

Select option by number:

Selection of Option 8 causes the program to terminate retrieval processing and to return to the root menu.

Selection of Options 1 through 7 prompts the display of the following menu to determine the output method of choice:

List of output options:

1. print retrieved reports to the terminal,
2. store retrieved reports into one file,
3. store individual reports into separate files, and
4. quit.

Select option by number:

Selection of output Option 4 causes the program to return to the retrieval options menu. Selection of Option 1 will route all retrieved reports to the terminal for display. A report is herein defined for the CMDB as being a packet of information for a single item retrieved from the database. For example, a list of all materials in the database would contain multiple reports with each report describing a separate material.

Option 2 will route all reports to both the terminal for display and to a single file for storage. Option 3 is similar to Option 2, except it breaks these reports apart and puts each one into its own file with the same name but with a different version number. Either option will allow the report to be stored with the corresponding headers in the file or with them deleted. This header option is selected by a query immediately following the output options menu selection and applies only to property data reports and not to descriptor reports.

After the retrieve and output options have been selected, the system performs the selected retrieval and display and returns to the retrieve options menu for further processing. These retrieve/display operations are described in the following sections.

A-4.1 DESCRIPTOR RETRIEVAL

Selection of one of the retrieve Options 1 through 6 causes the program to retrieve from the database the corresponding descriptor data and display and, if requested, store the reports. Retrieval occurs after the output option has been selected as described in Section 4.2. For all of these options except 2, reports for all descriptors in the database are retrieved without further input. Option 2, because it is a search by category, requires the user to go through the category number input sequence as described in Section 4.1.5. Only those descriptors with the corresponding category number are retrieved.

Each descriptor retrieved from the database is displayed or stored in an individual report containing the identification number and the descriptive information. The material descriptor includes multiple fields containing material name and number, category, batch number, and manufacturer. The other descriptors contain the identification number and a single field such as reference/source, manufacturer name and address, units name, and category name.

A-4.2 SPECIFIC PROPERTY RETRIEVAL

Selection of retrieve Option 7 causes the program to first query the user for the number of the material for which he wishes to retrieve data. This query procedure begins with the display of the following menu:

List of retrieval methods:

1. search via material number,
2. search via material name,
3. list material descriptors to determine material number, and
4. quit.

Selection option by number:

Selection of Option 4 returns the user to the data retrieve menu. Selection of Option 1 means that the user knows the material identification number and requires no inspection of the database to determine it. Selection of Option 2 means that the user wants to input a material name and have the program to list all material descriptors with that name so that he may extract the correct material identification number from this truncated list of materials. Selection of Option 3 automatically lists all material descriptors to allow the user to extract the material number by inspection of all materials in the database. Under Options 1 and 2, the user may still list all material descriptors in the database.

No matter the option selected here, the program will force the user to input the material number. The procedure asks questions of the user to determine whether or not he knows the number. The procedure will allow the user several outs by first listing the material descriptor and asking the user if it is the correct material. If it is, the user may move on to the next menu. If not, the user may continue inspection of the database until the required information is found. If it cannot be found, the procedure may be terminated with no retrieval operation being performed.

Once the material number has been determined and input to the program, the following menu is displayed to allow the user to select the property of interest:

List of properties for retrieval:

1. chemical genealogy,
2. density,
3. vapor pressure,
4. melting temperature,
5. gas chromatograph spectrum,
6. mass spectrum,
7. IR ATR plate spectrum,
8. real refractive index,
9. imaginary refractive index,
10. reflectivity,
11. transmissivity,
12. total mass loss,
13. CVCM,
14. outgassing species,
15. solar absorptance, and
16. quit.

Select option by number:

Selection of Option 16 returns the user to the retrieve menu. For Options 1 through 15, the data for the requested property type having the correct material number will be retrieved and displayed.

If requested, these reports will be stored to a file or collection of files depending upon the storage option selected as described in Section 4.2. Header information will be stored in the files unless headers are specifically cancelled by the user. When headers are cancelled, only the bare property data are stored and such data as material descriptor, reference, date of storage, and units are eliminated. Headers are always printed to the terminal with the data.

NOMENCLATURE

A	Geometric depolarization factor
a	Area, cm^2
C_c	Condensation coefficient
D^*	Normalized detectivity
d	Spacing of IDT electrodes, m
f	Frequency, Hz
h	Deposit thickness, cm
i_n, i_r, i_s	Detector output, amps
J_O	Laser intensity, photons/sec
K	Boltzmann's constant, ergs/Kelvin
k	Extinction coefficient
k_1, k_2	Constants related to SAW surface particle velocity, m^2-Sec/k_gH_2
L	Radiance, W/m^2-sr
M	Molecular weight, gm
m	Mass, gm
m_i	Incident mass flux, gm/cm^2-sec
m_g	Mass gain rate, gm/cm
m_o	Exiting mass flux, gm/sec
m_s	Mass loss rate, gm/sec

n	Refractive index
n_A	Avogadro's number, molecules, mole
n_s	Number density, molecules, cm^2
P_c	Chamber pressure, torr
P_i	Laser incident power
P_o	Source pressure, torr
p_m	Dipole moment, V-cm^2
Q	Legendre functions of second kind
R	Distance between SAW sensor and source, cm
r	Detector responsivity, amp/W
S_s	SERS signal level, photoelectrons/sec
T	Temperature, K
t_s	Thickness, cm
V_r	Rayleigh wave velocity, m/sec
ϵ	Dielectric function
η_t	Optical measurement efficiency
Θ_1, Θ_2	Angles defining SAW and source orientation, radius
λ	Wavelength, m
λ_1	Lame constant, n/m^2
μ'	Shear modulus, n/m^2

ϱ	Mass density, gm/cm^2
σ	Raman scattering cross section, cm^2/sr
Ω_c	Solid angle, sr
ω	Source orfice correction term
ω_o	Radiation frequency, Hz
ω_r	Raman frequency